University of Alberta

Local Oscillator and Focal Distance Measurement System for the Square Kilometre Array

by

Leonid Belostotski

A thesis submitted to the Faculty of Graduate Studies and Research in partial fulfillment of the requirements for the degree of Master of Science

Department of Electrical and Computer Engineering

Edmonton, Alberta

Spring 2000

National Library of Canada
Acquisitions and Bibliographic Services
395 Wellington Street
Ottawa ON K1A 0N4
Canada

Bibliothèque nationale du Canada
Acquisitions et services bibliographiques
395, rue Wellington
Ottawa ON K1A 0N4
Canada

Your file Votre référence

Our file Notre référence

The author has granted a non-exclusive licence allowing the National Library of Canada to reproduce, loan, distribute or sell copies of this thesis in microform, paper or electronic formats.

L'auteur a accordé une licence non exclusive permettant à la Bibliothèque nationale du Canada de reproduire, prêter, distribuer ou vendre des copies de cette thèse sous la forme de microfiche/film, de reproduction sur papier ou sur format électronique.

The author retains ownership of the copyright in this thesis. Neither the thesis nor substantial extracts from it may be printed or otherwise reproduced without the author's permission.

L'auteur conserve la propriété du droit d'auteur qui protège cette thèse. Ni la thèse ni des extraits substantiels de celle-ci ne doivent être imprimés ou autrement reproduits sans son autorisation.

0-612-60093-9

Canada

University of Alberta

Library Release Form

Name of Author: Leonid Belostotski

Title of Thesis: Local Oscillator and Focal Length Measurement System for the Square Kilometre Array

Degree: Master of Science

Year this Degree Granted: 2000

Permission is hereby granted to the University of Alberta Library to reproduce single copies of this thesis and to lend or sell such copies for private, scholarly, or scientific research purposes only.

The author reserves all other publication and other rights in association with the copyright in the thesis, and except as hereinbefore provided, neither the thesis nor any substantial portion thereof may be printed or otherwise reproduced in any material form whatever without the author's prior written permission.

Leonid Belostotski

18287-93 Avenue,
Edmonton, Alberta,
Canada, T5T 1V2

Jan. 19, 2000

University of Alberta

Faculty of Graduate Studies and Research

The undersigned certify that they have read, and recommend to the Faculty of Graduate Studies and Research for acceptance, a thesis entitled Local Oscillator and Focal Length Measurement System for the Square Kilometer Array submitted by Leonid Belostotski in partial fulfillment of the requirements for the degree of Master of Science.

T. Landecker

Dr. T. L. Landecker (co-supervisor)

D. Routledge

Dr. D. Routledge (co-supervisor)

Dr. C.J. Backhouse

A.E. Peterson

Prof. ~~Dr.~~ A.E. Peterson

J.F. Vaneldik

Dr. J.F. Vaneldik

Jan. 11, 2000

ABSTRACT

A system which simultaneously provides coherent local oscillator signal and measures focal length for the Large Adaptive Reflector is discussed. The Local Oscillator subsystem provides a phase-stable signal to an airborne platform over a radio link. A phase stability of 5°rms at 22 GHz is the goal for the system. Feedback is employed to readjust the phase of the delivered signal, to compensate for changes in the transmission medium. The dynamic properties of the Local Oscillator system are controlled primarily by a phase-locked loop. A Focal Length Measurement subsystem employing the Chinese remainder theorem for ambiguity resolution is proposed. The subsystem will measure the focal distance of 500 m with an accuracy of 70 μm. Both systems are based on interferometric techniques and are combined into one. A prototype of the Local Oscillator subsystem has been built and tested to demonstrate feasibility of the concept.

ACKNOWLEDGMENTS

I would like to thank all people who helped me with this thesis in any way. I thank the staff of the Dominion Radio Astrophysical Observatory for being very helpful and friendly. I would like to thank my supervisors Dr. Tom Landecker, Dr. Dave Routledge, and Dr. Fred Vaneldik for helping me through different stumbling blocks I ran into while working on the thesis. I would like to thank Dr. Peter Dewdney and Dr. Bruce Veidt for lots of advice and for making the work on the Square Kilometre Array and the Large Adaptive Reflector continue. I thank Rod Stuart, Ron Casorso, Jean Bastien, and Ron McDougall for helping me build my system. I thank Brian Force for mentioning the "Chinese numbers" which eventually led to employment of the Chinese remainder theorem in my system. I would like to thank Anne Guerra for helping with editing the thesis and with different problems encountered along the way. I would like to thank programmers who created LyX the document processor that made writing this thesis easier.

Contents

Abstract

Acknowledgment

List of Figures

List of Tables

Glossary

Table of Symbols

1 Background **1**

1.1 Introduction 1

1.2 The Square Kilometre Array 2

1.3 The Large Adaptive Reflector telescope 4

1.3.1 A Local Oscillator system and a Focal Length measurement system 6

1.3.2 Location of the FLLOSS within the LAR telescope 7

1.4 FLLOSS specifications 7

1.5 Thesis layout 8

2 Distance measurement systems **9**

2.1 Introduction 9

2.2 Background 9
2.2.1 Distance measurement 9
2.2.2 Pseudo-random noise 10
2.2.2.1 PRN selection 10
2.2.2.2 PRN generation 11
2.2.2.3 Delay measurement using PRN 12
2.2.3 Atmospheric effects 13
2.2.4 Cycle slips, Multipath and Doppler shift 14
2.2.5 System noise 15
2.2.6 Linear combination of signal phases 15
2.3 Summary of different ranging systems 15
2.3.1 Laser-based ranging systems 15
2.3.2 RF pulse technique 16
2.3.3 Correlator techniques 16
2.3.3.1 Wideband noise modulation 16
2.3.3.2 Sinusoidal sweep frequency modulation 18
2.3.3.3 Bandwidth synthesis 18
2.3.4 Tellurometer distance measurement scheme 19
2.3.4.1 System structure 19
2.3.4.2 System operation 19
2.3.5 Global Positioning System 22
2.3.5.1 GPS signal structure 22

2.3.5.2 Code Pseudorange 23
2.3.5.3 Phase Pseudorange 23
2.3.5.4 Distance Measurement 24
2.4 Measurement accuracy 26
2.4.1 Laser-based devices 26
2.4.2 Wideband noise modulation 27
2.4.3 Sinusoidal sweep frequency modulation 27
2.4.4 Bandwidth synthesis 27
2.4.5 Tellurometer 28
2.5 Sensitivity to errors 28
2.5.1 Laser-based systems 28
2.5.2 Correlator-based systems 28
2.5.3 Phase measuring systems 28
2.6 Conclusion 29
3 Local Oscillator System **31**
3.1 Introduction 31
3.2 Background: Control systems 31
3.2.1 Control system theory 32
3.2.1.1 S-plane domain 33
3.2.1.2 Frequency response domain 34
3.2.1.3 Time domain specifications 37
3.2.1.4 Phase Locked Loop 37

3.3 Summary of existing LO systems 38
3.3.1 Swarup and Yang LO system 38
3.3.2 Cascaded PLL system 38
3.3.3 Automatically Correcting system 39
3.3.4 Spatially Distributed PLL system 40
3.3.5 Discussion 41
3.4 Comparison of the Cascaded PLL and Spatially Distributed systems . 41
3.4.1 Comparison of steady-state errors due to distance changes . . 41
3.4.1.1 Spatially Distributed PLL system 41
3.4.1.2 Cascaded PLL system 44
3.4.2 Stability in the presence of time delay 47
3.4.3 Distance Measurement 48
3.5 Conclusions 48
4 The Focal Length/LO system **50**
4.1 Introduction 50
4.2 Background: Chinese remainder theorem 50
4.3 Combining the LO and FLM systems 51
4.4 Selection of the frequencies of operation 60
4.5 Procedure for distance measurement 62
4.6 Other design issues 65
4.6.1 Calibration 65
4.6.2 Frequency of distance measurements 66

4.6.3 Phase measurement accuracy 66
4.6.4 Minimum signal to noise ratio 67
4.6.5 Antennas 69
4.7 Conclusion 70
5 LO system prototype design **71**
5.1 Introduction 71
5.2 Background 71
5.2.1 Link budget and signal to noise ratio 71
5.2.2 Effect of impedance mismatches on signal phases 72
5.3 LO prototype design 73
5.3.1 Selection of frequencies for use in LO prototype 73
5.3.2 Preliminary prototype configuration discussion 74
5.3.3 Noise Considerations for the LO system 75
5.3.3.1 Noise introduced in phase-halving PLL 75
5.3.3.2 Noise acquired in the uplink 76
5.3.3.3 Noise acquired in the downlink 77
5.3.3.4 Noise due to the motion of airborne platform 78
5.3.4 LO prototype simulations 79
5.3.5 Phase-halving PLL design 85
5.3.5.1 Component selection 85
5.3.5.2 PLL loop filter design 87
5.4 LO prototype implementation 87

5.4.1 PLL implementation 87
5.4.1.1 Phase-halving PLL phase stability measurement . . . 87
5.4.2 Antenna design and implementation 88
5.4.2.1 Feed design 88
5.4.2.2 Paraboloidal antenna performance measurement . . . 95
5.4.3 LO prototype testing 99
5.4.3.1 Link budget for 800 metre test 101
5.4.3.2 Link budget for 350 metre test 106
5.5 LO system performance 110
5.5.1 LO prototype test without time delay 110
5.5.1.1 Improvement of the LO performance 111
5.5.2 100 metre test 112
5.5.3 350 metre test 117
5.5.4 800 metre test 121
5.6 Discussion 125
6 Conclusion **127**
Bibliography **129**
A Remote unit and ground unit circuit diagrams **134**
B Phase-halving PLL: circuit diagram **137**
C Mixer assembly **141**

List of Figures

1.1 Sensitivity of radio telescopes (adapted from [6]). 2

1.2 Large Adaptive Reflector telescope. 3

1.3 Basic interferometer. 4

1.4 Large Adaptive Reflector. 5

2.1 Simple PRN shift register. 11

2.2 Power spectrum of band-limited white noise. 17

2.3 Auto-correlation function of band-limited white noise. 18

2.4 Tellurometer block diagram (adapted from [47]). 20

2.5 C/A code correlation (adapted from Leick (1995) [36]). 24

3.1 Block diagram of a feedback control system. 32

3.2 Typical Bode plot, showing gain margin of 41.8 dB and phase margin of 98.9°. 36

3.3 Phase Locked Loop block diagram. 37

3.4 Active loop filter for a second order PLL. 38

3.5 Cascaded PLL system (adapted from Landecker and Vaneldik (1982) [32]). 39

3.6 Automatically Correcting system (adapted from Thompson et al. (1986) [54]). 40

3.7 Spatially distributed PLL system (adapted from Veidt et al. (1985) [55]). The three transmission lines shown represent a single physical cable. 40

3.8 Phase-domain block diagram of the Spatially Distributed system. $R(s)$ is the input to the LO sytem, $L(s)$ represents a change in the path length, and $C(s)$ is the output of the LO system. 42

3.9 Phase-domain block diagram of the phase control Cascaded PLL system. $R(s)$ is the input to the LO sytem, $L(s)$ represents a change in the path length, and $C(s)$ is the output of the LO system. 45

3.10 Phase-domain block diagram of a PLL based phase-halving system. . 45

4.1 Block diagram of the LO system. 53

4.2 LO system upconverted to higher frequencies. 54

4.3 LO system with the PRN signal. 55

4.4 Complete FLLOSS: ground unit. 56

4.5 Complete FLLOSS: remote unit. 57

4.6 Uplink and Downlink Spectra. 58

5.1 Generation of phase errors due to impedance mismatches. 73

5.2 Cascaded PLL LO prototype diagram. Initially the LO prototype has been designed for 2 km focal distance. The specification, however, was later reduced to 500 m. 75

5.3 Noise introduced in phase-halving PLL. $H(s)$ denotes the transfer function of the phase-halving PLL. 76

5.4 Noise acquired in the uplink transmission medium. 76

5.5 Noise acquired in the downlink transmission medium. 77

5.6 Disturbance due to the distance change. 78

5.7 Behaviour of error signal $R(j\omega) - C(j\omega)$ of the LO system as it acquires lock. The initial state of $C(j\omega)$ differed by 0.2 rad from the phase $R(j\omega)$. Transfer functions of the USG and the LSG were assumed to be 1. $R(j\omega)$ and $C(j\omega)$ are shown in Figure 5.3. F_n is the natural frequency expressed in hertz. 80

5.8 Frequency response from noise input $D_1(j\omega)$ to phase output $C(j\omega)$ of the closed loop LO system shown in Figure 5.4. Transfer functions of the USG and the LSG were assumed to be 1. F_n is the natural frequency expressed in hertz. 81

5.9 Frequency response from noise input $D_2(j\omega)$ to phase output $C(j\omega)$ of the closed loop LO system shown in Figure 5.5. Transfer functions of the USG and the LSG were assumed to be 1. F_n is the natural frequency expressed in hertz. 82

5.10 Frequency response from input $L(j\omega)$ to phase output $C(j\omega)$ of the closed loop LO system shown in Figure 5.6. Transfer functions of the USG and the LSG were assumed to be 1. F_n is the natural frequency expressed in hertz. The time delay in this simulation was 7.5 μs. . . . 83

5.11 Behaviour of error signal $R(j\omega) - C(j\omega)$ of the LO system as it acquires the lock for three different values of the time delay. The initial state of $C(j\omega)$ differed by 0.2 rad from the phase of the $R(j\omega)$ which was kept constant. Transfer functions of the USG and the LSG were assumed to be 1. $R(j\omega)$ and $C(j\omega)$ are shown in Figure 5.3. 84

5.12 Phase-domain diagram of the phase-halving PLL system diagram. . . 85

5.13 Photograph of the VCO used in the LO prototype. 86

5.14 Assembled phase-halving PLL. 88

5.15 Phase stability measurement. This figure records the difference between the VCO phase and the phase of the input reference signal. . . 89

5.16 Coaxially-mounted dual helical feed. 90

5.17 Reflector dimensions. 91

5.18 Beam pattern of the dual helix feed at 1.8 GHz when both helices are made of 10 AWG wire. 93

5.19 Feed antenna patterns at 1.35 GHz normalized by $E(0°)$. 94

5.20 Feed antenna patterns at 1.8 GHz normalized by $E(0°)$. 94

5.21 Feed antenna patterns at 3.15 GHz normalized by $E(0°)$. 95

5.22 Measured feed SWR. 96

5.23 Paraboloidal antenna and its feed. 97

5.24 Paraboloidal antenna beam patterns recorded by solar drift scans. . . 98

5.25 Solar flux density values (sfu), September 28, 1998 [41]. 99

5.26 Assembled ground unit. 101

5.27 Assembled remote unit. 102

5.28 LO prototype (800 m test). 103

5.29 LO prototype (350 m test). 104

5.30 Assembled LO system. (Two racks right of centre.) 110

5.31 Photograph of the "mixer assembly" 111

5.32 Improvement of the LO performance. Horizontal scale from beginning of each curve to the end in each figure represents a change of 0.47 m in the path length between the ground and the remote units. The vertical scale of 3.6 deg/div represents the phase variations in the LO output. 113

5.33 Phase of the LO output signal as the path length changes (100 m test). The figure represents phase variations in the output of the LO system as the path length between the ground and the remote units changes by 0.47 m. 114

5.34 Block diagram of the lock acquisition test (100 m test). 115

5.35 "Locking response" of the phase-halving PLL loop filter output to a square wave frequency-modulation of the 675 MHz reference signal (100 m test). 116

5.36 LO system phase stability test (350 m test). The phase of the LO output signal was compared with the phase of the 3.15 GHz reference signal. 117

5.37 Phase stability of the LO system as the distance changed (350 m test). The ground antenna was moved periodically back and forth by 0.4 m with an average speed of 0.14 m/s. The phase of the LO output signal was compared with the phase of the 3.15 GHz reference signal. 118

5.38 Open loop performance of the LO system (350 m test). The ground antenna was moved back and forth a few times. 118

5.39 Lock-in time measurements. An electrically controlled switch, driven by a square wave signal and introduced at the output of the VCO, broke and restored the phase-halving PLL loop so that the lock-in time could be measured at the output of the phase-halving PLL loop filter. (350 m test) 119

5.40 Phase variations at the LO output as a function of the antenna pointing. The angles were obtained from the power level measurements. The theoretical value for the HPBW was used. The phase is normalized. 120

5.41 "Locking response" of the phase-halving PLL loop filter output to a square wave modulation of the 675 MHz reference signal (350 m test). 121

5.42 LO output signal spectrum (350 m test). The resolution bandwidth equals 10 kHz and the spectrum analyzer's internal oscillator is used. 122

5.43 LO reference signal spectrum (350 m test). The resolution bandwidth equals 10 kHz and an external frequency reference is used. 123

5.44 "Locking response" of the phase-halving PLL loop filter output to a square wave modulation of the 675 MHz reference signal as the gain of "Amplifier A" increased by 100 (350 m test). 124

A.1 Remote unit circuit diagram. 135

A.2 Ground unit circuit diagram. 136

B.1 Phase-halving system. 138

B.2 Phase-halving PLL: phase detector and loop filter. 139

B.3 Lock indicator. 140

C.1 Mixer assembly. 141

List of Tables

2.1 MU and RU pattern frequencies (adapted from [47]). 19

2.2 Components of the GPS satellite signal [25], [50]. 22

4.1 Frequency bands considered for the FLLOSS. 60

4.2 Radio frequency bands [28]. 62

4.3 Calibrators available for FLM calibration. 67

5.1 Frequencies selected for the LO prototype. 74

5.2 Coupling between two helices. Helices were made of 10 AWG wire. . . 92

5.3 Coupling between the two helices made from the thin wire. 93

5.4 HPBWs of the paraboloidal antenna at the three frequencies. 98

5.5 Paraboloidal antenna efficiencies and effective areas. 100

5.6 The system noise figure of the remote unit (800 m test). 105

5.7 SNR of the input to the remote unit (800 m test). 105

5.8 Noise figure of the signal emerging from buried cable (800 m test). . . 106

5.9 The system noise figure of the ground unit (800 m test). 107

5.10 SNR at the input to the ground unit (800 m test). 107

5.11 The system noise figure of the remote unit (350 m test). 108

5.12 SNR of the input to the remote unit (350 m test). 108

5.13 Noise figure of the signal arriving at the remote antenna cable (350 m test). 109

5.14 The system noise figure of the ground unit (350 m test). 109

5.15 SNR at the input to the ground unit (350 m test). 110

GLOSSARY

CE	Characteristic Equation
CW signal	Continuous Wave Signal
CRT	Chinese Remainder Theorem
DRAO	Dominion Radio Astrophysical Observatory
FLLOSS	Focal Length/Local OScillator System
FLM	Focal Length Measurement
FM	Frequency Modulation
GM	Gain Margin
GPS	Global Positioning System
HPBW	Half-Power Beamwidth
LAR	Large Adaptive Reflector
LHCP	Left Hand Circular Polarization
LO	Local Oscillator
LSG	Lower Sideband Generator
MSR	Main lobe to Side lobe Ratio
MU	Master Unit
NF	Noise Figure
NM	Navigation Message
PFD	Phase/Frequency Discriminator (Detector)
PLL	Phase Locked Loop
PM	Phase Margin
PRN	Pseudo-Random Noise
PSD	Power Spectral Density
PSK	Phase Shift Keying
RF	Radio Frequency
RHCP	Right Hand Circular Polarization
RU	Remote Unit
SKA	Square Kilometre Array
SNR	Signal to Noise Ratio
TLM	Telemetry word in GPS
USG	Upper Sideband Generator
VCO	Voltage Controlled Oscillator
VLA	Very Large Array
VLBI	Very Long Baseline Interferometry

TABLE OF SYMBOLS

Chapter 1		
Symbol	**Units**	**Symbol definition**
D	m	interferometer baseline
N		number of LAR telescopes in the SKA

Chapter 2		
Symbol	**Units**	**Symbol definition**
n		number of bits in a PRN sequence
N		number of stages in a PRN register
$\phi(k)$		Euler's function producing the number of integers having no common factor with k
k		an integer
$H_{lim}(f)$, $H_{lim}(\omega)$		transfer function of a PRN bandwidth limiting filter
f	Hz	frequency
ω	rad/s	angular frequency
B_w	Hz	bandwidth of a band limited PRN signal
$u(.)$		unit step
$S(\omega)$	V^2/Hz	band limited power spectral density of PRN
$S_0(\omega)$	V^2/Hz	power spectral density of PRN (full bandwidth)
$R(t)$		auto-correlation function of PRN (band limited)
$R_0(t)$		auto-correlation function of PRN
$h_{lim}(t)$		impulse response of $H_{lim}(f)$
t	s	time

continues...

Symbol	Units	Symbol definition
Sa		sinc function
v_{gr}	m/s	group velocity
λ	m	wavelength
v_{ph}	m/s	phase velocity
n_{ph}		index of refraction for v_{ph}
n_{gr}		index of refraction for v_{gr}
A_i		a constant proportional to the number of particles capable of vibrating at frequency corresponding to λ_i
λ_i	m	wavelength of natural frequency of particles in the air
φ_a, φ_b	rad	arbitrary phase
n_a, n_b		integer number
φ	rad	phase of linear combination $n_a\varphi_a + n_b\varphi_b$
f_a, f_b change	Hz	frequencies
τ	s	time shift
$S_{wn}(f)$	V^2/Hz	band limited power spectrum density of white noise
$A(t)$		auto-correlation function of white noise
F_0	Hz	white noise bandwidth
$y(t)$		periodic PRN binary sequence
C_{ij}		cross-correlation function of $y(t)$
Δt	s	time delay
t_0	s	period of F_0
f_M	Hz	MU pattern frequency

continues...

Symbol	Units	Symbol definition
λ_M	m	wavelength of f_M
f_R	Hz	MU pattern frequency
λ_R	m	wavelength of f_R
φ_M	rad	phase of f_M
x		fraction of λ_M
N_M		number of whole λ_M
φ_R	rad	phase of f_R
y		fraction of λ_R
N_R		number of whole λ_R
N_{M-R}		number of whole wavelength of $f_M - f_R$
z		fraction of $f_M - f_R$ wavelength
f_0	Hz	fundamental frequency of GPS signals
L_1, L_2		GPS signals
f_1, f_2	Hz	carrier frequencies of L_1 and L_2
$C_p(t)$, $C_{c/a}(t)$		GPS PRN codes
$M_N(t)$		GPS navigation message
$\Delta\tau$	s	time difference between satellite clock and GPS receiver
t_r	s	time shown by GPS receiver
t_s	s	satellite time
$\Delta\delta$	s	biases affecting code pseudorange
R	m	distance from the ground to satellite
ρ	m	true distance between GPS receiver and the satellite

continues...

Symbol	Units	Symbol definition
$\varphi_r^s(t)$	rad	phase difference between satellite carrier and the GPS receiver carrier
$\varphi_r(t)$	rad	receiver signal phase at time t
$\varphi^s(t)$	rad	received satellite signal phase at time t
$N_r^s(1)$	rad	initial integer ambiguity
$I_{r,\varphi}^s(t)$	rad	ionospheric effects
$T_r^s(t)$	s^2rad/m	tropospheric effects
$d_{r,\varphi}(t)$, $d_\varphi^s(t)$	rad	hardware delays
$d_{r,\varphi}^s(t)$	rad	multipath phase contribution
ϵ_φ	rad	random phase noise
N_a	rad	phase ambiguity ($N_a = N_r^s(1)$)
f_w	Hz	$f_1 - f_2$
λ_w, λ_{L_1}, λ_{L_2}	m	wavelengths of f_w, f_1, f_2
Φ	rad	$\varphi_r^s(t)$
Φ_w ($\Phi_{L_1-L_2}$)	rad	phase difference between satellite carrier and the GPS receiver carrier of f_w
N_{L_1}, N_{L_2}	rad	phase ambiguity in f_1 and f_2
$\varphi_{L_1+L_2}$	rad	sum of the f_1 phase and the f_2 phase
φ_{L_3}	rad	linear combination $\varphi_{L_1} - \frac{f_2}{f_1}\varphi_{L_2}$
Φ_{L_1}, Φ_{L_2}	rad	phase difference between satellite carrier and the GPS receiver carriers of f_1 and f_2
R_{L_1}, R_{L_2}	m	distance from the ground to the satellite measured with f_1 and f_2
N_w	rad	phase ambiguity in f_w
f_{PRN}	Hz	frequency of PRN

Chapter 3		
Symbol	**Units**	**Symbol definition**
$R(s)$		reference input
$C(s)$		controlled variable
s	rad/s	complex frequency
ω	rad/s	angular frequency
σ	rad/s	real part of complex frequency
$G(s)$		transfer function of a process or a plant
$D(s)$		disturbance
$E(s)$		actuating signal
$H_{fb}(s)$		feedback transfer function
$G_{CL}(s)$		transfer function $\frac{C(s)}{R(s)}$
$g_{CL}(t)$		impulse response of $G_{CL}(s)$
K		static loop sensitivity
z_i, p_j	rad/s	zeros and poles in a transfer function
m, n		number of poles and zeros in a transfer function
i, j		indices
$f(t)$		a stable time function
$F(t)$		Laplace transform of $f(t)$
t	s	time
P		step amplitude
e_{ss}	rad	steady-state error
Z		amplitude
$c(t)$	rad	system output
$M(\omega)$		magnitude of $G(\omega)$

continues...

Symbol	Units	Symbol definition
$\phi(\omega)$	rad	phase of $c(t)$
ζ		damping ratio
M_P	deg	phase margin
M_G		gain margin
T_r	s	rise time
B_{cl}	rad/s	close loop bandwidth
T_d	s	time delay
G_{VCO}		transfer function of a VCO
K_0	rad/sV	gain of a VCO
K_d	rad/V	phase detector gain
$F(s)$		transfer function of a loop filter
$G_{PLL}(s)$		transfer function of a PLL
A		gain of loop filter amplifier
R_1, R_2	Ω	resistors used in a loop filter
C	F	capacitor used in a loop filter
τ_1, τ_2	s	loop filter time constants
ω_n	rad/s	natural frequency
φ	rad	phase
F_1, F_2	Hz	reference frequencies in Cascaded PLL LO system
a	rad	phase shift
Q	rad	phase of F_2 at the input to the LSG
ν_1, ν_2	Hz	reference frequencies in Automatically Correcting System
L	m	distance

continues...

Symbol	Units	Symbol definition
$T_{cl}(s)$		close loop transfer function
b	1/s	$\frac{1}{\tau_2}$
$G_1(s)$		transfer function of LSG
$G_2(s)$		transfer function of USG
$H(s)$		transfer function of phase-halving PLL

Chapter 4		
Symbol	**Units**	**Symbol definition**
$m_1, \ldots, m_s$		s relatively prime positive integers
$\beta_1, \ldots, \beta_s$		s integers
x		congruence of m_i and β_i
L	m	distance
b_i		constants required by CRT
F_{pc}	Hz	frequency carrier modulated by PRN
F_p	Hz	frequency carrier upconverting F_{pc}
F_c	Hz	high frequency carrier for LO system
F_0	Hz	reference signal delivered by LO system
F_{PRN}	Hz	frequency of PRN code
F_{ref}	Hz	reference signal required by LO system
$F_{ref/2}$	Hz	half of F_{ref}
F'	Hz	$F_p - F_{pc}$
F_a	Hz	$F_0 - F_{ref}$
F_1	Hz	$F_c + F_a$

continues...

Symbol	Units	Symbol definition
F_2	Hz	$F_c + F_{ref}$
F_3	Hz	$F_c - F_0$
F_4	Hz	$F_3 - F_0$
F_5	Hz	$F_p + F_0$
F''	Hz	$F' + F_0$
f	Hz	$F \angle \varphi$
φ	rad	phase
A	rad	negative of the LO output phase
ϕ_{LO}	rad	phase error in LO output
$\Delta\phi_3$, $\Delta\phi_4$, $\Delta\phi_5$	rad	uncalibrated phase errors in f_3, f_4, and f_5
L_3, L_4, L_5	rad	phases experienced by f_3, f_4, and f_5 travelling distance L
f_6	Hz	$f_3 + f_5$
f_7	Hz	$f_4 + 2f_5$
f_8	Hz	$2f_3 - f_5$
f_9	Hz	$f_3 - f_4 - f_a$
f_{10}	Hz	$f_4 - f_5 + f_a$
L_6, L_7, L_8	rad	phases experienced by f_6, f_7, and f_8 travelling distance L
$\Delta\phi_6$, $\Delta\phi_7$, $\Delta\phi_8$	rad	uncalibrated phase errors in f_6, f_7, and f_8
L_9, L_{10}	rad	phases experienced by f_9 and f_{10} travelling distance L
$\Delta\phi_9$, $\Delta\phi_{10}$	rad	uncalibrated phase errors in f_9 and f_{10}
λ_7, λ_8, λ_0	m	wavelength of F_7, F_8, and F_0
r_7, r_8, r_0	m	accuracy of λ_7, λ_8, λ_0 measurement

continues...

Symbol	Units	Symbol definition
m_7, m_8, m_0		inputs to CRT
β_7, β_8, β_0		distance measured with f_7, f_8, and f_0 in units of r_7, r_8, and r_0
β_7^0, β_8^0, β_0^0		true distance measured with f_7, f_8, and f_0 in units of r_7, r_8, and r_0
$\Delta\beta_7$, $\Delta\beta_8$, $\Delta\beta_0$		error in distance measured with f_7, f_8, and f_0 in units of r_7, r_8, and r_0
L_0, L_1, L_2, L_3		distances produced by the CRT
E_0, E_1, E_2, E_3		errors in distances produced by the CRT
C_j^i, b_j^i		constants required by the CRT
B	Hz	bandwidth of the SKA correlator
SNR		signal to noise ratio
T_σ	K	1σ noise temperature
T_{LAR}	K	LAR system noise temperature
T_{ref}	K	reference antenna system noise temperature
T_a	K	antenna noise temperature
S_{cal}	Jy	flux density of the calibration source
A	m^2	effective area
A_{LAR}	m^2	LAR effective area
A_{ref}	m^2	reference antenna effective area
$y(t)$		LO output signal
P		amplitude of $y(t)$
ϕ	rad	phase of $y(t)$
$n_i(t)$		noise signal in the LO output
$n_c(t)$, $n_s(t)$		noise signal orthogonal components

continues...

Symbol	Units	Symbol definition
E_n		noise envelope
Θ_n		noise phase
$R(t)$		envelope of $y(t)$
$\Delta\phi$	rad	phase error due to noise
f_m	Hz	antenna centre frequency
λ_m	m	wavelength of f_m

Chapter 5		
Symbol	**Units**	**Symbol definition**
L_{FS}		free space attenuation
λ	m	wavelength
d	m	distance between antennas
B	Hz	bandwidth
N	W	noise power
T	K	noise temperature
T_e	K	system noise temperature
NF		noise figure
T_0	K	standard reference temperature
NF_1, NF_2, NF_3		noise figures of cascaded stages
$Gain_1$, $Gain_2$		power gains of cascaded stages
SNR		signal to noise ratio
G_{AT}, G_{AR}		gains of transmitting and receiving antennas
P_{TX}	W	transmitted power

continues...

Symbol	Units	Symbol definition
Γ		reflection coefficient
SWR		standing wave ratio
F_0	Hz	frequency delivered by LO system
F_{ref}	Hz	reference frequency required by LO system
F_a	Hz	$F_0 - F_{ref}$
T_d	s	time delay
$G_1(s)$, $G_2(s)$		transfer functions of LSG and USG
$H(s)$		transfer function of phase-halving PLL
$R(s)$		reference input
$C(s)$		controlled variable (output)
$D(s)$		noise introduced in phase-halving PLL
$D_1(s)$		uplink disturbance
$D_2(s)$		downlink disturbance
$L(s)$		disturbance due to distance change
B_L	Hz	PLL noise bandwidth
ω_n	rad/s	PLL natural frequency
ζ		damping ratio
$B_{L_{min}}$	Hz	minimum noise bandwidth
ω_{3dB}	rad/s	PLL bandwidth
K		loop sensitivity
A		loop filter amplifier gain
K_d	rad/V	phase detector gain
K_0	rad/sV	VCO gain
Q		quality factor

continues...

Symbol	Units	Symbol definition
τ_1, τ_2	s	loop filter time constants
R_1, R_2	Ω	loop filter resistors
C	F	loop filter capacitor
C_λ		helix circumference normalized by wavelength
α	deg	helix pitch angle
S_λ		spacing between turns in a helix normalized by wavelength
n		number of turns in a helix
D		helix gain
ϕ	deg	feed opening angle
AR		axial ratio
R	Ω	helix terminal resistance
T_s	K	antenna temperature due to the Sun
P_s	W	power due to T_s
T_n	K	calibration noise temperature
P_n	W	power due to T_n
A_{eff}	m^2	effective area
S	sfu	solar flux density
NF_{ru}		noise figure of the remote unit
T_{ru}	K	noise temperature of the remote unit
NF_{ra}		noise figure of the signal transmitted by remote antenna
SNR_{ru}		signal to noise ratio at the input to the remote unit
T_{ga}	K	noise temperature received by ground antenna

continues...

Symbol	Units	Symbol definition
NF_{gu}		noise figure of the ground unit
T_{gu}	K	noise temperature of the ground unit
SNR_{gu}		signal to noise ratio at the input to the ground unit
K_m	Hz	gain of frequency modulator
t_{lock}	s	lock-in time

Chapter 1

Background

1.1 Introduction

The field of radio astronomy at centimetre wavelengths is continuously evolving. Improved sensitivity and very fine resolution achievable with interferometric techniques are making centimetre wavelength astronomy well established. Very Long Base Line Interferometry (VLBI) techniques and Space VLBI techniques enable researchers to explore the Universe with microarcsecond resolution. Recent advances in telescope receiver sensitivity, digital bandwidth, and imaging techniques improve overall sensitivity of the telescopes. However, it appears that radio astronomers are reaching the limit of sensitivity achievable with the current telescopes. The only avenue to improving sensitivity is increasing the collecting area [14]. Figure 1.1 shows the increase in sensitivity of radio telescopes over the history of radio astronomy.

Even though radio astronomy is making substantial progress upgrading existing telescopes, some critical astrophysical problems cannot be solved without increasing the sensitivity. It seems that current technologies are reaching saturation, and to keep up with the general trend shown in Figure 1.1 a breakthrough technology is required to provide a large increase in collecting area without large cost increases.

There are several alternative telescopes being designed in different countries. The Square Kilometre Array (SKA[1]) telescope based on the Large Adaptive Reflector (LAR) telescope[2] is favored by the Canadian group and is discussed in this thesis.

[1] also known as 1kT or SKAI.

[2] in this thesis "LAR" refers to the reflector itself while "LAR telescope" refers to the complete telescope including the reflector and the airborne platform.

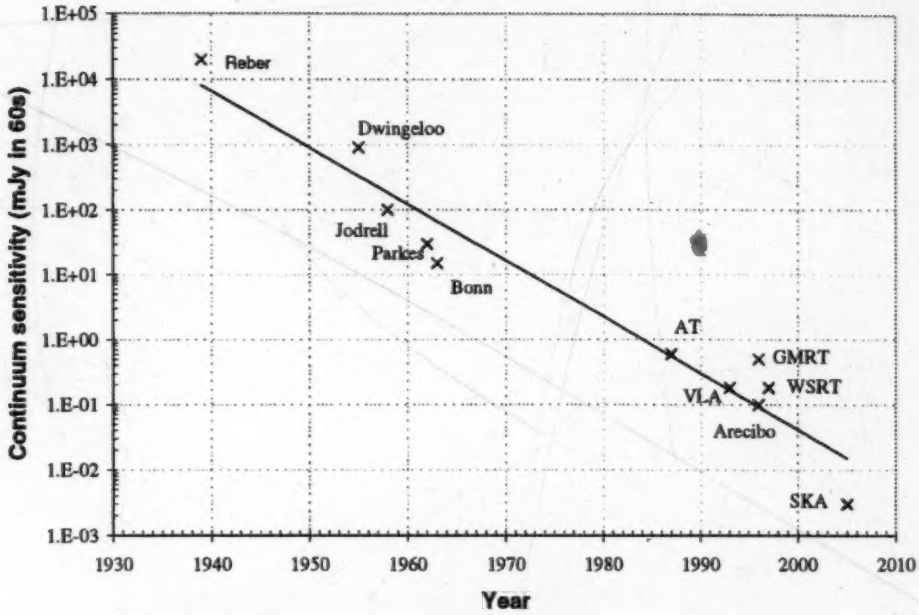

Figure 1.1: Sensitivity of radio telescopes (adapted from [6]).

1.2 The Square Kilometre Array

The SKA will have a square kilometre of collecting area and will operate at wavelengths ranging from 1 m (300 MHz) to possibly 1 cm (30 GHz) [14]. It will be an aperture synthesis telescope and will consist of up to thirty-five LAR telescopes and airborne vehicles supporting the receiving elements (feeds) of each LAR telescope as shown in Figure 1.2. The concept for the LAR was proposed by T.H. Legg (1997) [35]. Note that during The International Square Kilometre Array Meeting in Sydney, Australia, held on December 15-17, 1997, the initial highest frequency requirement of 30 GHz was lowered. Thus, researchers designing the LAR have adopted an upper frequency of 22 GHz.

The SKA telescope will employ traditional aperture synthesis techniques for obtaining images of the observed parts of the sky. Aperture synthesis is a convenient technique of simulating a telescope having large collecting area with a number of smaller telescopes separated by some distances. By using small antennas as an aperture synthesis telescope, the great sensitivity and great resolution of the large telescope is achieved. Aperture synthesis is the technology of choice at the present time. There have been many telescopes built using this technique such as the Very Large Array (VLA) and the Synthesis Telescope at the Dominion Radio Astrophys-

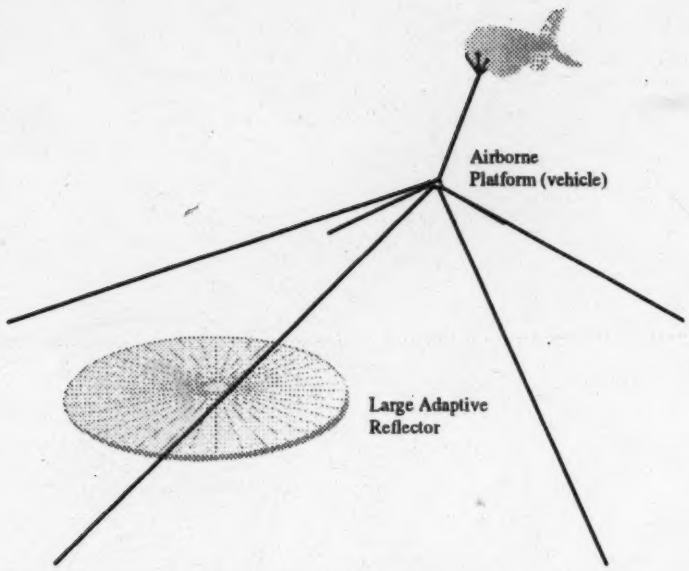

Figure 1.2: Large Adaptive Reflector telescope.

ical Observatory (DRAO) and many others.

In the limiting case an aperture synthesis telescope can consist of only two antennas linked together and separated by a baseline, D. This case is also known as a "two-element interferometer". The basic interferometer is the backbone of any aperture synthesis telescope. The antennas are connected to cables carrying received signals to the centre point where the signals are cross-correlated. A correlator consists of a multiplier and an integrator. Figure 1.3 shows a diagram of a basic interferometer.

The response of the correlator to a source moving across the sky is called the visibility. With enough visibility measurements the distribution of the brightness in the sky can be determined and maps of observed regions are created by calculating two-dimensional Fourier transforms of the visibility function.

In the SKA, each two LAR telescopes will constitute one of $\frac{N^2-N}{2}$ interferometric pairs, where N is the number of LAR telescopes in the SKA. The visibilities from all such pairs will be combined and analyzed to create the maps of the sky. All LAR telescopes will be controlled from one central point. The data received by the LAR telescopes will be correlated by the SKA correlator.

The SKA will be by far the largest telescope ever built. With a collecting area thirty times greater than that of the present largest telescope, the SKA will have sensitivity one hundred times that of the VLA. It will have a field of view larger

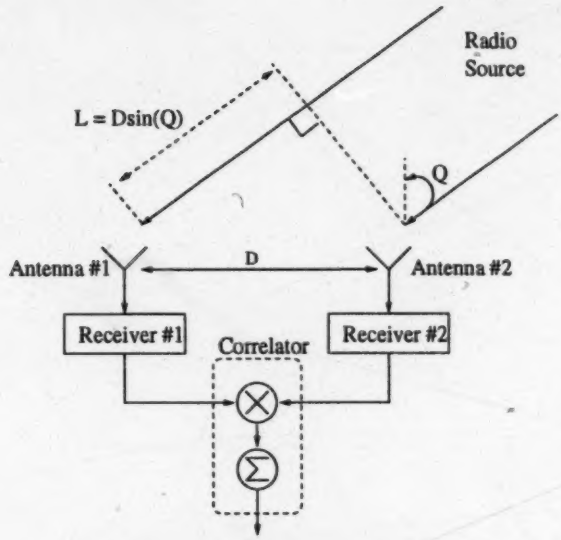

Figure 1.3: Basic interferometer.

than the Moon and the spatial resolution of the SKA will exceed the resolution of the Hubble Telescope. A. R. Taylor and R. Braun (1999) produced an extensive document summarizing some of the most important goals for the SKA as they are seen at the present time [52].

1.3 The Large Adaptive Reflector telescope

The LAR telescope represents a novel concept for designing antennas with very large collecting areas. Up until now, the largest fully steerable antenna with the diameter of 100 m is located in Effelsberg, Germany. It seems impossible to build traditional antennas having diameter much larger than 100 m because of structural limitations. A structure of that size becomes too heavy and keeping it in the perfectly parabolic shape becomes an impossible task.

In the LAR telescope, the 200 m reflecting surface is supported by the ground. The steering is performed by adjusting the surface of the LAR and positioning the feed at the focus appropriately.

The LAR will consist of a number of panels each of which is supported by actuators and can be tilted to adjust the shape of the reflector as shown in Figure 1.4. The cross section of the reflector must always be parabolic so as to reflect and focus the signals coming from the celestial sources to the airborne platform supporting the feed antenna and the associated electronics.

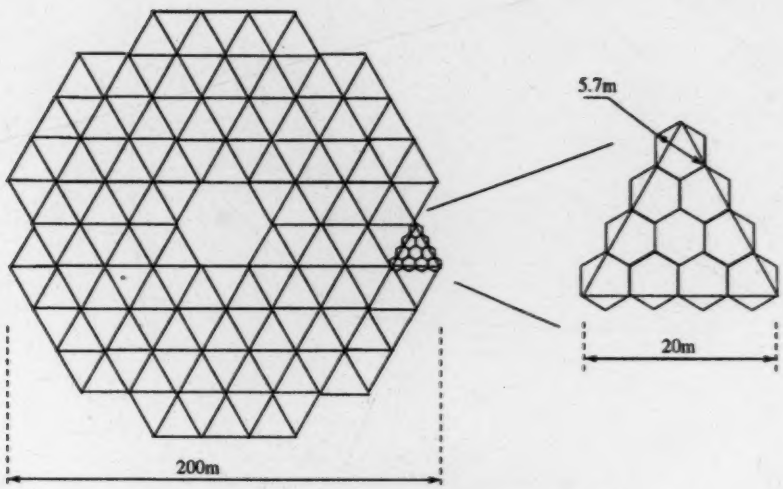

Figure 1.4: Large Adaptive Reflector.

The airborne platform is a helium filled balloon controlled by three (or maybe six) tethers. The platform will be in continuous motion.

The LAR telescope will have a multi-level control system to ensure proper position of the airborne platform at the focus of the reflector. A coarse position measurement will be obtained with a 3-D positioning system. The output of that system will control the tether motors for coarse airborne platform positioning. It will also be used to readjust the surface of the LAR. The Focal Length Measurement system will then be used to compensate for small motions of the airborne platform. This will be performed in the correlator during data processing.

At this point, the LAR telescope is being thought of as a prime focus antenna having a number of cooled receivers at the focus. The receivers will allow the LAR telescope to emulate a digital camera having as many as 180 pixels. The multi-beam telescope will have a large field of view which is one of the design requirements for the SKA.

The concept of building large telescopes based on the LAR is very revolutionary. Even though current technologies allow the construction of the LAR telescope, the technologies must be utilized in somewhat novel ways.

The LAR telescope will be the largest fully steerable telescope ever built. With the multiple feeds connected to a number of cooled receivers, the LAR will be an unprecedentedly powerful instrument for deep, wide-field, spectral imaging [53].

An LAR telescope by itself will be a very useful instrument in three major areas of radio astronomy. It will be very useful for high sensitivity and high resolution science based on VLBI techniques. The LAR telescope will aid scientists working

with low brightness spectral line science and also with continuum science [53]. Taylor et al. (1999) produced an elaborate description of the scientific implications of the LAR [53].

1.3.1 A Local Oscillator system and a Focal Length measurement system

The objective of this thesis is to recommend a suitable Local Oscillator (LO) system and Focal Length Measurement (FLM) system required by the SKA telescope. The thesis will show how to combine the two systems into one capable of achieving the required performance. It will be shown that the two systems are based on the same interferometric concepts and therefore can be combined. The combined systems will use radio-frequency signals propagating between the ground and the airborne platform.

In order for the SKA telescope to work properly, an LO system must be designed to provide coherent signals to the electronics located on board the airborne vehicles. The main purpose of the LO signal is to act as a reference signal required to shift the frequency of the received signals to much lower frequencies for subsequent transmission to the ground and digital processing. The LO system discussed in this thesis will not link every LAR antenna of the aperture synthesis telescope, however. It is assumed that there is another system delivering the phase coherent signal to the base of each LAR. The LO system discussed in this project will then deliver that phase coherent signal to the focus of the LAR telescope.

The LO system is very important for proper operation of the LAR telescope as an element in the SKA. Without the LO system the intrinsic phase relationship among the signals arriving at the foci of the many LAR telescopes will be disturbed when the signals are downconverted to low frequencies. The correlation will then be degraded, thereby decreasing the signal to noise ratio at the output of the synthesis array.

The distance between the LAR and the airborne platform is also important to know for similar reasons. If the distances from any two LAR's to their corresponding airborne platforms are not known, the intrinsic phase relationship between the two signals received by these LAR telescopes will be disturbed, producing the same effects as a phase incoherent LO system.

For these reasons the Focal Length/Local OScillator System (FLLOSS) is an important part of the SKA.

1.3.2 Location of the FLLOSS within the LAR telescope

The FLLOSS will consist of two parts. The ground part (ground unit) will have its antenna located at the centre of the LAR. The antenna will have the capability to be steered around either electrically or mechanically to track the airborne platform. The bulk of the electronic components will also be located on the ground.

The second part (remote unit) of the system will be located on the airborne platform. This part will be considerably smaller. The remote antenna will be a small patch antenna. To reduce the weight and complexity of the payload it will not be steerable .

1.4 FLLOSS specifications

The nominal target for the phase errors in the signal delivered by the LO system to the first mixer of the receiver was selected to be 5°rms at 22 GHz by the SKA design group.

As mentioned above, the uncertainty in the focal length creates effects similar to the uncertainty in the LO phase. The specification for the distance measurement was therefore set to 70 μm rms which corresponds to 1.8°rms of the phase of the 22 GHz signal [14].

The constant motion of the airborne platform and the time delay are the two limiting parameters. The spectral distribution of the airborne platform velocities is not known at the present time; however, some preliminary analysis performed by Nahon (1999) shows that for a change of wind velocity of 2.5 m/s equal to one standard deviation, σ, in the expected velocity distribution of the air at the height of the aerostat, the position of the platform will change by 0.60 m in 20 s; thus, for 5σ change in wind speed, we can expect to have the platform moving at 0.15 m/s [39]. This open loop velocity will be reduced by the airborne platform position control system. The spectral content of the velocity distribution is not expected to have high frequency components since the airborne vehicle is a massive balloon acting as a mechanical low pass filter [39].

At the beginning of the work on this thesis, the distance between the airborne platform and the LAR was intended to be 2 km; however, the distance was later reduced to 500 m by a decision of the LAR telescope design group.

An LAR telescope will require the airborne platform to move constantly across the sky to enable the telescope to track the apparent motion of the observed sources. To track a source moving at sidereal rate will require a motion of the airborne platform of 0.036 m/s (assuming that a source is moving at the rate of 15° in one hour and the altitude of the airborne platform is 500 m). Therefore, in the worst case the combination of the velocities of the airborne platform is 0.19 m/s.

1.5 Thesis layout

Chapter 2 describes different distance measurement schemes that are most widely used at the present time. The methods are compared and the most suitable scheme is suggested for use in the LAR telescope.

Chapter 3 follows with the description of different LO systems that are or have been used in radio telescopes. The selection of the LO systems is narrowed down to two most suitable systems that are later compared and the better system is selected for use in the telescope.

Chapter 4 discusses the final configuration and the suitable implementation of a complete system capable of distance measurement and delivery of the LO signal to the airborne platform. The frequencies of operation are selected and the procedure for distance measurement is discussed. The chapter does not go into discussions on LO design which is described in Chapter 5.

A prototype for the LO system is designed in Chapter 5. This chapter also describes the implementation of the prototype. Because of the time and cost considerations, the complete system was not built. However, a simplified LO prototype was constructed to test critical aspects of the LO system.

Chapter 6 summarizes the work discussed in the preceding chapters.

Chapter 2

Distance measurement systems

2.1 Introduction

A concept for a distance measurement system is selected in this chapter. The chapter begins by describing the most commonly used distance measuring methods. In the second part of the chapter the methods are compared and a concept for a distance measurement system able to achieve the distance measurement accuracy required by the SKA is suggested.

2.2 Background

2.2.1 Distance measurement

Most ranging systems based on electromagnetic techniques determine distance by transmitting a signal and analyzing changes experienced by the signal while travelling to the object of interest and back to the ranging system. There are two distinct ways to measure a distance using electromagnetic waves. One way is to transmit a signal and compare its phase with the phase of the reflected signal. The phase difference between the two signals is linearly proportional to the distance. The other way is to transmit a signal and to measure the amount of time required for it to return back.

Time-delay measuring systems can also be subdivided into two categories: pulse systems and wideband systems. A pulse system measures the time a pulse requires to return back to the transmitter, whereas a wideband system transmits a continuous wideband signal and determines the time delay by cross-correlating the transmitted signal with the returned signal. A wideband signal is usually obtained by modulating a carrier signal with a noise signal having a narrow autocorrelation function. An example of such a noise signal is pseudo-random noise (PRN).

2.2.2 Pseudo-random noise

Binary sequences that have very narrow auto-correlation functions are called pseudo-random noise since their auto-correlation functions closely resemble the auto-correlation function of white noise [48]. Generation of an approximation to white noise requires elaborate gain control and sampling or filtering circuitry that is very complicated and not very reliable [12]. Therefore PRN has become popular in recent years. As will be shown below, generation of PRN is not very complicated.

PRN sequences are common in distance ranging systems. The most important property of PRN is that each PRN sequence is easily distinguishable from a time-shifted version of itself [48]. Usually when used for distance measurements, PRN is used in conjunction with a correlator that compares the original PRN with the PRN signal which has travelled through the transmission medium. Ideally, the cross-correlation function of these two signals is a very narrow pulse so that the time delay between the two signals can be determined unambiguously. The major difference between true white noise and PRN sequences is that the latter are periodic.

The most common PRN signals considered for ranging systems are: maximum-length sequences, Golay's codes, and Barker codes.

2.2.2.1 PRN selection

There are a number of PRN sequences that are used in ranging systems. They all have different properties. In the case of the LAR, however, a very accurate distance measurement between a stationary and a moving object is the main goal of the design; therefore, it is required to select a PRN such that it would produce the least ambiguous delay measurement. The ambiguity can be a problem if the peak of the PRN auto-correlation function is not very sharp, making determination of its centre and thus the time-delay measurement less accurate.

Benkhelifa, et al. (1994) compared different PRN sequences and found that the cyclic maximum length sequences (m-sequences) and the complementary Golay's codes outperform the Barker codes [3]. The Golay's codes, the Barker codes and the m-sequences have auto-correlation functions that are only one bit wide. According to Benkhelifa et al. (1994) the Barker codes are only capable of producing a main lobe to side lobe ratio (MSR) of 30 dB whereas the MSR for m-sequences is $20\log(n)$, [dB], where n is the number of elements in a sequence (for example the ratio equals 42 dB for $n = 127$) and the theoretical MSR for Golay's codes is infinity. When the target is moving however, there is obvious degradation of MSR since the signals do not align properly in the correlator for optimum sidelobe cancellation due to the Doppler shift. Benkhelifa et al. (1994) found that when the propagating medium is absent a Golay's code is marginally better than an m-sequence in terms of MSR. However, the Golay's code requires twice as much energy to be transmitted since it really consists

of two complementary sequences. When the transmitting medium is introduced, it appears that a 1023 bit long m-sequence produces a much better MSR than the two complementary 1024 bit Golay's codes since they are designed to cancel the side lobes when perfectly lined up. However, since the target is moving and since there are some unavoidable errors in generating the signals, the 1024 bit Golay's code MSR was measured by Benkhelifa et al. (1994) to be only 30 dB whereas the 1023 bit m-sequence had a MSR of nearly 50 dB [3]. Therefore the maximum length sequence is preferred as the PRN sequence for the FLM.

The m-sequence has a number of important properties summarized by Fry (1970) [18]. The m-sequence is easily reproducible, and the reproduction is reliable and repeatable. Time-shifted versions of the sequence are easily obtainable. The bandwidth of the sequence is proportional to the clock frequency and the power spectrum is flat within the bandwidth. The mean value is zero and the variance is known. The auto-correlation function is pulse-like as was mentioned above.

2.2.2.2 PRN generation

The maximum length sequence is usually generated by shift registers with a number of modulo-two feedback elements to form a few closed loops as shown in Figure 2.1. The output of any gate is the PRN. A shift register containing N stages would gen-

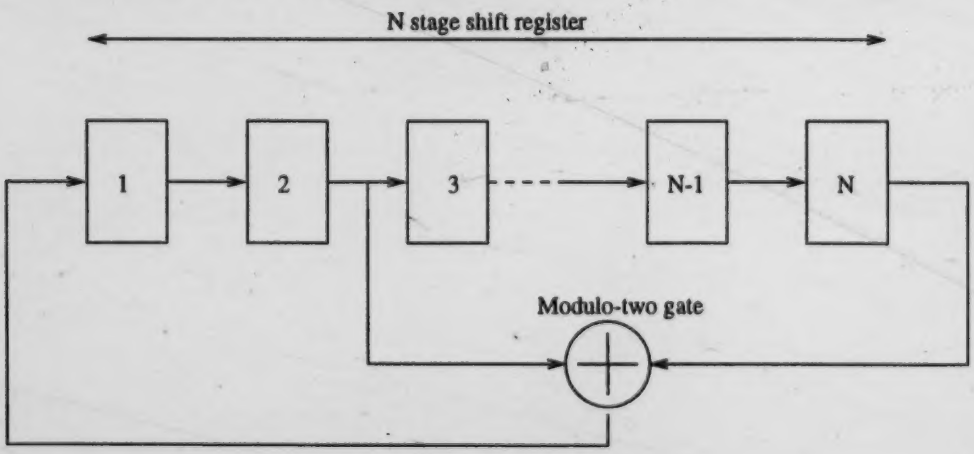

Figure 2.1: Simple PRN shift register.

erate a sequence $\left(2^N - 1\right)$ bits long. Any N-stage shift register can produce $\frac{\phi\left(2^N-1\right)}{N}$ different PRN sequences, where $\phi(k)$ is Euler's function defined as the number of integers having no common factor with k and less than k [12].

The state when all inputs to the stages in the register are zeros must be prevented since the register would stay in that state forever. Another concern with using shift registers is that some sequences may repeat themselves before $\left(2^N - 1\right)$ states are produced. In fact if the shift register has an odd number of modulo-two connections the generated sequence will not be an m-sequence [12].

2.2.2.3 Delay measurement using PRN

PRN is commonly used in distance measuring radars. A PRN signal is correlated with the version of itself reflected from a distant object. The cross-correlation of the two signals produces a more accurate measure of the time delay than any other comparison of the two signals [37], [33]. The question that arises is how accurately can the distance be measured with this configuration.

Ideally, the cross-correlation function of the PRN is the one-bit wide impulse occurring when the two inputs to the correlator are exactly lined up. However this limits the estimate of the time delay to the period of a single pulse of the PRN since it is impossible to determine where exactly inside the period the inputs line up. To improve on this, the PRN can be over-sampled. This results in the impulse appearing as a triangular function spread over a number of new sampling periods. The time delay can be interpolated by fitting the triangular shaped function to the output of the correlator.

In reality, the cross-correlation function will only appear as a triangular function when the PRN signal is not band-limited. The PRN signal will most likely be band-limited by $H_{lim}(f) = \frac{1}{\sqrt{B_w}}\left[u(f + \frac{B_w}{2}) - u(f - \frac{B_w}{2})\right]$ affecting the power spectral density of the input signal, $S_0(\omega)$. The output spectral density of the signal will become $S(\omega) = S_0(\omega)\left|H_{lim}(\omega)\right|^2$. Note that the auto-correlation function and the power spectral density are related through the inverse Fourier transform: $R(t) = \mathcal{F}^{-1}(S(\omega))$. The autocorrelation function in the band-limited case becomes $R(t) = R_0(t) * h^*_{lim}(-t) * h_{lim}(t)$, where $h^*_{lim}(-t) * h_{lim}(t) = \mathcal{F}^{-1}\left(\left|H_{lim}(\omega)\right|^2\right) = \frac{1}{\sqrt{B_w}}\mathcal{F}^{-1}\left(H_{lim}(\omega)\right)$ since $\left|H_{lim}(f)\right|^2 = \frac{H_{lim}(f)}{\sqrt{B_w}}$. The auto-correlation of the band-unlimited PRN approaches the impulse function, therefore the convolution $R(t)$ of $R_0(t)$ and $h^*_{lim}(-t) * h_{lim}(t)$ is a sinc function

$$R(t) = \frac{1}{\sqrt{B_w}}\int_{-\frac{B_w}{2}}^{\frac{B_w}{2}} H_{lim}(f)e^{j2\pi ft}df = \frac{\sin(\pi B_w t)}{\pi B_w t} = Sa(\pi B_w t). \qquad (2.1)$$

To estimate the actual time delay the sinc function is fitted to the correlator output. The function will be centered on the time delay.

A correlator was simulated using MATLAB software. The effects of oversampling, correlation time, length of the PRN sequence, and the signal to noise ratio (SNR)

were investigated. First, the simulations showed that the sinc function, S_a, does represent the correlator output quite well. Second, the accuracy of the time delay measurement was inversely proportional to the SNR.

2.2.3 Atmospheric effects

Since the signals in the measurement system will travel in the atmosphere, the effects of its inhomogeneity must be considered.

The atmosphere can be divided into a number of spheres with different thicknesses. Two main divisions are the neutral atmosphere and the ionized atmosphere. These regions are also subdivided into subregions. The region of interest here is called the homosphere, and is divided into troposphere, stratosphere and mesosphere. The troposphere is about 10 km in height and is the prime concern for the FLM system [1].

Phase scintillations are not as dominant as amplitude scintillations in the troposphere but are more important for ranging systems. Phase and amplitude effects are variable with frequency. Phase scintillations essentially spread the signal in time and amplitude scintillations affect the received signal amplitude. Some systems apply pre-emphasis across the bandwidth at the transmitting end to remove some effects of scintillations and to have reasonably uniform characteristics in phase and amplitude across the whole bandwidth [1]. Pre-emphasis assumes that the amplitude and phase effects are monotonic with frequency, which is true for narrowband signals. If this assumption does not hold, dispersion effects may appear.

A group of electromagnetic waves propagates with a group velocity $v_{gr} = -\frac{df}{d\lambda}\lambda^2$ and each electromagnetic wave has its phase velocity $v_{ph} = \lambda f$ [25]. Differentiating the latter equation, one obtains an expression $dv_{ph} = fd\lambda + \lambda df$ that implicitly contains the dispersion, i.e. the dependence of the phase velocity on the wavelength [25]. Another way of expressing the wave propagation in a medium uses the notion of a refractive index $n_{ph} = \frac{c}{v_{ph}}$ and $n_{gr} = \frac{c}{v_{gr}}$. Of course, refractive indices change with frequency, chemical composition of the air and atmospheric conditions. Note here that, knowing n_{ph}, one can find n_{gr} in the following fashion: $n_{gr} = n_{ph} + f\frac{dn_{ph}}{df}$ [25].

The dispersion can be of two kinds: normal dispersion and anomalous dispersion [29]. Anomalous dispersion happens when the radio frequency approaches absorption bands of various chemicals found in the air. In those regions, the phase changes very rapidly. There exist several models to approximate the index of refraction of radio waves. Sellmeier's equation is one of the most successful expressions to approximate n_{ph}; it states that $n_{ph}^2 = 1 + \sum_i \frac{A_i\lambda^2}{\lambda^2 - \lambda_i^2}$, where λ_i is the wavelength of the natural frequency of particles found in the air and A_i is a constant proportional to the number of particles capable of vibrating at frequencies corresponding to λ_i [29].

This expression works very well far from absorption lines and in close proximity to them; however, it fails completely when the frequency coincides with the absorption bands.

It is possible to measure atmospheric conditions in real time. There are some narrowband devices that are used for measuring the indices of refraction [22]. Although they cannot be employed to survey large bandwidths, they might be used to obtain the initial conditions for evaluation of some unknowns used in a number of algorithms (for example those described in [38], [13]) that have been created to correct for atmospheric effects.

An analysis of atmospheric effects on signals travelling from satellites in the 10 GHz – 30 GHz frequency range and in the presence of rain shows that the signal phase changes linearly with frequency for signals having bandwidths less than 500 MHz unless they are very close to the water absorption band of 22 GHz [51]. It seems likely that dispersion effects may be ignored in most satellite communications systems utilizing instantaneous bandwidths of less than 1% of the carrier frequency as long as the amount of water in the air is not excessive [1], [11]. For the FLM system these effects are even less significant because the distance between the objects is much shorter and the ionosphere does not affect the signals. Therefore, dispersion can be ignored at least in the initial stage of the FLM system design.

Effects such as reflections from atmospheric layers tend to be most significant at frequencies below 1 GHz [23]. The phenomenon of "ducting" happens mostly above water and only when signals propagate in nearly horizontal directions and can be ignored here [10].

2.2.4 Cycle slips, Multipath and Doppler shift

The reflected signal always acquires a Doppler shift relative to the transmitted signal due to movement of the reflecting object. The time shift and the frequency shift cannot be determined simultaneously [34]. The Doppler shift will appear as a drift of the phase in phase-measuring ranging systems.

The FLM system will consist of two antennas pointed directly at each other. The directivity of the antennas will be discussed later but for now it is sufficient to say that at least one of the antennas will have narrow beamwidth in order to reduce coupling with the similar ranging systems used in other LAR telescopes in the SKA. A narrow beamwidth will significantly reduce multipath related problems. Some other ways of removing multipath will be discussed in Sections 2.5.2 and 2.5.3.

Cycle slips usually appear in PRN systems having low signal to noise ratio. This phenomenon should not be a problem since it should be possible to have a very high SNR in a system having two closely located antennas pointed directly at each other. However, if a cycle slip does occur, it can be determined very easily by plotting the

phase data with time.

2.2.5 System noise

Noise is always present in any communication system. Noise is received by antennas and produced by internal devices. It is added to the signal and cannot be completely removed, although it can be made smaller relative to the signal by using phase locked loops, for example. The measure of noise in a signal is the signal to noise ratio (SNR). The SNR limits the accuracy of measurements and needs to be taken into account.

2.2.6 Linear combination of signal phases

If a signal of frequency f is generated from two signals of frequency f_a and f_b with $f = n_b f_a + n_b f_b$, then the phase of the signals so generated is:

$$\varphi = n_a \varphi_a + n_b \varphi_b = n_a f_a t + n_b f_b t = ft, \tag{2.2}$$

where n_a and n_b are integers.

Knowing phases of φ_a and φ_b, the phase of any signal generated from a combination of f_a and f_b can be calculated.

2.3 Summary of different ranging systems

Free space is the transmission medium for the FLM system. There are a number of ranging systems that can operate in free space. This section will discuss different alternatives for the FLM system.

2.3.1 Laser-based ranging systems

One possible way of measuring a distance is by using optical instruments–that is, lasers. There are a number of laser-based instruments currently used for ranging in industry and space exploration.

There are two distinct kinds of laser-based ranging systems employed for distance greater than about 100 m: the beam-modulation telemetry system and the pulsed laser system.

In beam-modulation systems, the laser output is modulated by a sweep frequency. The phase of the return signal is then compared with the phase of the emitted signal. The modulating signal is designed so that by measuring a number of phases during one sweep cycle one can resolve 2π phase ambiguity. Combining the measured phases, the distance of interest is obtained.

On the other hand the pulsed laser system, also known as optical radar or LIDAR (LIght Detection And Ranging), measures the round-trip time of very short pulses emitted by the laser. These devices are most common in satellite tracking and military range finding.

2.3.2 RF pulse technique

The RF pulse technique is based on measuring the round-trip time of the pulse travelling to the object and back to the ranging device. This technique is widely used in radar. Time measurements are very important since for example an error of 2 ns corresponds to a distance error of 0.3 m. Very complicated electronics is required to achieve the precision needed to measure distance with an accuracy of a few micrometres.

2.3.3 Correlator techniques

A cross-correlation detector measures a distance by comparing a signal sent out to the distant point and reflected back, with a reference signal available inside the detector. By shifting the reference signal in time the detector determines the time shift, τ, at which the correlation function is maximum. That time corresponds to the time delay experienced by the travelling signal. SNR is greatly improved by cross-correlation since the interference components are averaged out.

Signals having a very wide bandwidth so as to minimize the correlation time are the prerequisite to this method. The wideband method is similar to the pulse method used in radar systems with the only difference that the signal is available all the time [34]. The frequency bandwidth, BW, or the shortness of the correlation function of the signal determines the attainable resolution [34]. The shortness of the correlation function is reciprocal to the bandwidth.

This technique is employed in many FM altimeter designs. There are two main methods. One method is to vary the frequency of a carrier by means of a sinusoidal voltage; the other is to modulate a carrier by means of a non-periodic noise voltage [34]. Some techniques based on these methods are described in the following subsections.

2.3.3.1 Wideband noise modulation

The transmitted carrier is wideband modulated by white noise or a noise-like signal. Let us consider band-limited white noise with power spectrum, $S_{wn}(f)$, shown in Figure 2.2. The auto-correlation function, $A(t)$, of the white noise is

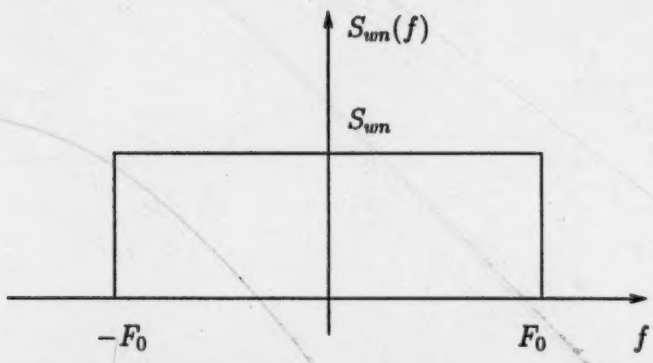

Figure 2.2: Power spectrum of band-limited white noise.

$$A(t) = \int_{-\infty}^{+\infty} S_{wn}(f) e^{j2\pi ft} df = 2F_0 S_{wn} \frac{\sin(2\pi F_0 t)}{2\pi F_0 t}. \tag{2.3}$$

The auto-correlation function is plotted in Figure 2.3. Equation 2.3 shows that the wider the modulating bandwidth the narrower the main lobe of the sinc function (or $\frac{\sin(x)}{x}$ function) produced by a cross-correlator receiver and, therefore, the accuracy of time measurement increases since the tip of the cross-correlation function becomes sharper and, thus, less ambiguous.

An altimeter based on the wideband noise modulation technique was first implemented by Horton (1959) [27]. The wideband modulation was accomplished by modulating a carrier with white Gaussian noise. The altimeter employed correlation techniques to measure the delay time between the transmitted and the received signal.

The true white noise may be replaced by a PRN signal. A good PRN signal has a very narrow auto-correlation function as described in more detail in Section 2.2.2. A PRN signal is a periodic binary sequence $y(t)$ with the cross-correlation function $C_{ij}(\Delta t)$ as follows:

$$C_{ij}(\Delta t) = \frac{1}{\tau} \int_{t_0}^{t_0+\tau} y_i(t) y_j(t+\Delta t) dt = \begin{cases} 1 & if \quad \Delta t = 0 \\ 1 - \frac{|\Delta t|}{T} & if \quad |\Delta t| \leq T \\ \approx 0 & if \quad |\Delta t| > T \end{cases} \tag{2.4}$$

where T is the period of pulses in $y(t)$. The sinc function is replaced by a triangular function [36]. This correlation function is continuous, which allows one to track the time delay between two signals. Consider Figure 2.5. Imagine the receiver-generated code being shifted in time until the output of the correlator is 1. The time shift or time delay is the measure of the distance between the transmitter and receiver. Even

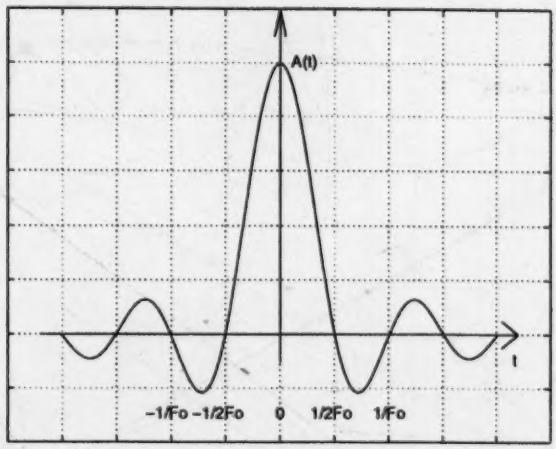

Figure 2.3: Auto-correlation function of band-limited white noise.

if the PRN signal is dominated by external unwanted noise, when added statistically, many samples increase the correlation to a level that can be detected.

2.3.3.2 Sinusoidal sweep frequency modulation

Here the transmitted carrier is frequency modulated by a wideband frequency sweep. The transmitted signal is reflected back from the distance object. The time it takes for the signal to get back to the transmitter can be found by comparing the frequencies of the reflected signal and the transmitted signal. The longer it takes for a reflected signal to get back the larger the difference is. The difference can be measured with a frequency meter or a correlator.

2.3.3.3 Bandwidth synthesis

If wideband modulation becomes too expensive, bandwidth synthesis schemes might be used as a substitute. The band is synthesized using smaller frequency bands. The frequency separation of the bands is normally optimized with a computer simulation as no single formula exists to determine which pattern is the best. The problem of choosing the frequencies is similar to finding a minimum redundancy distribution of antenna spacing in an array [46], [54]. The main criterion when choosing the frequency pattern is the effect of the band locations on the output of the cross-correlator. Some combinations produce higher sidelobes in the correlator output

than others, making selection of the correct peak more complicated. The bands are placed in some geometrical sequence with increasing separation so that the phase can be determined going from one band to the next [54]. Also, the pre-emphasis technique is used to effectively enlarge the bandwidth of the signal.

2.3.4 Tellurometer distance measurement scheme

A tellurometer is an instrument that measures the electrical distance between two objects by measuring phases of different microwave signals [19], [47]. The following description of tellurometer operation and frequencies used are based on work published by Saastamoinen (1967) [47].

2.3.4.1 System structure

The basic tellurometer system consists of a remote unit (RU) and a master unit (MU) having slightly different carrier frequencies. Let us assume that the MU carrier frequency is 10.050 GHz and the RU carrier frequency is 10.083 GHz. The block diagrams of the RU and MU are shown in Figure 2.4.

The carrier frequency is frequency modulated by the pattern frequencies shown in Table 2.1. Different frequencies are simulated using linear combination concepts similar to those described in Section 2.2.6. The phases of the simulated frequencies are then measured and analyzed. Note that the MU and RU frequencies differ by 33 MHz and the RU and MU pattern frequencies differ by 1 kHz.

	RU pattern frequency, MHz		MU pattern frequency, MHz
A	7.492377	A+	7.491377
		A-	7.493377
B	7.490879	B	7.489879
C	7.477392	C	7.476392
D	7.342529	D	7.341529
E	5.993902	E	5.992902

Table 2.1: MU and RU pattern frequencies (adapted from [47]).

2.3.4.2 System operation

At the RU, the RU frequency-modulated carrier and the MU frequency-modulated carrier are mixed together to obtain a 33 MHz IF signal amplitude-modulated by a 1 kHz signal. The 1 kHz signal is the difference between corresponding modulating patterns. The 1 kHz is then used to frequency modulate a 100 kHz subcarrier. This

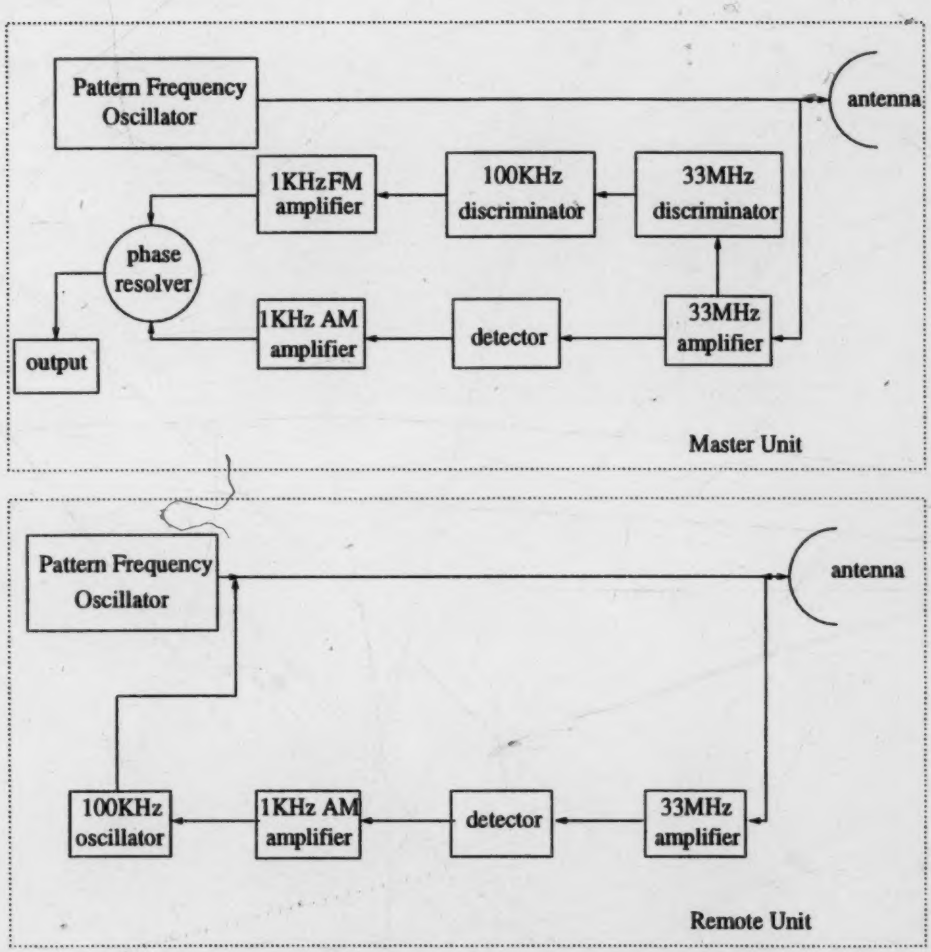

Figure 2.4: Tellurometer block diagram (adapted from [47]).

100 kHz subcarrier frequency modulates the RU carrier. Thus, the RU carrier is frequency modulated by one of the pattern frequencies and by the 100 kHz subcarrier, which is in turn frequency modulated by the 1 kHz signal.

At the MU, the RU signal and the MU signal are again mixed together to produce a 33 MHz IF signal which is again amplitude modulated by the 1 kHz signal and frequency modulated by the 100 kHz subcarrier. The 1 kHz signal amplitude modulating the 33 MHz IF is then compared to the 1 kHz signal modulating the 100 kHz signal. A phase meter is used to measure the phase difference of the two 1 kHz signals.

Usually, the MU pattern frequency, f_M, is 1 kHz higher than the corresponding RU pattern frequency, f_R, so that the phase difference resulting from mixing is related to $f_M - f_R$. When travelling from the MU to the RU, the MU pattern undergoes a phase retardation equal to the number of wavelengths contained in the distance travelled. Similarly, the RU pattern experiences phase retardation going from the RU to the MU.

Let the distance between the MU and the RU contain N_M whole wavelengths λ_M and a fraction x of one wavelength of the MU pattern frequency f_M. At the RU, the f_M signal phase will be $\varphi_M = 360x°$. Similarly, for the RU pattern frequency, let the distance between the RU and the MU contain N_R whole wavelengths λ_R and a fraction y of the remote frequency f_R wavelength. At the MU, the phase of the f_R signal will be $\varphi_R = 360y°$. Now, one can see that the difference $f_M - f_R$ produces a 1 kHz signal and a phase difference $-\varphi_R$ at the MU and φ_M at the RU. The phase difference produced at the RU is returned back to the MU. Let the distance between the MU and the RU contain N_{M-R} whole wavelengths at 1 kHz and a fraction z. The wavelength of the difference frequency would be $\lambda_M - \lambda_R$ and the phase would be $360z = \varphi_M - \varphi_R$. Therefore, the return signal arrives at the MU with a phase retarded by $(\varphi_M - \varphi_R)°$.

Now the difference $(f_M - f_R)_R$ produced at the RU and the difference $(f_M - f_R)_M$ produced at the MU are compared at the MU. The total angle is $\varphi_R + \varphi_M + (\varphi_M - \varphi_R) = 2\varphi_M$. Thus, the phase between the two 1 kHz signals equals $2\varphi_M$.

The reason for having more than one pattern frequency is that tellurometers need to resolve 2π phase ambiguities. Tellurometers use linear combinations of frequencies to simulate other frequencies. This lets tellurometers increase the maximum measurable distance and resolve phase ambiguities without covering a wide band of frequencies. For example the "A-" pattern frequency allows a signal with a frequency equal to "2A" to be simulated [47].

2.3.5 Global Positioning System

The Global Positioning System (GPS) is effectively a combination of some of the ranging systems described above. It is the most commonly used distance measuring system at present. The following description of GPS operation is mostly based on work published by Hofmann-Wellenhof, et al. (1993) [25].

2.3.5.1 GPS signal structure

An oscillator on board every satellite produces a fundamental reference signal $f_0 = 10.23$ MHz with stability in the range of 10^{-13} ppm over a day. All other frequencies are derived from this reference and are summarized in the Table 2.2 .

Component		Frequency, MHz
Fundamental frequency	f_0	10.23
Carrier L_1	$f_1 = 154 f_0$	1575.42
Carrier L_2	$f_2 = 120 f_0$	1227.60
Precision code (P-code)	f_0	10.23
Coarse/Acquisition code (C/A code)	$f_0/10$	1.023
Navigation message (NM)	$f_0/204600$	$50 \text{x} 10^{-6}$

Table 2.2: Components of the GPS satellite signal [25], [50].

Carriers L_1 and L_2 are modulated with the navigation message (NM) described below and PRN codes. The PRN C/A-code is repeated every millisecond whereas the PRN P-code is repeated every 266.4 days. These codes are specific to every particular satellite and are used to identify the source of data received by a receiver among other things. The navigation message is 1500 bits long at the frequency of 50 Hz and is transmitted in 30 seconds.

The following equation describes two signals sent from every satellite:

$$L_1 = C_p(t) M_N(t) \cos(f_1 t) + C_{c/a}(t) M_N(t) \sin(f_1 t) \tag{2.5}$$

$$L_2 = C_p(t) M_N(t) \cos(f_2 t) \tag{2.6}$$

where $C_p(t)$ and $C_{c/a}(t)$ are the PRN P-code and the PRN C/A code respectivelly, and $M_N(t)$ is the navigation message.

The navigation message contains information on the satellite clock, the orbit, the satellite health status, and various correction data. The total message consists of five subframes, each of which is six seconds long and consists of ten words thirty bits long.

Each subframe starts with the telemetry word (TLM) containing a synchronization pattern and some diagnostic messages. The hand-over word (HOW) is the second word in every subframe. It contains the identification information and gives the Z-count for the next subframe. The Z-count is the GPS satellite clock time at the leading edge of the next data subframe.

GPS positioning techniques generally assume that signals from more than one satellite are available.

2.3.5.2 Code Pseudorange

The basic idea of this approach to distance measurement is that, if the time required by a signal to reach the ground receiver is known, one can derive the distance between the ground and the satellite by multiplying the time difference by the speed of the electromagnetic waves. The problem with this approach is that the clock on board a satellite and the clock on the ground have to be synchronized. Any discrepancies would result in error.

The time difference is $\Delta\tau = (t_r - t_s) + \Delta\delta$, where t_r is the time shown by the ground receiver clock, t_s is the time of transmitting the message obtained using the correlation technique, and $\Delta\delta$ includes the receiver clock discrepancy, the atmospheric delays and some other biases. Thus the distance from the ground to the satellite is $R = c\Delta\tau = \rho + c\Delta\delta$, where ρ is the true distance.

Similar to the discussion in Section 2.3.3.1, the cross-correlation function of the PRN signal is represented by a triangular shaped function as shown in Figure 2.5. Again the receiver generated code is shifted in time until the output of the correlator is 1. The time shift gives the information on the path the signal has travelled before reaching the receiver provided that the satellite clock and the receiver clock are synchronous. Since the C/A code is only 1 ms in duration the ambiguity is 1 ms which implies a 300 km uncertainty. The simplest way to remove the ambiguity is to observe the transition in the TLM and detect the preamble in the TLM containing the information needed by the user [36].

Locking and tracking are accomplished by the delay lock loop (DLL). Some implementations of the DLL may use two correlators.

Once the PRN code is removed, one can read the NM. Using the NM data, the satellite location and the satellite time are obtained. With that information, the receiver position can be calculated. This method is very fast but not as accurate as other methods.

2.3.5.3 Phase Pseudorange

The carriers are phase shift keying (PSK) modulated by the NM and the PRN. It is easy to see that by squaring the signal, one can free the carrier from the modulating

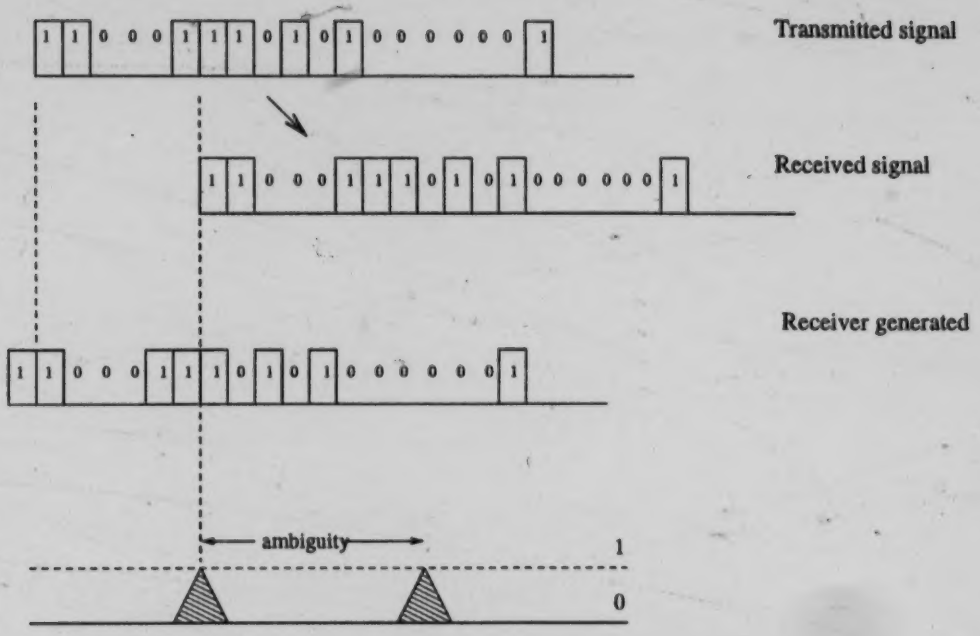

Figure 2.5: C/A code correlation (adapted from Leick (1995) [36]).

PRN codes and the NM.

The phase difference between the satellite carrier and the reference ground carrier is, as described by Leick [36]:

$$\varphi_r^s(t) = \varphi_r(t) - \varphi^s(t) + N_r^s(1) + I_{r,\varphi}^s(t) + \frac{f}{c}T_r^s(t) + d_{r,\varphi}(t) + d_\varphi^s(t) + d_{r,\varphi}^s(t) + \epsilon_\varphi, \quad (2.7)$$

where $\varphi_r(t)$ and $\varphi^s(t)$ are the receiver signal phase and the received satellite signal phase at time t, $N_r^s(1)$ is the initial integer ambiguity, $I_{r,\varphi}^s(t)$ and $T_r^s(t)$ are the ionospheric and tropospheric effects, $d_{r,\varphi}(t)$ and $d_\varphi^s(t)$ are hardware delays, $d_{r,\varphi}^s(t)$ is the multipath phase contribution and ϵ_φ denotes the random noise. Section 2.3.5.4 describes the procedure for obtaining the distance from the phase pseudorange.

2.3.5.4 Distance Measurement

For high-precision surveying the phase pseudorange is favored [36]. However, more and more systems employ both phase and code techniques to increase the accuracy of measurements [25], [36]. Also, different linear combinations of the carrier frequencies are used to obtain phase measurements at different simulated frequencies [36]. The

following are the most popular techniques for distance measurement employed in GPS receivers.

Single frequency phase data: A number of measurements are made. The data are modelled by Equation 2.7. In this approach errors which are not modelled affect all estimated parameters. To correct for this, the ambiguity ($N_a = N_r^s(1)$) is measured as a real value. Once N_a has been approximated, the value of N_a closest to an integer and having the smallest uncertainty is considered as the most reliable [25].

Double frequency phase data: A frequency $f_w = 347.82$ MHz is obtained by subtracting L_2 from L_1. The wavelength, $\lambda_w = 86.2$ cm, is significantly longer than $\lambda_{L_1} = 19.0$ cm and $\lambda_{L_2} = 24.4$ cm.

Equation 2.7 can be rewritten to simplify the analysis in the following way:

$$\Phi = \frac{1}{\lambda}\rho + \frac{c}{\lambda}\Delta\delta + N_a + I^s_{r,\varphi}(t), \tag{2.8}$$

where $\Phi = \varphi^s_r(t)$, $N_a = N^s_r(1)$, ρ is the distance between the satellite and the ground, and $\Delta\delta$ combines all other errors. The $I^s_{r,\varphi}(t)$ can be approximated by $\frac{1}{\lambda}\frac{A}{f^2}$ [25], [50]. The $\Phi_{L_1-L_2}$ (or Φ_w) then is

$$\Phi_w = \frac{f_w}{c}\rho + f_w\Delta\delta + N_w - \frac{A}{c}(\frac{1}{f_1} - \frac{1}{f_2}). \tag{2.9}$$

From Equations 2.8 and 2.9, one can obtain the following:

$$N_{L_1} = \Phi_{L_1} - (\Phi_w - N_w)\frac{f_1}{f_w} + \frac{A}{c}\frac{f_1 + f_2}{f_1 f_2}. \tag{2.10}$$

A similar equation can be derived for N_{L_2}. It is important to note that terms containing ρ and $\Delta\delta$ have disappeared. However, they are implicitly included in the N_w term. The ionospheric term cancels for short baselines with similar ionospheric conditions; however, it can introduce errors for longer baselines [25].

There are two other useful linear phase combinations to be considered. They are: $\varphi_{L_1+L_2}$ and $\varphi_{L_3} = \varphi_{L_1} - \frac{f_2}{f_1}\varphi_{L_2}$. φ_{L_3} is used to remove the effects of the ionosphere. $\varphi_{L_1+L_2}$ simulates a frequency with much smaller wavelength for better accuracy.

Double frequency phase and code data: The biggest cause of errors in the previous technique is the ionospheric term. Its effects can be eliminated by combining the phase and code data. Consider the following four equations:

$$\Phi_{L_1} = \frac{\rho}{c} f_1 - \frac{A}{c}\frac{1}{f_1} + N_{L_1} + f_1 \Delta\delta \tag{2.11}$$

$$\Phi_{L_2} = \frac{\rho}{c} f_2 - \frac{A}{c}\frac{1}{f_2} + N_{L_2} + f_2 \Delta\delta \tag{2.12}$$

$$R_{L_1} = \frac{\rho}{c} f_1 + \frac{A}{c}\frac{1}{f_1} + f_1 \Delta\delta \tag{2.13}$$

$$R_{L_2} = \frac{\rho}{c} f_2 + \frac{A}{c}\frac{1}{f_2} + f_2 \Delta\delta \tag{2.14}$$

Equations 2.11 and 2.12 describe frequency phase ranging while Equations 2.13 and 2.14 describe code ranging.

Using these, one can find that

$$N_w = \Phi_w - \frac{f_1 - f_2}{f_1 + f_2}(R_{L_1} + R_{L_2}). \tag{2.15}$$

This equation enables one to determine the ambiguity N_w regardless of ionospheric effects and independent of the length of the baseline. The only problem which remains is the multipath problem, which can be removed by averaging signals over a period of time.

Having obtained the value for N_w and using Equation 2.11 and Equation 2.12, one can derive equations for N_{L_1} and N_{L_2} that are not affected by the ionosphere:

$$N_{L_1} = \frac{f_1}{f_w}\Phi_{L_1} - \frac{f_2}{f_w}(\Phi_{L_2} + N_w) - (\frac{\rho}{c} + \Delta\delta)(f_1 + f_2). \tag{2.16}$$

Other techniques: Other techniques such as search techniques and the ambiguity function method are also used [25]. They are usually insensitive to cycle slips but very time consuming.

2.4 Measurement accuracy

2.4.1 Laser-based devices

Distance ranging laser-based systems have been widely used for over 25 years for military and surveying applications. However, the accuracy of these devices is no better than 1 mm for distances of up to 1000 m and is even worse for larger distances [44], [58]. A laser system capable of measuring deflections of the reflector shape at the Green Bank Telescope (GBT) is sensitive to extremely small distance changes. It is

capable of detecting deflections of less than 50μm at distance of over 700 m; however, the absolute distance measurement is not more accurate than a few millimetres [21], [43].

2.4.2 Wideband noise modulation

The accuracy of this method depends on how accurately the peak of the correlation function can be obtained.

If the accuracy is not a major concern, the time delay is obtained directly with a cross-correlator. The maximum of the correlator output will occur at the time delay that corresponds to the time taken by the signal to reach the cross-correlator. This method is only accurate to the resolution of the time measurement.

For better accuracy of distance measurement, the PRN code can be resampled at higher frequency and a known expected function can then be fitted to the output of the cross-correlator. The centre of the function will produce a much more accurate measurement of the time delay. The simulations mentioned in Section 2.2.2.3 suggested that the accuracy of time measurement in a correlator is inversely proportional to the SNR. As a rule of thumb the measurement accuracy of the time delay is related to the signal SNR as follows:

$$accuracy \approx \frac{1}{f_{PRN} \times SNR}, \text{ [s]}, \tag{2.17}$$

where f_{PRN} is the frequency of PRN and SNR is a unitless signal to noise ratio.

2.4.3 Sinusoidal sweep frequency modulation

Once the cross-correlation function is obtained, the accuracy of measurements in this case is similar to the one described in Section 2.4.2. However, wide bandwidth of the sweep signal is more complicated to achieve and the maximum of the sinc function is not as well defined as the maximum of a triangular function.

2.4.4 Bandwidth synthesis

This scheme cannot be more accurate than the wide bandwidth scheme because the removal of frequency components removes some information from the signal. Otherwise, in a limiting case of leaving the carrier modulated by a single CW, one would create an absolutely accurate system which is obviously not true.

2.4.5 Tellurometer

A tellurometer measures the distance between two objects in terms of fractions of wavelengths. The accuracy of measurement depends on stability of the signals and the electronic components used. With today's instruments, the accuracy of phase measurement is about 0.1% of wavelength. Thus, provided other errors have been calibrated out, the tellurometer accuracy may be as high as 0.1% of the smallest wavelength.

2.5 Sensitivity to errors

2.5.1 Laser-based systems

A system suitable for the LAR must operate in an uncontrolled environment. At wavelengths as small as 650 nm the environment plays a very important role since high-frequency signals are greatly sensitive to temperature changes, pressure changes and chemical composition changes of the atmosphere. According to Ready (1997) the atmospheric changes are in fact the limiting factor in laser-based ranging instruments [44]. Even the rangefinder employed at the GBT is very susceptible to errors due to the atmospheric conditions. In fact, even though the system is capable of measuring deflections of the surface shape of the order of 20μm at a 100 m distance, changes of a few millimetres in the measured distance are possible due to changes of atmospheric conditions [43].

2.5.2 Correlator-based systems

As discussed in Section 2.2.3, atmospheric effects do not affect RF signals as long as their relative bandwidth is in the order of a few percent. In fact GPS research shows that most errors in correlator-based systems are caused by multipath [57]. The other errors are usually averaged out in the correlator. There are several multipath mitigation techniques developed primarily for GPS system. The most promising technique uses the full PRN bandwidth in the correlator. The full bandwidth encompasses many spectrum sidelobes. This technique produces the best ranging accuracy and multipath mitigation [57].

2.5.3 Phase measuring systems

The dominant cause of errors in this technique is multipath. It appears to be much more difficult to combat multipath errors in pure phase measuring systems simply because it is impossible to distinguish between two signals entering the receiving antenna with the same frequency but different phase. Most methods for multipath

mitigation in phase measuring systems are based on designs of low sidelobe antennas. However, these techniques are not very effective [57].

2.6 Conclusion

Comparison of pulse radar and correlation techniques reveals that the wideband PRN modulation technique is the best scheme for the FLM system. Lange (1967) concluded that the wideband technique is superior to the pulse technique if the distance to only one object is to be measured and the effort to achieve the required performance with the pulse technique is not worthwhile [34]. The bandwidth synthesis technique is not as accurate as other wideband schemes as mentioned above in Section 2.4.4. Lange (1967) also determined that noise modulation is preferred over sinusoidal signal modulation because the time delay indication is very clear and different objectives can be achieved by choosing different noise configurations [34].

Laser-based systems generally require higher levels of maintenance than RF systems since any dust build-up on the laser lenses affects the device performance, thus increasing the operating cost of the devices. It is also more difficult to keep a very narrow laser beam pointed directly on a target whose attitude and altitude change constantly. There has not been built a laser-based ranging system that would achieve the accuracy of 70 μm over distances of a few hundred metres. The laser pointing and the operating cost of that system would make it unsatisfactory for the FLM and therefore laser-based systems will not be considered as an FLM alternative.

The GPS by itself will not be able to achieve the required accuracy [25]. However, the idea of combining different schemes may be adapted for the FLM. The wideband PRN part would be very useful since it simplifies ambiguity resolution, produces useful information on multipath, and produces the transfer function of the propagation medium. However, to achieve an accuracy of 70 μm with a correlator that has a resolution of, for example, 0.1% of the PRN code period, the frequency of the PRN signal according to Equation 2.17 should be:

$$f_{PRN} = \frac{0.001}{\left(\frac{70\times10^{-6}}{3\times10^{8}}\right)} \approx 4.3 \text{ GHz}, \tag{2.18}$$

where 3×10^8 m/s is the speed of the electormagnetic signal and 0.001 corresponds to the SNR of the correlated signals. At the present time, it is not possible to create such a PRN signal. Therefore, the correlator-based system by itself will not be able to achieve the desired accuracy. Thus, it is necessary to measure the phase of a high-frequency signal to ensure adequate accuracy of the distance measurement.

The true tellurometer technique will not be used in the FLM system but it will be altered to increase the speed of measurements and to remove unnecessary

complications that have to do with unavailability of a phase coherent signal at the remote end. The FLM system will have a number of CW signals available for phase measurements. Phase measurements will be performed in parallel in contrast with true tellurometers.

The final configuration of the FLM system will be selected in Chapter 4. The CW signals available for distance measurement will be selected there and therefore the decision of whether the ambiguity resolution is required or not will be discussed then. However, a combination of a CW phase measurement scheme and a correlator scheme is suggested to provide accurate measurements of the focal distance. The PRN sequence, if required, will provide the measurement of the time delay to resolve phase ambiguity whereas CW signals will be used to achieve high accuracy of distance measurement. Use of different frequencies will enable the system to employ various phase processing techniques used in both GPS systems and tellurometer systems.

A more detailed discussion and design of the FLM system will be presented in Chapter 4.

Chapter 3

Local Oscillator System

3.1 Introduction

A local oscillator system for the LAR telescopes is selected in this chapter. The chapter starts with a brief description of control system concepts necessary to understand the operation and the selection process of different LO systems. The two most suitable systems are then compared and the better one for the SKA is selected and recommended. A more detailed design of the LO system is discussed later in Chapter 5.

3.2 Background: Control systems

One of the goals of this project is to design a system that will provide a phase and frequency controllable signal to the airborne platform. The phase may not be constant as it might have to be changed to compensate for apparent movement of observed objects on the sky. The phase must be controlled however. Thus, a control system is required. Moreover, there is a physical distance separating the airborne platform and the reference frequency source on the ground. The signal path length cannot be assumed constant as the airborne platform is in continuous motion and various weather effects such as temperature will alter the transmission medium properties, altering signal propagation times and thus the phase of the signals. The control system must, therefore, be able to adjust the phase of the signals somehow to compensate for the disturbances in the transmission medium. That will be achieved by feeding back some information about signal properties to the control system. In this control system, the phase delivered to the airborne platform will be the controlled variable.

3.2.1 Control system theory

Commonly a control system is represented by a block diagram which identifies major components of the system, shows the directions of information flow from one component to another, but omits details. An example of a block diagram is shown in Figure 3.1, where $R(s)$ is the reference input, $C(s)$ is the controlled variable, $G(s)$ is a transfer function of a process or a plant, $H_{fb}(s)$ is the transfer function of the feedback element, $E(s)$ is the actuating signal which is related to the discrepancy between the reference signal and the controlled variable, and $D(s)$ is a disturbance added to the system. Depending on the given situation a control system designer might be able to alter $G(s)$.

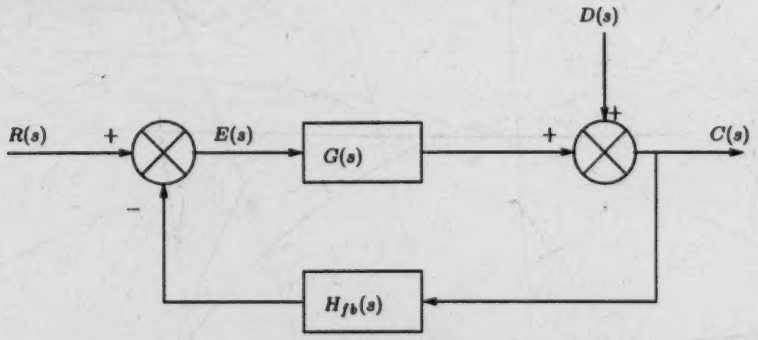

Figure 3.1: Block diagram of a feedback control system.

Usually a control system is much more complicated than the one shown in Figure 3.1. However, there are several rules that help to simplify the system to what is called a unity feedback control system. In the unity feedback control system, $H_{fb}(s) = 1$.

A control system can be represented by a mathematical description of the system also known as a dynamic model [17]. Both analytical modelling and experimental modelling of a control system involve writing the equations describing the processes in the control system. Analytical modelling is a systematic application of physical laws to system components and component interconnections. Experimental modelling is the selection of mathematical equations that seem to fit experimental results. However, before any model is created one has to clearly identify the phenomena under investigation. Once a model has been created one needs to analyze it to investigate how well the model matches the desired performance. A quick, approximate solution can be obtained by using a linear representation of the model whereas a more detailed, precise solution often require numerical techniques. However, linear analysis provides a very good idea of how the system will behave and usually there is no need to invoke anything more than linear analysis. Linear analysis also provides

convenient ways of deciding on what alterations need to be done to the system so that it will have a desired response to certain inputs. The dynamic system response is generally studied within three domains: the s-plane, the frequency response, and the state space. The s-plane domain and the frequency response methods are described in the following subsections. These two methods are used in this chapter.

3.2.1.1 S-plane domain

This technique is based on the replacement of a function of a real variable by a frequency dependent representation by using the Laplace transform. The transfer function, $G_{CL}(s)$, of a continuous control system in the s-plane domain is defined as follows:

$$G_{CL}(s) = \frac{C(s)}{R(s)}, \tag{3.1}$$

where $C(s)$ is the Laplace transform of the output signal, $R(s)$ is the Laplace transform of the input signal, and $s = \sigma + j\omega$ represents the complex variable. The inverse Laplace transform of $G_{CL}(s)$ is the impulse response of the control system, $g_{CL}(t)$. The transfer function can be also represented as:

$$G_{CL}(s) = K\frac{\prod_{i=1}^{n}(s+z_i)}{\prod_{j=1}^{m}(s+p_j)}, \tag{3.2}$$

where K is the static-loop sensitivity, z_i and p_j are the system's zeros and poles respectively, and n and m are the indices on the zeros and poles.

A very useful property of the Laplace transform is known as the Final Value Theorem. It allows designers to compute a steady-state value of a stable time function, $f(t)$, provided its Laplace transform, $F(s)$, is known. Stability of the time function is important. For an unstable system, the result of the Final Value Theorem would be erroneous [17]. The theorem states

$$\lim_{t\to\infty} f(t) = \lim_{s\to 0} sF(s). \tag{3.3}$$

Following the rules of block diagram reduction, one can find that the closed-loop transfer function of the system shown in Figure 3.1 is

$$\frac{C(s)}{R(s)} = \frac{KG(s)}{1 + KG(s)H_{fb}(s)}. \tag{3.4}$$

The stability of such a system is determined by analyzing the denominator or the characteristic equation of the closed-loop transfer function:

$$1 + KG(s)H_{fb}(s) = 0. \tag{3.5}$$

The closed-loop system is stable when all roots of the characteristic equation have negative real parts.

Stable systems are classified into system types according to their steady-state errors in response to certain inputs. The Final Value Theorem is used to determine the steady state errors. For example, assume that the input signal is a step input and assume a unity feedback system. The Laplace transform of such a signal is $\frac{P}{s}$, where P is the step amplitude. The steady-state error to step input $R(s) = \frac{P}{s}$ is then

$$e_{ss} = \lim_{s \to 0} s\,(R(s) - C(s)) = \lim_{s \to 0} s \frac{R(s)}{1 + KG(s)} = \lim_{s \to 0} \frac{P}{1 + KG(s)}, \tag{3.6}$$

$$e_{ss} = \frac{P}{1 + \lim_{s \to 0} KG(s)}. \tag{3.7}$$

Therefore, the steady-state error of this system to the step input may not be zero. Systems that have a constant error to a step input are called Type 0 systems. If on the other hand a ramp is the input signal, then

$$e_{ss} = \lim_{s \to 0} s \frac{\frac{P}{s^2}}{1 + KG(s)} = \lim_{s \to 0} \frac{P}{s(1 + KG(s))} = \frac{P}{\lim_{s \to 0} sKG(s)}. \tag{3.8}$$

It is easy to see that if $KG(s)$ does not have a pole at the origin then the steady-state error will be infinite. Systems that do have a single pole at the origin and have constant steady-state error due to a ramp input are called Type 1 systems. Similarly, systems that have two poles at the origin and have a constant steady-state error due to a parabolic input are called Type 2 systems. It is important to note that Type 1 systems have zero steady-state error in response to a step input and Type 2 systems have zero steady-state error in response to step and ramp inputs.

Generally, to analyze and design a control system, a graphical method known as Root Locus is used. The Root Locus plot shows location of all open loop poles and zeros as functions of static-loop sensitivity K. If stability of the system is of interest and if the parameter under design is not expressed as the static loop sensitivity, then according to the Root Locus method of Evans the closed-loop characteristic equation can be rearranged so that the parameter under investigation appears in place of the static loop sensitivity [17]. Stability of the rearranged system insures stability of the system of interest. The Root Locus plot is commonly used in control system design and is widely discussed in the literature (for example [5], [15], [17], [42]).

3.2.1.2 Frequency response domain

If the steady-state response is the main concern, then frequency response methods are used. The frequency response is the response of the system to a sinusoidal input.

Using Euler's identity, one can express any sinusoid as

$$Z\cos(\omega t) = \frac{Z}{2}\left(e^{j\omega t} + e^{-j\omega t}\right). \tag{3.9}$$

Letting $s = j\omega$ in Equation 3.1 and applying the superposition property one obtains the system output due to the sinusoidal input as

$$c(t) = \frac{Z}{2}\left[G(j\omega)e^{j\omega t} + G(-j\omega)e^{-j\omega t}\right]. \tag{3.10}$$

$G(j\omega)$ is a complex number that can be represented in polar form as $G(j\omega) = M(\omega)e^{j\phi(\omega)}$, where $M(\omega)$ is the magnitude of $G(j\omega)$ and $\phi(\omega)$ is the phase of $G(j\omega)$. Therefore since $M(-\omega) = M(\omega)$ and $\phi(-\omega) = -\phi(\omega)$

$$c(t) = ZM(\omega)\cos\left(\omega t + \phi(\omega)\right). \tag{3.11}$$

Equation 3.11 states that for any input of frequency ω, the output of the system with the transfer function $G(s)$ will have the same frequency, amplitude scaled by M and phase shifted by ϕ.

The frequency response of the system can in general be measured very easily. The system is driven by sinusoidal inputs with known amplitudes at the frequencies of interest. The inputs are then compared with the outputs to determine the amplitude and phase changes.

The frequency response does not provide complete information about system behaviour however. Its main purpose is to determine the steady state performance of the system disregarding the transient response.

The Bode plot is a graphical tool for analysis and design of control systems in the frequency domain. It can be directly measured the same way the frequency response is measured or it can be calculated from the transfer function of the system. Some properties of the Bode plot are important to note. First of all, each pole in a transfer function of the system produces a -20 dB/dec slope on the amplitude part of the plot and changes the phase by $-90°$. Zeros have the opposite effect. The stability of a control system is determined from the Bode plot by analyzing the gain margin (GM) and the phase margin (PM). GM is the gain at the point where the phase crosses the $-180°$ line. PM is the difference between the phase at which the amplitude plot crosses the 0 dB line and $-180°$. Figure 3.2 shows an example of GM and PM. The Bode plot method and other graphical frequency domain methods such as the Nyquist plot and the Nichol's plot are discussed in more detail in most control system literature (for example [5], [15], [17], [42]).

Even though the frequency response method generally ignores the transient response, Brogan (1991) summarized four rules of thumb showing correlations between

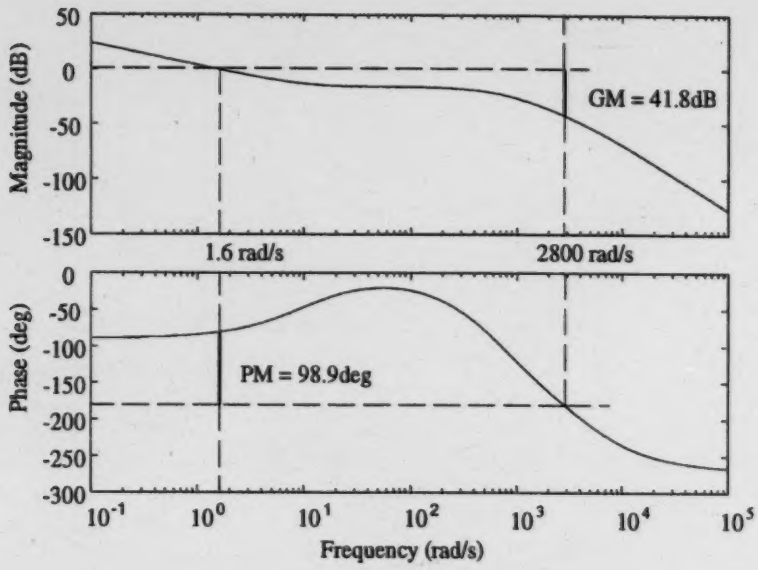

Figure 3.2: Typical Bode plot, showing gain margin of 41.8 dB and phase margin of 98.9°.

frequency domain and close-loop time domain characteristics [5]. The rules are repeated here:

1. $\zeta \approx 0.01 \times M_P$, where ζ is the damping ratio and M_P is the phase margin in degrees,
2. $\%\,overshoot + M_P \approx 75$, where *overshoot* is the maximum amount the system overshoots its final value expressed in percentage of the final value and is measured during step response,
3. $T_r \times B_{CL} = 0.9\pi$, where T_r is the rise time and B_{CL} is the closed-loop 3 dB bandwidth in rad/s,
4. Acceptable transient response requires $M_P > 30°$ and $M_G > 6$ dB, where M_G is the gain margin.

These rules are approximate however. A time delay present in a control system, for example, affects the stability and dynamic response. It may produce ringing or even instability in an otherwise well damped closed-loop system.

A time delay, T_d, is represented by an e^{-sT_d} term in the s-domain and as $e^{-j\omega T_d}$ in the frequency domain. Time delay is more easily investigated in the frequency

domain. The amplitude of the time delay term is constant and is equal to 1 and the phase varies as $-\omega T_d$.

3.2.1.3 Time domain specifications

Specifications for a control system often involve some parameters associated with the time response of the control system. Some of the most common requirements for a step response are the rise time, settling time, and overshoot. Rise time is the time needed for the system to rise from 10% to 90% of its final value. Settling time is the time it takes to reach and stay within 2% (or sometimes 5%) of the final value. Overshoot is the maximum amount of system output overshoot, beyond the steady-state output, expressed as a percentage of the steady-state output.

3.2.1.4 Phase Locked Loop

This section is based on the work published by Gardner (1979) and Best (1984) [4], [20]. A basic block diagram of a Phase Locked Loop (PLL) is shown in Figure 3.3. The PLL controls the phase of the voltage controlled oscillator (VCO) so that it

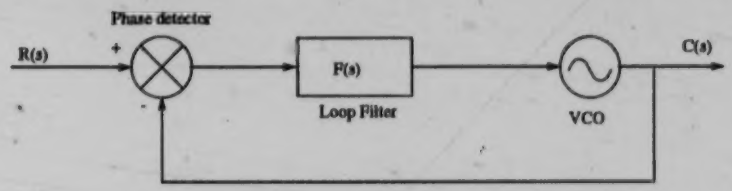

Figure 3.3: Phase Locked Loop block diagram.

follows the input phase. With the phase being the controlled variable, the transfer function of the VCO is

$$G_{VCO}(s) = \frac{K_o}{s}, \tag{3.12}$$

where K_o is the gain of the VCO in rad/s/V. The phase detector has a gain K_d expressed in V/rad. The loop filter filters out the noise and high frequency components and determines the dynamic response of the PLL. The overall transfer function of the PLL is :

$$G_{PLL}(s) = \frac{C(s)}{R(s)} = \frac{K_d F(s)\frac{K_o}{s}}{1 + K_d F(s)\frac{K_o}{s}}. \tag{3.13}$$

The transfer function of the active loop filter shown in Figure 3.4 for a second order loop is:

$$F(s) = \frac{-A(sCR_2 + 1)}{sCR_2 + 1 + (1 + A)sCR_1}. \tag{3.14}$$

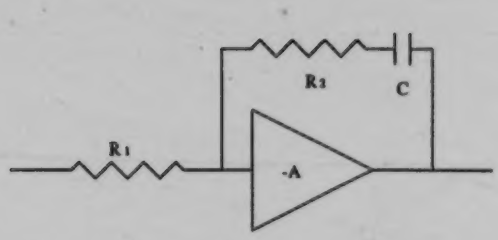

Figure 3.4: Active loop filter for a second order PLL.

For an amplifier having a large gain A and a large gain bandwidth product, the loop filter can be rewritten as follows:

$$F(s) \approx -\frac{s\tau_2 + 1}{s\tau_1}, \tag{3.15}$$

where $\tau_1 = R_1C$ and $\tau_2 = R_2C$. The PLL transfer function then becomes:

$$G_{PLL}(s) = \frac{2\zeta\omega_n s + \omega_n^2}{s^2 + 2\zeta\omega_n s + \omega_n^2}, \tag{3.16}$$

where $\omega_n = \left(\frac{K_o K_d}{\tau_1}\right)^{1/2}$ is the natural frequency of the closed loop, and $\zeta = \frac{\tau_2\omega_n}{2}$ is the damping ratio for the closed loop.

3.3 Summary of existing LO systems

3.3.1 Swarup and Yang LO system

The idea of the Swarup and Yang system as described by Thompson et al. (1986) is to measure the length of the transmission cable by measuring the phase difference between the outgoing reference signal and a part of that signal that gets reflected back at the antenna [54]. The phase of the reference signal is then adjusted accordingly to cancel out the phase error component due to increase in length of the transmission line. Since many unwanted reflections may occur in the transmission medium, the system must determine the desired component of the returning signal to effectively deliver a coherent phase signal to the antenna. This is done by modulating the desired component.

3.3.2 Cascaded PLL system

This method uses signals at slightly different frequencies travelling in opposite directions and measures phase differences between the signals as shown in Figure 3.5.

Note that $\omega \angle \varphi$ denotes a signal with a frequency of ω [rad/s], and a phase of φ [deg]. Each ω_i, [rad/s] corresponds to F_i, [Hz].

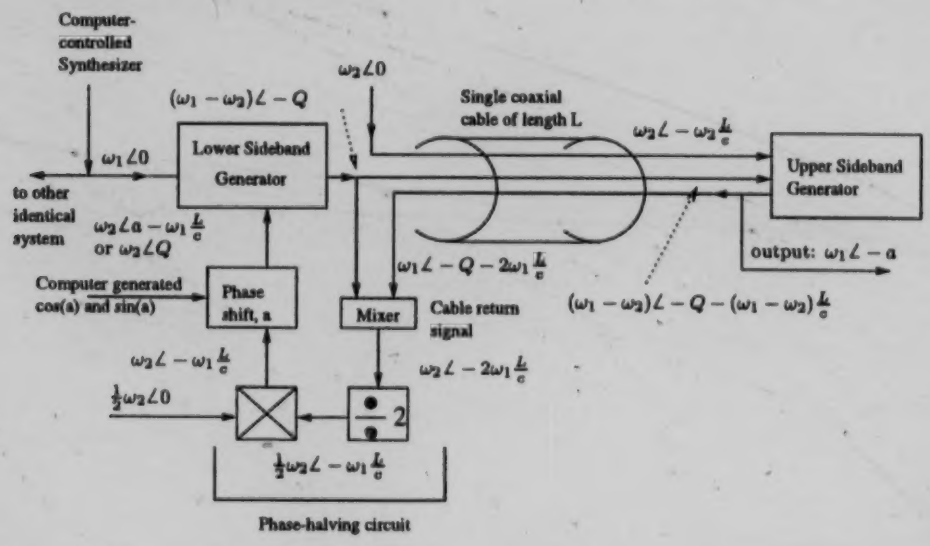
Computer-controlled Synthesizer
$\omega_2 \angle 0$
$(\omega_1 - \omega_2) \angle -Q$
Single coaxial cable of length L
$\omega_2 \angle -\omega_2 \frac{L}{c}$
$\omega_1 \angle 0$
Lower Sideband Generator
Upper Sideband Generator
to other identical system
$\omega_2 \angle a - \omega_1 \frac{L}{c}$ or $\omega_2 \angle Q$
output: $\omega_1 \angle -a$
$\omega_1 \angle -Q - 2\omega_1 \frac{L}{c}$
Computer generated cos(a) and sin(a)
Phase shift, a
Mixer
Cable return signal
$(\omega_1 - \omega_2) \angle -Q - (\omega_1 - \omega_2) \frac{L}{c}$
$\omega_2 \angle -\omega_1 \frac{L}{c}$
$\omega_2 \angle -2\omega_1 \frac{L}{c}$
$\frac{1}{2}\omega_2 \angle 0$
2
$\frac{1}{2}\omega_2 \angle -\omega_1 \frac{L}{c}$
Phase-halving circuit

Figure 3.5: Cascaded PLL system (adapted from Landecker and Vaneldik (1982) [32]).

Cascaded PLL type systems are used at the Dominion Radio Astrophysical Observatory (DRAO), the Australia Telescope, and the Mark III telescope at Jodrell Bank [32], [56], [59]. This system is also known as the Frequency-Offset, Round-Trip system. The reference signal, F_1, is combined in a PLL lower sideband generator (LSG) with a signal, F_2. The output of the LSG and reference signal, F_2, are sent to the remote end through a coaxial cable. At the remote end the two signals are mixed together in the PLL upper sideband generator (USG) to produce F_1. Some of F_1 is sent back and mixed with the output of the LSG to produce F_2, the phase of which equals to what the phase of F_1 would have been if it travelled to the remote unit and back. The phase-halving circuitry feeds half of the phase of that signal into the LSG, thus completing the loop.

3.3.3 Automatically Correcting system

This system was suggested by J. Granlund (1967) [54]. It is particularly suitable for providing a stable reference frequency at a number of points along a linear array of antennas. Two frequencies are injected from opposite ends of the transmission

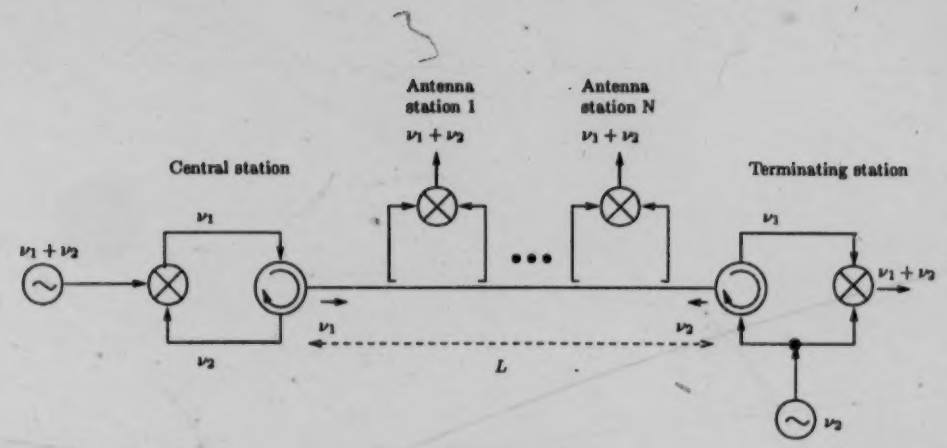

Figure 3.6: Automatically Correcting system (adapted from Thompson et al. (1986) [54]).

medium as shown in Figure 3.6. The frequency separation is very small. At each antenna the frequencies are mixed together to form a sum frequency. The effects of changes in the line length are automatically corrected.

3.3.4 Spatially Distributed PLL system

This system is described by Veidt et. al. (1985) [55]. The system consists of a

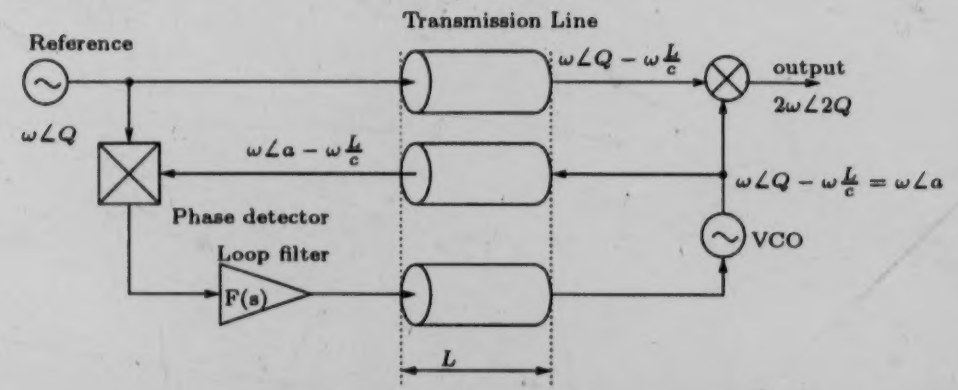

Figure 3.7: Spatially distributed PLL system (adapted from Veidt et al. (1985) [55]). The three transmission lines shown represent a single physical cable.

spatially distributed PLL with the voltage controlled oscillator (VCO) located at

the antenna feed and the loop filter located at the control centre of the telescope as shown in Figure 3.7. The error voltage is transmitted to the feed. The innovative idea behind this system is that it can provide a phase offset in the LO signal equal to the phase experienced by the IF signal on its way from the antenna feed to the control building by offsetting the frequency of the VCO at the antenna by the IF signal. The IF signal is the result of mixing the signal received by the telescope with the output of the LO system.

3.3.5 Discussion

The Swarup and Yang technique is essentially a means of measuring the phase of the reference signal at the antenna. This system has a major drawback–that is, multipath effects can greatly reduce the accuracy of the system. The Cascaded PLL system is an improvement of the Swarup and Yang LO system since it creates a frequency-shifted return signal. The automatically correcting system is not useful to provide a stable phase to just a single antenna feed; therefore, this system will not be considered.

It seems that the Spatially Distributed system and the Cascaded PLL system could provide the coherent signal to the feed of the LAR.

3.4 Comparison of the Cascaded PLL and Spatially Distributed systems

3.4.1 Comparison of steady-state errors due to distance changes

3.4.1.1 Spatially Distributed PLL system

Let us consider the following phase control transfer function, $T_{cl}(s)$, of the system shown in Figure 3.8

$$T_{cl}(s) = \frac{C(s)}{R(s)} = \frac{K\frac{F(s)}{s}e^{-sT_d}}{1 + K\frac{F(s)}{s}e^{-2sT_d}} + e^{-sT_d}, \tag{3.17}$$

where $KF(s) = K_d K_0 K_{LF}\frac{s+1/\tau_1}{s}$ in which K_d is the gain of the phase detector, K_0 is the gain of the VCO having transfer function of $\frac{K_0}{s}$, K_{LF}/τ_1 is the gain of the loop filter described by $F(s) = K_{LF}\frac{s+1/\tau_1}{s}$. For simplicity $K = K_d K_0 K_{LF}$ and $F(s) = \frac{s+1/\tau_1}{s}$. The transfer function $T_{cl}(s)$ is the transfer function of the LO system; however, the response of the LO system to the distance variations will be discussed

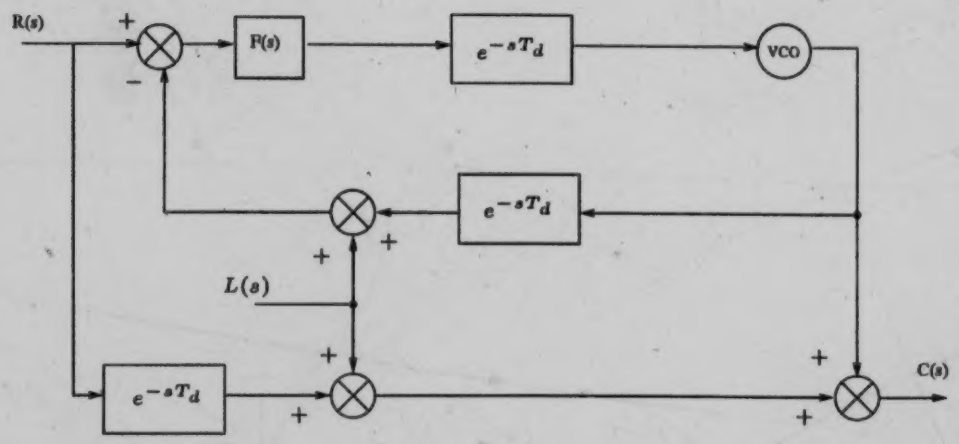

Figure 3.8: Phase-domain block diagram of the Spatially Distributed system. $R(s)$ is the input to the LO sytem, $L(s)$ represents a change in the path length, and $C(s)$ is the output of the LO system.

here so the transfer function $D_{cl}(s) = \frac{C(s)}{L(s)}$ is of interest:

$$D_{cl}(s) = \frac{C(s)}{L(s)} = -\frac{K\frac{F(s)}{s}e^{-sT_d}}{1 + K\frac{F(s)}{s}e^{-2sT_d}} + 1, \tag{3.18}$$

where $L(s)$ represents a change is the path length.

Let us assume that a step input is applied to the system described by D_{cl}. In the s-domain the input is expressed as $\frac{C_1}{s}$, where C_1 is the amplitude of the input. According to the Final Value Theorem the error in the output of the system will then be

$$e_{ss} = \lim_{s \to 0} s\frac{C_1}{s}E(s) \tag{3.19}$$

where in this case $E(s) = D_{cl}(s)$ and thus

$$e_{ss} = \lim_{s \to 0} C_1 \left(-\frac{K\frac{F(s)}{s}e^{-sT_d}}{1 + K\frac{F(s)}{s}e^{-2sT_d}} + 1 \right) = 0. \tag{3.20}$$

Similarly, if a ramp input is applied to the system described by $D_{cl}(s)$, the steady-state error due to this input, described in the s-domain as $\frac{C_1}{s^2}$, would then be

$$e_{ss} = \lim_{s\to 0} s\frac{C_1}{s^2}\left(-\frac{K\frac{F(s)}{s}e^{-sT_d}}{1+K\frac{F(s)}{s}e^{-2sT_d}}+1\right), \tag{3.21}$$

$$e_{ss} = \lim_{s\to 0} C_1\left(-\frac{KF(s)e^{-sT_d}}{s+KF(s)e^{-2sT_d}}+\frac{1}{s}\right), \tag{3.22}$$

$$e_{ss} = \lim_{s\to 0} C_1\left(\frac{-KF(s)e^{-sT_d}+s+KF(s)e^{-2sT_d}}{s^2+sKF(s)e^{-2sT_d}}\right). \tag{3.23}$$

Substituting $F(s) = \frac{s+b}{s}$, where $b = \frac{1}{\tau_1}$, in Equation 3.23, one obtains

$$e_{ss} = \lim_{s\to 0} C_1\left(\frac{-K(s+b)e^{-sT_d}+s^2+K(s+b)e^{-2sT_d}}{s^3+sK(s+b)e^{-2sT_d}}\right) \tag{3.24}$$

Since both numerator and denominator approach zero as $s \to 0$, L'Hôpital's rule may be used to determine e_{ss}. According to the rule

$$e_{ss} = C_1\frac{\lim_{s\to 0} num'(s)}{\lim_{s\to 0} den'(s)}, \tag{3.25}$$

where

$$\begin{aligned} num'(s) &= 2s + K\left(e^{-2sT_d} - e^{-sT_d}\right) \\ &+K(s+b)\left(-2T_de^{-2sT_d} + T_de^{-sT_d}\right) \end{aligned} \tag{3.26}$$

and

$$den'(s) = 3s^2 + K(2s+b)e^{-2sT_d} - 2KT_d(s^2+bs)e^{-2sT_d}. \tag{3.27}$$

Thus

$$e_{ss} = C_1\frac{-T_dKb}{Kb} = -T_dC_1. \tag{3.28}$$

A parabolic input applied to the system is described by $\frac{C_1}{s^3}$ in the s-domain. The steady-state error is

$$e_{ss} = \lim_{s\to 0} s\frac{C_1}{s^3}\left(-\frac{K\frac{F(s)}{s}e^{-sT_d}}{1+K\frac{F(s)}{s}e^{-2sT_d}}+1\right) \tag{3.29}$$

or

$$e_{ss} = C_1\lim_{s\to 0}\left(\frac{-K(s+b)e^{-sT_d}+s^2+K(s+b)e^{-2sT_d}}{s^4+K(s^3+bs^2)e^{-2sT_d}}\right). \tag{3.30}$$

Once again both numerator and denominator approach zero and L'Hôpital's rule is

applied to determine e_{ss}.

$$\begin{aligned} num'(s) &= 2s + K\left(e^{-2sT_d} - e^{-sT_d}\right) \\ &+K(s+b)\left(-2T_de^{-2sT_d} + T_de^{-sT_d}\right) \end{aligned} \tag{3.31}$$

and

$$den'(s) = 4s^3 + K(3s^2 + 2bs)e^{-2sT_d} - 2KT_d(s^3 + bs^2)e^{-2sT_d}, \tag{3.32}$$

where

$$\lim_{s\to 0} num'(s) = T_dKb \tag{3.33}$$

and

$$\lim_{s\to 0} den'(s) = 0, \tag{3.34}$$

therefore

$$e_{ss} \to \infty. \tag{3.35}$$

3.4.1.2 Cascaded PLL system

This system is described by Landecker and Vaneldik, (1982)[32]. The transfer function of the system is

$$G_{cl}(s) = \frac{C(s)}{R(s)} = \frac{-G_1(s)G_2(s)e^{-sT_d}}{1 + G_1(s)(e^{-2sT_d}G_2(s) - 1)H(s)}, \tag{3.36}$$

where DC gains $G_1(0) = 1$, $G_2(0) = 1$ and $H(0) = \frac{1}{2}$. The block diagram of the phase control system is shown in Figure 3.9. G_1 and G_2 represent the LSG and the USG respectively. $H(s)$ represents the transfer function of a phase-halving PLL. The phase-halving system is based on a PLL and is shown in Figure 3.10.

The transfer function relating the variations in the distance between the ground unit and the remote unit to the output of the LO system is expressed as

$$D_{cl}(s) = \frac{C(s)}{L(s)} = \left(1 - \frac{G_1(s)H(s)}{1 - G_1(s)H(s)}e^{-sT_d}\right)\frac{G_2(s)}{1 + \frac{G_1(s)H(s)}{1-G_1(s)H(s)}G_2(s)e^{-2sT_d}}, \tag{3.37}$$

where $L(s)$ represents a change in the path length.

The steady-state error of this system to a step input, $\frac{C_1}{s}$, is

$$e_{ss} = \lim_{s\to 0} s\frac{C_1}{s}E(s) = \lim_{s\to 0}\frac{C_1}{s}s\left(\frac{\left(1 - \frac{G_1(s)H(s)}{1-G_1(s)H(s)}e^{-sT_d}\right)G_2(s)}{1 + \frac{G_1(s)H(s)}{1-G_1(s)H(s)}G_2(s)e^{-2sT_d}}\right), \tag{3.38}$$

where $E(s) = D_{cl}(s)$.

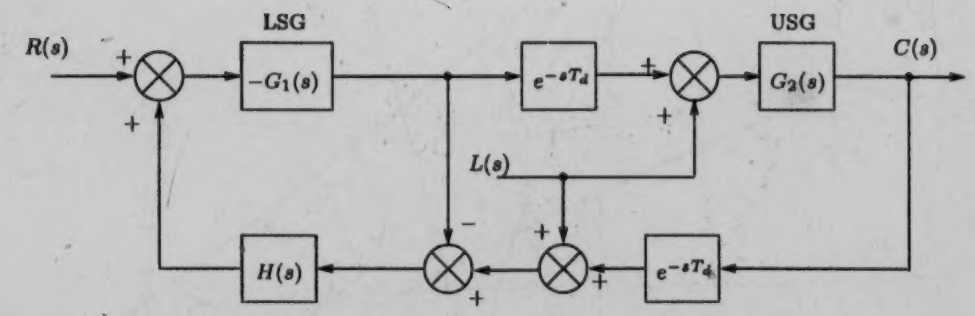

Figure 3.9: Phase-domain block diagram of the phase control Cascaded PLL system. $R(s)$ is the input to the LO sytem, $L(s)$ represents a change in the path length, and $C(s)$ is the output of the LO system.

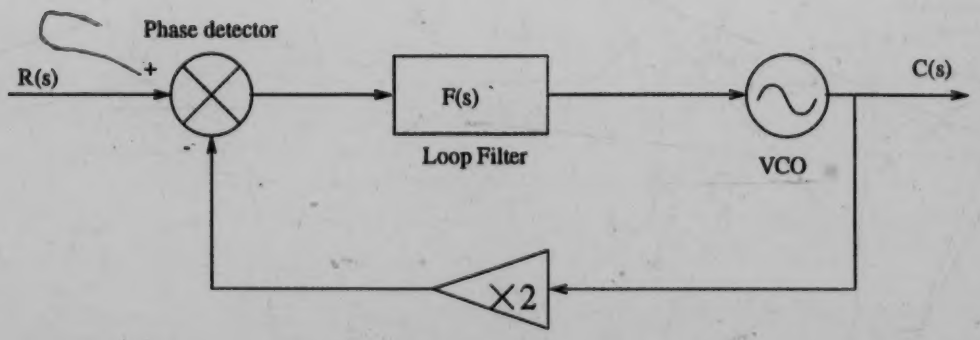

Figure 3.10: Phase-domain block diagram of a PLL based phase-halving system.

Ideally each of the LSG and USG are constructed out of a mixer and a passband filter and therefore it can be assumed that $G_1 = G_2 = 1$. Since $H(0) = \frac{1}{2}$, then

$$e_{ss} = 0. \tag{3.39}$$

If a ramp, represented by $\frac{C_1}{s^2}$ in the s-domain, is applied at the input to the system, the steady state error can be found as follows:

$$e_{ss} = \lim_{s\to 0} s\frac{C_1}{s^2}\left(\frac{\left(1 - \frac{G_1(s)H(s)}{1-G_1(s)H(s)}e^{-sT_d}\right)G_2(s)}{1 + \frac{G_1(s)H(s)}{1-G_1(s)H(s)}G_2(s)e^{-2sT_d}}\right). \tag{3.40}$$

The actual transfer function of $H(s) = \frac{KF(s)}{s+2KF(s)}$ where again $F(s) = \frac{s+b}{s}$ and $K = K_{LF}K_dK_0$. The steady-state error of the LO system due to a ramp input is

$$e_{ss} = \lim_{s\to 0} C_1\left(\frac{1 - \frac{H(s)}{1-H(s)}e^{-sT_d}}{s + s\frac{H(s)}{1-H(s)}e^{-2sT_d}}\right), \tag{3.41}$$

$$e_{ss} = \lim_{s\to 0} C_1\left(\frac{1 - H(s)(1 + e^{-sT_d})}{s + sH(s)(e^{-2sT_d} - 1)}\right), \tag{3.42}$$

$$e_{ss} = \lim_{s\to 0} C_1\left(\frac{s^2 + 2Ks + 2Kb - K\,(s+b)\left(e^{-2sT_d} + 1\right)}{s^3 + 2Ks^2 + 2Kbs + K\,(s^2 + bs)\,(e^{-2sT_d} - 1)}\right). \tag{3.43}$$

Equation 3.43 has both numerator and denominator approaching zero as $s \to 0$ L'Hôpital's rule can be used to solve for e_{ss}:

$$e_{ss} = C_1\frac{\lim_{s\to 0} num'(s)}{\lim_{s\to 0} den'(s)}, \tag{3.44}$$

where

$$num'(s) = 2s + K(1 - e^{-2sT_d}) + 2T_dKse^{-2sT_d} + 2T_dKbe^{-2sT_d} \tag{3.45}$$

and

$$\begin{aligned} den'(s) = {} & 3s^2 + 2Ks(1 + e^{-2sT_d}) - 2T_dKs^2e^{-2sT_d} \\ & + Kb(1 + e^{-2sT_d}) - 2T_dKbse^{-2sT_d}. \end{aligned} \tag{3.46}$$

It is easy to see that $\lim_{s\to 0} num'(s) = T_dKb$ and $\lim_{s\to 0} den'(s) = 2Kb$, therefore

$$e_{ss} = C_1\frac{T_d}{2}. \tag{3.47}$$

The steady-state error due to a parabolic input, $\frac{C_1}{s^3}$, is

$$e_{ss} = \lim_{s\to 0} s\frac{C_1}{s^3}\left(\frac{\left(1-\frac{G_1(s)H(s)}{1-G_1(s)H(s)}e^{-sT_d}\right)G_2(s)}{1+\frac{G_1(s)H(s)}{1-G_1(s)H(s)}G_2(s)e^{-2sT_d}}\right). \tag{3.48}$$

Substituting the transfer function of the phase-halving PLL and simplifying the equation for e_{ss}, one derives

$$e_{ss} = \lim_{s\to 0} C_1\left(\frac{s^2+2Ks+2Kb-K\left(s+b\right)\left(e^{-2sT_d}+1\right)}{s^4+2Ks^3+2Kbs^2+K\left(s^3+bs^2\right)\left(e^{-2sT_d}-1\right)}\right). \tag{3.49}$$

Again L'Hôpital's rule is used to solve Equation 3.49:

$$e_{ss} = C_1\frac{\lim_{s\to 0} num'(s)}{\lim_{s\to 0} den'(s)}, \tag{3.50}$$

$$num'(s) = 2s + K(1-e^{-2sT_d}) + 2T_dKse^{-2sT_d} + 2T_dKbe^{-2sT_d} \tag{3.51}$$

and

$$\begin{aligned} den'(s) = {} & 4s^3 + 3Ks^2(1+e^{-2sT_d}) - 2T_dKs^3e^{-2sT_d} \\ & +2Kbs(1+e^{-2sT_d}) - 2T_dKbs^2e^{-2sT_d}. \end{aligned} \tag{3.52}$$

It is easy to see that both $num'(s)|_{s\to 0} \to T_dKb$ and $den'(s)|_{s\to 0} \to 0$; therefore the complete steady-state error of the system to the parabolic input is

$$e_{ss} \to \infty. \tag{3.53}$$

3.4.2 Stability in the presence of time delay

Let us consider the stability of the transfer function described by Equation 3.36. In the frequency domain, the term

$$\left(e^{-2j\omega T_d}G_2(\omega) - 1\right) \tag{3.54}$$

is time delay dependent. Since the magnitude of $e^{-2j\omega Td}$ is always one and $|G_2| \leq 1$, $\left|e^{-2j\omega T_d}G_2 - 1\right| \leq 2$ for all ω and for all T_d. Therefore, $\left|G_1(e^{-2j\omega T_d}G_2 - 1)H\right| \leq 1$, since $|G_1| \leq 1$ and $|H| \leq \frac{1}{2}$ for all ω. Even though the time delay cannot make the system unstable, it will worsen the transient response of the system as it increases [32].

The Spatially Distributed system on the other hand is very sensitive to the time delay since the time delay term affects the phase of the open loop transfer function. As the time delay increases, the phase of the open loop system decreases rapidly

with frequency, thus worsening the GM, PM, and the dynamic response until the system becomes closed-loop unstable.

3.4.3 Distance Measurement

An important requirement for an LO system to be used in the SKA is the ability to measure the transmission distance between the feed and the surface of the LAR. The Cascaded PLL system operates by measuring the distance between the telescope control centre and the antennas. The Spatially Distributed system on the other hand does not measure the distance by itself without modifications.

There are two ways of measuring the phase shift with the Spatially Distributed system, however. One way would be to measure the phase difference between the reference signal arriving from the ground unit and the LO output signal at the airborne platform. This would require additional circuitry to modulate a carrier with the output of a phase detector and send the result of the measurements back to the ground. The other way is to send the output of the LO signal to the ground and determine the phase shift acquired while travelling. This could be achieved by frequency shifting the carrier by the LO output frequency, which might be done in any case to distinguish between the uplink and the downlink.

3.5 Conclusions

Both the Cascaded PLL system and the Spatially Distributed system can be designed to have the same dynamic response and are employed in existing aperture synthesis telescopes. They both have similar steady-state errors for similar inputs as discussed in Section 3.4.1. The three inputs that were used to determine the steady-state performance of the system will be present in the actual system. These signals will appear in the real system because the LO signals experience Doppler shift due to motion of the airborne platform. For example a constant speed of the platform will produce a ramp signal in the phase domain. The Cascaded PLL system is more stable in the presence of time delay as discussed in Section 3.4.2. Also the distance measurement between the remote and ground units is a by-product of the Cascaded PLL system, whereas the Spatially Distributed system must be reconfigured to provide the distance measurement capability. But perhaps the most important reason for choosing the Cascaded PLL system over the Spatially Distributed system is the extra two zeros at the origin that exist in the transfer function described by Equation 3.37. Equation 3.37 can be rewritten as

$$D_{cl}(s) = \frac{C(s)}{L(s)} = \frac{\left(1 - G_1(s)H(s) - G_1(s)H(s)e^{-sT_d}\right)G_2(s)}{1 + G_1(s)H(s)\left(G_2(s)e^{-2sT_d} - 1\right)}, \qquad (3.55)$$

in which the zeros appear from the bracketed terms in the numerator and the denominator. The similar transfer function for the Spatially Distributed system shown in Equation 3.18 has only one zero at the origin. The extra zero dramatically improves the ability of the Cascaded PLL system to attenuate slow distance changes between the ground unit and the remote unit. The extra zero makes the Cascaded PLL system a superior system for the SKA.

Chapter 4

The Focal Length/LO system

4.1 Introduction

The chapter discusses a functional design of the FLLOSS. The chapter begins with a suggestion for a possible configuration of the FLLOSS system. There are three block diagrams to aid understanding of the system followed by two more detailed diagrams explaining the fine details.

The sections that follow show how the frequencies for the FLLOSS were selected and how the usage of the Chinese remainder theorem (CRT) assists the distance measurement and in particular the problem of ambiguity resolution.

The distance measurement system has been suggested in Chapter 2. The LO system has been selected in Chapter 3. The detailed design of an LO system prototype will be discussed in the next chapter.

4.2 Background: Chinese remainder theorem

The CRT is often discussed in connection with radars. The theorem is well known and is discussed in many books on number theory. As quoted by Niven and Zuckerman (1966) the theorem states [40]:

> "Let m_1, m_2, ..., m_s denote s positive integers that are relatively prime in pairs, and let β_1, β_2, ..., β_s denote any s integers. Then the congruences $x \equiv (\beta_i) mod(m_i)$, $i = 1, 2, \ldots, s$ have common solutions. Any two solutions are congruent modulo m_1, m_2, ..., m_s."

The theorem will not be proven here. However an example of its usage in radars will explain how the theorem is relevant to the discussions of ambiguity resolution that follow.

Assume that two radars transmit pulses of 1 μs duration repetitively, but with different repetition rates. The reflections of the pulses are received by corresponding receivers. Receiver #1 has eight gates occupying 8 μs. Receiver #2 has ten gates occupying 10 μs. The returned signal is detected in the second gate of Receiver #1 and in the first gate of Receiver #2. The actual distance will be found with the use of the CRT.

The transmission repeats every 9μs in the first radar and every 11μs in the second radar. Therefore $m_1 = 9$ and $m_2 = 11$, where 1 μs is one unit of measurement and remainders $\beta_1 = 2$ and $\beta_2 = 1$. Numbers nine and eleven are relatively prime; thus, the CRT can be applied.

According to the CRT, the true distance between the radars and the target is

$$\begin{aligned} L &\equiv (2) mod(9) \\ L &\equiv (1) mod(11). \end{aligned} \tag{4.1}$$

The proof of the theorem presented by Clarke (1984) shows that the solution to this example is

$$L = \sum_{j=1}^{j=s} \frac{m}{m_j} b_j \beta_j, \tag{4.2}$$

where $m = \prod_{i=1}^{i=s} m_i$ and b_j is found from $\frac{m}{m_j} b_j \equiv (1) mod(m_j)$ for $1 \leq j \leq s$ [9]. Thus b_1 and b_2 are calculated so that

$$\begin{aligned} 11 b_1 &\equiv (1) mod(9) \\ 9 b_2 &\equiv (1) mod(11). \end{aligned} \tag{4.3}$$

By inspection, $b_1 = 5$ and $b_2 = 5$. Then the distance is

$$L = 11 b_1 \times 2 + 9 b_2 \times 1 = 155. \tag{4.4}$$

Other solutions can be found from

$$L \equiv (155) mod(9 \times 11). \tag{4.5}$$

Therefore the distance is $(56 + 99k)$ $\mu s \times c$, $k = 0, 1, \ldots$, where c is the speed of light. The distance ambiguity in this example is (9×11) $\mu s = 99$ μs.

4.3 Combining the LO and FLM systems

The proposed range of frequencies of observation for the LAR telescope is 300 MHz–22 GHz and the upper frequency may be as high as 30 GHz. As explained in Chapter

1, the LO system and the FLM system will be operating over a radio link. It is very important, therefore, to make sure that these two systems do not interfere with the LAR telescope.

Figure 4.1 shows the Cascaded PLL LO System of Figure 3.5 redrawn to incorporate a free-space path. It is important that the FLLOSS should not interfere with the operation of the LAR telescope. Therefore all radiated signals must lie above the upper limit of the operating frequency. Figure 4.2 shows the same system with the addition of upconverters. Note that in this chapter F implies the frequency of the signal, while f implies the frequency and the phase; thus $f = F\angle\phi$.

The "Downconverter" block in the LO ground unit mixes together two frequencies arriving from the LO remote unit to produce a low frequency signal for the LO. A more detailed block diagram of the system follows in Figures 4.4 and 4.5.

The LO system consists of a number of CW signals that travel the focal length and might be used for the distance measurement. As discussed in Section 2.6, the FLM system might also require a PRN sequence for ambiguity resolution. Figure 4.3 shows the combination of the LO system and the PRN signal, where the frequency carrier f_{pc} is modulated with the PRN signal and upconverted with f_p to be outside the LAR band.

The complete system is depicted in Figures 4.4 and 4.5. Upconversion and downconversion are represented by mixers. Figure 4.4 also shows the CW signals that are available for distance measurement. It is assumed that every reference signal in Figure 4.4 is locked to a common phase- and frequency-stable reference signal.

The frequency relations and descriptions of the signals shown in Figures 4.4 and 4.5 are as follows:

1. F_p - high frequency carrier for PRN signal,
2. F_c - high frequency carrier for the LO system,
3. F_0 - reference signal delivered by the LO system,
4. F_{PRN} - frequency of the PRN code (chirp frequency),
5. F_{ref} - reference signal required by the LO system,
6. $F_{ref/2}$ - half of F_{ref},
7. F_{pc} - frequency carrier modulated by the PRN code,
8. $F' = F_p - F_{pc}$,
9. $F_a = F_0 - F_{ref}$,
10. $F_1 = F_c + F_a$,

Figure 4.1: Block diagram of the LO system.

Figure 4.2: LO system upconverted to higher frequencies.

Figure 4.3: LO system with the PRN signal.

Figure 4.4: Complete FLLOSS: ground unit.

Figure 4.5: Complete FLLOSS: remote unit.

11. $F_2 = F_c + F_{ref}$,
12. $F_3 = F_c - F_0$,
13. $F_4 = F_3 - F_0$,
14. $F_5 = F_p + F_0$,
15. $F'' = F' + F_0$.

Figure 4.6 shows the spectrum of the uplink and downlink signals.

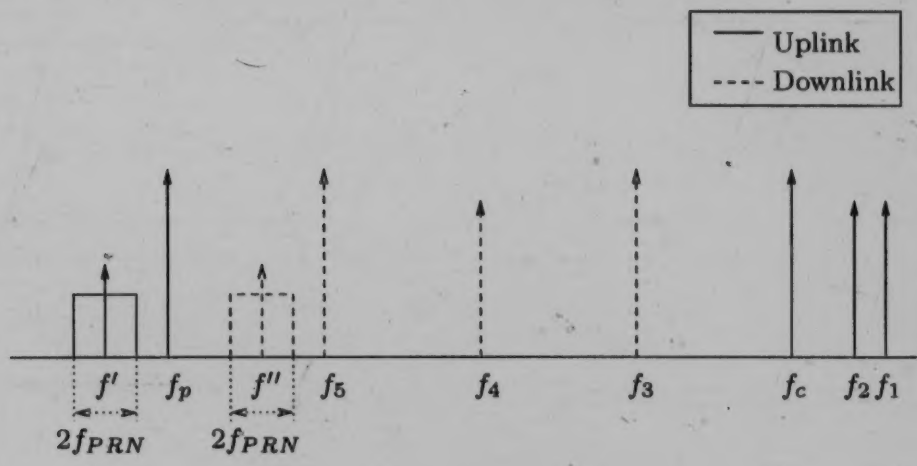

Figure 4.6: Uplink and Downlink Spectra.

The signals available for distance measurement are:

1. $f_3 = F_3\angle(A - 2L_3 + \Delta\phi_3 - \phi_{LO})$
2. $f_4 = F_4\angle(2A - 2L_4 + \Delta\phi_4 - 2\phi_{LO})$
3. $f_5 = F_5\angle(-A - 2L_5 + \Delta\phi_5 + \phi_{LO})$

where

1. $\Delta\phi_3$, $\Delta\phi_4$, $\Delta\phi_5$ are the uncalibrated phase errors in the f_3, f_4 and f_5 signals.
2. L_3, L_4, L_5 are the phases due to one way travel by the f_3, f_4 and f_5 signals.

3. A is the output phase of the LSG. In theory $A = Q - L_0$; Q may be changing depending on the location of the radio source on the sky, and L_0 is the phase due to one-way travel of the F_0 signal.

4. ϕ_{LO} is the phase error in the LO output.

There are two other lower frequency signals available:

1. $f_{ref} = F_{ref}\angle(A + \Delta\phi_{ref})$

2. $f_a = F_a\angle(-A + \Delta\phi_a)$,

where $\Delta\phi_{ref}$ and $\Delta\phi_a$ are the uncalibrated phase errors in the f_{ref} and f_a signals.

One can use different linear combinations of the signals to measure the distance with different frequencies and thus different ambiguities. According to the specification, ϕ_{LO} should not vary by more than ($5° F_0/22$ GHz) rms but its actual value is not known, introducing variable errors in the distance measurements. The value of A may not be a constant. Therefore, one should remove ϕ_{LO} and A from signal phases by means of linear combinations if possible.

The following are some linear combinations that can be used to measure the distance at high frequencies for more accurate results:

1. $f_6 = f_3 + f_5 = F_6\angle(-2L_6 + \Delta\phi_6)$

2. $f_7 = f_4 + 2f_5 = F_7\angle(-2L_7 + \Delta\phi_7)$

3. $f_8 = 2f_3 - f_4 = F_8\angle(-2L_8 + \Delta\phi_8)$,

where $\Delta\phi_6$, $\Delta\phi_7$, and $\Delta\phi_8$ are the uncalibrated phase errors in the f_6, f_7 and f_8 signals.

From the definitions of these frequencies one can derive that $F_8 < F_6 < F_7$. Therefore measurement of the phase of the f_7 signal gives the highest accuracy provided the phase errors are calibrated out. The lower frequency signals must also be measured to resolve the ambiguities that are unavoidable when measuring a distance with CW signals:

1. $f_9 = f_3 - f_4 - f_a = F_9\angle(-2L_0 + \Delta\phi_9 + \phi_{LO})$,

2. $f_{10} = f_4 - f_5 + f_a = F_{10}\angle(-2L_0 + \Delta\phi_{10} + 3\phi_{LO})$,

where $\Delta\phi_9$ and $\Delta\phi_{10}$ are the uncalibrated phase errors in the f_9 and f_{10} signals.

The low frequency signals are contaminated by the LO phase error; therefore these measurements cannot be very accurate.

If an ideal PSK modulator is available, the f_p signal may be PSK modulated by the PRN signal. If that is the case, the phase of the f_7 signal would not be affected by the phase errors due to the PRN since the PSK modulation is effectively removed by squaring the modulated signal; however, in reality the phase at the output of a modulator may be unbalanced by, say, 0.5° which introduces phase errors that will cause errors in distance measurement. Therefore, a subcarrier f' is introduced to be modulated by the PRN signal. It may be possible to improve PSK modulators so that the phase errors are reduced. In this case, the need for the f' signal disappears; however, the phase of the f_6 signal will be contaminated by a 180° ambiguity due to PSK modulation. The following discussion on distance measurement will show that it is not necessary to measure the phase of the f_6 signal to obtain accurate distance measurement.

The phase of the f_{10} signal is more contaminated than the phase of the f_9 signal but the frequency difference is not significant. Therefore, measurement of the phase of the f_{10} signal is not suggested.

4.4 Selection of the frequencies of operation

There are several issues to be addressed when it comes to selecting the frequencies for the FLLOSS. The most important issues are summarized as follows:

1. The highest operating frequency of the LAR telescope might be as much as 30 GHz. It is imperative that the frequencies of operation of the FLLOSS be higher than the highest frequency of observation.

2. It is also desirable to have all signals within the same frequency band since it is more difficult to find components spanning more than one standard band. The two standard bands that will be considered are shown in Table 4.1.

Ka band	26.5 GHz – 40 GHz
Q band	33 GHz – 50.5 GHz

Table 4.1: Frequency bands considered for the FLLOSS.

3. Frequencies between 45 GHz and 75 GHz are in the oxygen resonance-region [49]. It is therefore desired to have the FLLOSS frequencies below 45 GHz.

4. Low frequencies are preferred since the free air attenuation increases with frequency.

5. It is also important to select the frequencies so that the FLLOSS does not interfere with other band users. There are a large number of protected bands that the FLLOSS may not be allowed to occupy [28].

6. It should be possible to separate each of the signals in the systems using filters, otherwise unwanted spurious signals may decrease the accuracy of the system. As a rule a narrow bandpass filter will have a relative bandwidth of 1%. Therefore it is desirable to have $100(F_1 - F_2) = 100(F_0 - 2F_{ref}) \approx F_c$ and 30 GHz $< F_c <$ 45 GHz.

7. It is also desirable for F_0 to be of high frequency, since when the output of the LO is multiplied to 22 GHz or 30 GHz at the telescope focus, the phase errors are multiplied also.

8. It is advantageous to set the frequencies so that combined together the lower frequency signals will resolve the ambiguity of the distance measurement by the higher frequency signals.

Now the signal frequencies that are available for distance measurement again are:

1. $F_7 = F_c - F_0 + 2F_p$
2. $F_8 = F_c$.
3. Even though nominally $F_9 = F_{ref}$, the phase of f_9 is due to a signal of frequency F_0; therefore for distance measurement purposes $F_9 = F_0$.

The following frequencies are suggested for the FLLOSS. The frequencies were selected so that there would be no spurious signals due to harmonics present in signal bands:

1. $F_p = 38.2785$ GHz,
2. $F_c = 41.1700$ GHz,
3. $F_0 = 0.6570$ GHz,
4. $F_{ref} = 0.2730$ GHz,
5. $F_{pc} = 0.3000$ GHz.

Frequency	Services
37.5 GHz – 39.5 GHz	Fixed Fixed-satellite (space-to-Earth) Mobile
39.5 GHz – 40.5 GHz	Fixed Fixed-satellite (space-to-Earth) Mobile Mobile-satellite (space-to-Earth)
40.5 GHz – 42.5 GHz	Broadcasting-satellite Fixed Mobile

Table 4.2: Radio frequency bands [28].

The frequencies F_p, F_c, and F_0 were chosen so that wavelengths λ_7, λ_8, and λ_0 of F_7, F_8, and F_0 were within 10% from being integer multiples of distance measurement accuracies r_7, r_8, and r_0 discussed in Section 4.5, assuming that the speed of light $c = 299695100$ m/s.

Table 4.2 shows the frequency band allocations relevant to the frequencies selected for the FLLOSS.

The simulated frequencies used for distance measurement are then $F_7 = 117.07$ GHz, $F_8 = 41.17$ GHz and $F_0 = 0.657$ GHz. The wavelengths of the frequencies are $\lambda_7 = 2.56$ mm, $\lambda_8 = 7.28$ mm and $\lambda_0 = 456$ mm.

4.5 Procedure for distance measurement

The CRT provides a convenient way of determining a true range from several ambiguous distance measurements [2], [9], [49]. In the case of the FLM system the ambiguous measurements are wavelength measurements, not time delay measurements as in radars where the CRT is widely used.

Assume that the accuracies of measurement of the wavelengths of f_7, f_8 and f_0 are $r_7 = 20\,\mu$m, $r_8 = 40\,\mu$m and $r_0 = 3$ mm respectively. Note that the phase error ϕ_{LO} will introduce an error of $(5° F_0/22$ GHz) rms $= 0.15°$ rms in f_0 which is equivalent to 0.2 mm. Obviously, since the measurements will be halved to measure the one way distance and with the accuracy as mentioned, the three inputs to the distance determining system based on the CRT are $m_7 = 65$, $m_8 = 92$ and $m_0 = 77$. These three are relatively prime and the necessary condition of the theorem is fulfilled. Note that the round-off errors in λ_7, λ_8, and λ_0 of 35 nm, 547 nm, and 157 μm respectively introduce errors in the distance measurement; however, these errors are

very insignificant and constitute 0.0014%, 0.0075%, and 0.034% of the corresponding wavelength.

Let us assume that the measurement of the distance L produces the following results:

1. distance measured with f_7 in units of r_7 is $\beta_7 = \beta_7^0 + \Delta\beta_7$
2. distance measured with f_8 in units of r_8 is $\beta_8 = \beta_8^0 + \Delta\beta_8$
3. distance measured with f_9 in units of r_0 is $\beta_0 = \beta_0^0 + \Delta\beta_0$,

where $\Delta\beta_i$ are errors in the measurements and are integers in units of r_i.

There are four independent ways of measuring the actual distance L by applying the CRT, as follows:

$$\begin{cases} L - E_0 = L_0 \equiv (C_7^0\beta_7 + C_8^0\beta_8 + C_0^0\beta_0) mod(m_7m_8m_0) \\ L - E_1 = L_1 \equiv (C_7^1\beta_7 + C_8^1\beta_8 \qquad\quad) mod(m_7m_8) \\ L - E_2 = L_2 \equiv (C_7^2\beta_7 + \qquad\quad C_0^2\beta_0) mod(m_7m_0) \\ L - E_3 = L_3 \equiv (\qquad\quad C_8^3\beta_8 + C_0^3\beta_0) mod(m_0m_8) \end{cases} \tag{4.6}$$

where E_i is the error in the distance measurement, L_0, L_1, L_2 and L_3 are the results produced by solving each equation in System 4.6 and C_i^j are constants required by the CRT and found by solving System 4.7.

$$\begin{cases} C_7^0 = b_7^0 m_8 m_0 \\ C_8^0 = b_8^0 m_7 m_0 \\ C_0^0 = b_0^0 m_7 m_8 \end{cases} \quad \begin{cases} C_7^1 = b_7^1 m_8 \\ C_8^1 = b_8^1 m_7 \\ C_0^1 = 0 \end{cases}$$

$$\begin{cases} C_7^2 = b_7^2 m_0 \\ C_8^2 = 0 \\ C_0^2 = b_0^2 m_7 \end{cases} \quad \begin{cases} C_7^3 = 0 \\ C_8^3 = b_8^3 m_0 \\ C_0^3 = b_0^3 m_8 \end{cases} \tag{4.7}$$

where b_7^0 is the smallest positive number that when multiplied by m_8m_0 and divided by m_7 produces one as the remainder. Similar definitions apply to all $b's$. Note that L_0, L_1, L_2, and L are in units of r_7 in the first three equations in System 4.6, and L_3 and L are in units of r_8 in the fourth equation.

When the FLM system is calibrated, the errors $\Delta\beta_i$ will be zero and the distance L can be measured directly using any equation in System 4.6.

The following are the constants required by Systems 4.6 and 4.7: $b_7^0 = 64$, $b_8^0 = 5$, $b_0^0 = 74$, $b_7^1 = 53$, $b_8^1 = 17$, $b_7^2 = 38$, $b_0^2 = 32$, $b_8^3 = 49$, $b_0^3 = 36$. Therefore, System 4.6 becomes

$$\begin{cases} L_0 \equiv (453376 \times \beta_7 + 25025 \times \beta_8 + 442520 \times \beta_0) mod(460460) \\ L_1 \equiv (\ 4876 \times \beta_7 + \ 1105 \times \beta_8 \qquad\qquad\ ) mod(5980) \\ L_2 \equiv (\ 2926 \times \beta_7 \qquad\qquad + \ 2080 \times \beta_0) mod(5005) \\ L_3 \equiv (\qquad\qquad 3773 \times \beta_8 + \ 3312 \times \beta_0) mod(7084) \end{cases} \tag{4.8}$$

System 4.8 produces an output in terms of the units of measurements that are related to the resolution of the distance measurement. The actual distance is obtained by multiplying the distance found by applying the CRT by the appropriate resolution.

If the measurements are calibrated ($\Delta\beta_0 = \Delta\beta_1 = \Delta\beta_2 = \Delta\beta_3 = 0$), the ambiguity of the distance measurement depends on the product $m_7 m_8 m_0$, which could be made much larger if the phase measurement equipment is capable of achieving higher accuracy of measurements. The ambiguity that the PRN correlator has to resolve is thus $m_7 m_8 m_0 \times r_7 = 9.2092$ m. An ambiguity of 9 m corresponds to a time delay of 30 ns. A PRN noise with a chirp frequency of $F_{PRN} = 33$ MHz and higher will give enough resolution to resolve the ambiguity without the necessity of oversampling and fitting a function to the output of the correlator as discussed in Section 2.2.2.3. A TMC2023 digital correlator produced by Fairchild would be a perfect choice for the correlator. The device is a 64-bit CMOS correlator operating at a clock frequency as high as 50 MHz. The correlator allows for easy cascading and it has threshold detection capability for detection of the peak of the cross-correlation function.

A 127 bit PRN sequence is suggested, but is not necessary. A 127 bit sequence will repeat every 2.54 μs when $F_{PRN} = 50$ MHz, which corresponds to 762 m of distance.

Please note that the use of PRN is not necessary to resolve the ambiguities. A phase of another CW signal, for example f_6, can be measured instead and combined with the phases of the other three for distance measurement. The only extra information one obtains from the cross-correlation of the reference and returned PRN sequences is the transfer function of the transmission medium. The transfer function can be used to mitigate multipath if it is a problem. Also note that PRN does not have to be transmitted continuously. Since the airborne platform will be moving at most 0.19 m/s (see Section 1.4), it will take 47 s for the platform to move 9 m and the distance measuring system will be able to resolve the ambiguity simply by updating the integer number of the ambiguities in the distance measurement.

The reason the PRN signal is present in the FLLOSS system is because the PRN signal may be used for 3-D positioning of the airborne platform as discussed below in Section 4.6.5.

The accuracy of the distance measurement based on the procedure discussed in this section equals the finest resolution $r_7 = 20$ μm of the wavelength measurement.

4.6 Other design issues

4.6.1 Calibration

The distance measurement system must be calibrated before any reliable data are obtained. A fine calibration can be performed in the SKA correlator that determines the time delay difference between signals received by LAR telescopes in a manner similar to that used at DRAO in the correlator designed for the Space VLBI [7]. The experience with VLBI shows that the resolution in the time delay measurement is in the order of a few picoseconds for the much more severe case of ionospheric dispersion, which is not a problem for the SKA [16]. The method of the time delay measurement is based on the work by A. E. E. Rogers (1970) [46]. The delay measurement is similar to the delay measurement using PRN discussed in Section 2.2.2.3. The simulations performed in Section 2.2.2.3 showed that with a conservative bandwidth $B = 500$ MHz and a SNR of 40 dB the accuracy of delay measurement is

$$accuracy \approx \frac{c}{B \times SNR} = \frac{3 \times 10^8}{500 \times 10^6 \times 10^4} = 70\ \mu\text{m}. \tag{4.9}$$

Let us assume that there is a reference antenna with a diameter of 10 m located at a known position. By observing a calibration source with the reference antenna and an LAR telescope and using time delay measurement techniques employed in Space VLBI, one can determine the focal length of the LAR. The 1σ rms noise temperature of this correlation interferometer is

$$T_\sigma \approx \sqrt{2}\frac{\sqrt{T_{LAR}T_{ref}}}{\sqrt{B \times \tau}}, \tag{4.10}$$

where T_{LAR} and T_{ref} are system noise temperatures of the two antennas (see Section 5.2.1), B is the bandwidth of the receiver, and τ is the integration time [8]. The integration time is limited by the amount of time it takes for the airborne platform to travel 0.1 m. The airborne platform will travel that distance in 0.5 s since the maximum velocity of the airborne platform is 0.19 m/s (see Section 1.4). Assuming that $T_{LAR} = T_{ref} = 50$ K and $\tau = 0.5$ s,

$$T_\sigma = 4.4 \times 10^{-3}\ \text{K}. \tag{4.11}$$

For a SNR of 40 dB, the change in antenna temperature due to the calibration source must be $T_a = 10^4 T_\sigma = 44$ K. The flux density in units of janskys[1] of the calibration source is

[1] 1 Jy (jansky) $= 10^{-26}\ \text{Wm}^{-2}\text{Hz}^{-1}$

$$S_{cal} = 2 \times 10^{26} \frac{kT_a}{A} \text{ [Jy]}, \tag{4.12}$$

where k is Boltzmann's constant and $A = 2(A_{LAR} \times A_{ref})^{1/2}$, where A_{LAR} is the effective area of the LAR and A_{ref} is the effective area of the reference antenna [8]. Thus assuming 50% efficiency of the two antennas

$$S_{cal} = 1 \text{ Jy}. \tag{4.13}$$

At this time, it is impossible to suggest usable calibrators since the location of the SKA is not known. However, for an LAR prototype planned to be built on the grounds of the DRAO, twelve circumpolar calibrators that have a flux density not lower than 1 Jy at 22 GHz are shown in Table 4.3. There are many more calibrators that have a flux density much higher than 1 Jy at frequencies lower than 22 GHz.

Note that only one reference antenna is required to calibrate every LAR telescope in the SKA. It is also possible to perform calibration by using only LAR telescopes. In this case a calibrator will be required to have a flux density higher than 50 mJy. If the reference antenna is not used, when calibrating outputs of a pair of LAR telescopes, the time delay measurement will take into account errors in focal distance measurement in both antennas. To correct for the errors, the output of each LAR telescope will have to be correlated with outputs of a few other LAR telescopes and the time delay for each LAR will be derived by analyzing the results of the correlations. Self-calibration or phase closure techniques applied to the SKA telescope will effectively perform this calibration.

4.6.2 Frequency of distance measurements

The airborne platform will be moving at a maximum speed of 0.19 m/s (see Section 1.4). It may therefore move through one unit of resolution of 20 μm used by the CRT in 105 μs. This suggests that the necessary measurements must be performed at most in that amount of time. 9,500 measurements per second does not appear to be unreasonably high. However, for resolution of 70 μm the rate can be reduced to 2,715 per second.

4.6.3 Phase measurement accuracy

As discussed in Section 4.4, the resolution or the accuracy of the three phase measurements suggested was $r_7 = 20\mu$m for $\lambda_7 = 2.56$ mm, $r_8 = 40\mu$m for $\lambda_8 = 7.28$ mm and $r_0 = 3$ mm for $\lambda_0 = 456$ mm. These and the round-off errors discussed in Section 4.5 assume accuracy of phase measurement of around $0.5\%\lambda$ or 1.8° of phase. This is

Calibrator	Coordinates		Flux density at 42.9 GHz	Flux Density at 15 GHz	Flux density at 1.5 GHz
	Right Ascension	Declination			
0102+584	1h2m46s	58°24′11″	2.4 Jy	2.3 Jy	0.9 Jy
0217+738	2h17m31s	73°49′33″	2.0 Jy	2.1 Jy	2.3 Jy
0228+673	2h28m50s	67°21′3″	1.4 Jy	2.3 Jy	1.3 Jy
0824+558	8h24m47s	55°52′43″	1.5 Jy	0.9 Jy	1.2 Jy
0841+708	8h41m24s	70°53′42″	0.8 Jy	2.2 Jy	4.0 Jy
0921+622	9h21m36s	62°15′52″	0.8 Jy	1.2 Jy	1.2 Jy
1153+809	11h53m12s	80°58′29″	1.1 Jy	1.4 Jy	1.4 Jy
1638+573	16h38m13s	57°20′24″	2.6 Jy	1.7 Jy	0.9 Jy
1800+784	18h0m46s	78°28′4″	2.4 Jy	3.0 Jy	1.8 Jy
1927+739	19h27m48s	73°58′1″	2.2 Jy	2.0 Jy	3.1 Jy
2005+778	20h5m31s	77°52′43″	1.3 Jy	1.6 Jy	1.0 Jy
2022+616	20h22m07s	61°36′59″	1.2 Jy	2.0 Jy	2.1 Jy

Table 4.3: Calibrators available for FLM calibration.

not an impossible task. Some simple Mini-Circuits I&Q Demodulators are capable of achieving this kind of phase accuracy. More complicated vector voltmeters such as the HP8405A have phase resolution as fine as 0.1°.

4.6.4 Minimum signal to noise ratio

Assume that the signal at the output of the LO system is

$$y(t) = P\cos(\omega_0 t + \phi(t)) + n_i(t), \tag{4.14}$$

where $n_i(t)$ is band-limited noise with power spectral density (PSD) $S_{n_i}(\omega)$, in bandwidth BW centered around ω_0. The bandpass noise is expressed in terms of its quadrature components as

$$n_i(t) = n_c\cos\omega_0 t + n_s(t)\sin\omega_0 t, \tag{4.15}$$

or in terms of its envelope, $E_n(t)$, and phase, $\Theta_n(t)$, as

$$n_i(t) = E_n(t)\cos(\omega_0 t + \Theta_n(t)), \tag{4.16}$$

where

$$E_n(t) = \sqrt{n_c^2(t) + n_s^2(t)} \tag{4.17}$$

and

$$\Theta_n(t) = \arctan \frac{n_s(t)}{n_c(t)}. \tag{4.18}$$

Thus

$$\begin{aligned} n_c(t) &= E_n(t) \cos \Theta_n(t) \\ n_s(t) &= E_n(t) \sin \Theta_n(t). \end{aligned} \tag{4.19}$$

Therefore, combining Equations 4.14 and 4.16 one obtains

$$y(t) = R(t) \cos(\omega_0 t + \phi(t) + \Delta\phi(t)), \tag{4.20}$$

where

$$R(t) = \sqrt{P^2 + E_n^2 + 2PE_n \cos(\phi(t) - \Theta_n(t))} \tag{4.21}$$

and

$$\phi(t) + \Delta\phi(t) = \arctan \frac{P \sin \phi(t) + E_n \sin \Theta_n(t)}{P \cos \phi(t) + E_n \cos \Theta_n(t)}. \tag{4.22}$$

The LO requires the phase error, $\Delta\phi(t)$, be not greater than 5° at 22 GHz. This corresponds to 5°(657 MHz/22 GHz) = 0.15° phase error in the output of the LO system operating at 657 MHz . Therefore

$$\arctan \frac{P \sin \phi(t) + E_n \sin \Theta_n(t)}{P \cos \phi(t) + E_n \cos \Theta_n(t)} - \phi(t) \leq 0.15°. \tag{4.23}$$

Now assume that the phase $\phi(t)$ is zero. Then

$$\frac{E_n \sin \Theta_n(t)}{P + E_n \cos \Theta_n(t)} \leq 2.62 \times 10^{-3}. \tag{4.24}$$

For Equation 4.24 to be always true, the ratio between the noise amplitude and the signal amplitude must be $\frac{P}{E_n} \geq 382$. Therefore the LO system requires $SNR \geq$ 52 dB. However, there are other errors that will appear in the LO system due to the system dynamic response. Therefore a better SNR is preferred.

A similar calculation is applied to investigate the SNR for the phase measurement in the FLM. In this case, however, the allowable phase error is in the order of 1° and Equation 4.24 is rewritten as

$$\frac{E_n \sin \Theta_n(t)}{P + E_n \cos \Theta_n(t)} \leq 0.017. \tag{4.25}$$

Therefore the SNR for this case must be at least 35 dB.

4.6.5 Antennas

According to the discussions in Sections 4.3 and 4.4, the antennas required for the FLLOSS will have a relative bandwidth of the transmitted signals of about 1 : 10 with the centre frequency of $f_m = 39.88$ GHz or $\lambda_m = 7.52$ mm. The antennas will have to be circularly polarized so that changes in the mutual orientation of the antennas will not cause a loss of signal. The size and weight of the airborne antenna must be minimal.

The attitude of the airborne platform will be adjusted automatically so that its feed surface is always perpendicular to the axis of the LAR. Therefore the FLLOSS airborne antenna positioned on the surface of the LAR telescope feed will be pointed at the centre at the LAR at all times. A relatively high-gain antenna can thus be employed to improve the SNR. The half-power beamwidth (HPBW) for the antenna cannot be recommended at this time since it is not clear how well the positioning of the airborne platform can be accomplished. A patch antenna having dimensions in the order of λ_m is expected to perform adequately.

The ground antenna might be steered in order to follow the airborne platform. A narrow beam from the ground antenna has two advantages. First of all, a narrow-beam antenna has a large gain. Second, the effects of multipath are reduced since the antenna only receives signals coming from the points illuminated by the narrow beam.

It is suggested that the ground antenna should be designed as an array of four antennas arranged in a square pattern. This will enable the FLLOSS to employ angle-tracking techniques used in monopulse radars to determine where the airborne platform is located by comparing the signals' phases and amplitudes as they are received [49]. According to Skolnik (1970), the precision of angle measurement can reach 0.003°[49]. With that precision, the 3-D position of the airborne platform can be determined with the FLM with a precision of $500 \tan 0.003 = 26$ mm, where the focal length is assumed to be 500 m. The ground antenna must be rotated around its phase centre; otherwise, additional phase errors will contaminate the phases of the signals used for distance measurement [31]. The beamwidth of the ground antenna will have to be selected when the locations of the LAR telescopes in the SKA are known. The main parameters to consider will be the SNR of the signals, the cross-talk between the FLLOSS's from different LAR telescopes, and the ability of the ground unit to track the airborne platform. Choosing different operating frequencies for neighboring LAR telescopes will diminish the cross-talk. However, the frequencies must be selected so that the wavelengths are integer multiples of measurement resolutions since the CRT only works with integers.

4.7 Conclusion

The configuration of the FLLOSS system has been discussed in this chapter. A block diagram of the system has been shown, outlining its most important parts. However, a more detailed diagram will be required for system implementation. Use of surface mounted electronic components will make the system light weight. It is expected that the system will be able to perform according to the specifications.

Frequencies of operation for the FLLOSS have been suggested. The selected frequencies lie in the standard Q-band. The configuration of the frequencies enables the FLLOSS system to ease ambiguity resolution. The PRN code may be used for 3-D airborne platform positioning.

A procedure for distance measurement based on the CRT has been recommended. The procedure is useful as it helps with ambiguity resolution.

Using monopulse radar techniques, angle-tracking becomes possible adding 3-D position measuring capability to the FLM system.

The LO system is required to produce a phase with an error of less than 5°rms at 22 GHz. This condition will be achieved if the phase error of the LO system at 657 MHz is less than 0.15°rms; this can be achieved in the Cascaded PLL LO system. A more detailed design of the LO system will be shown in the next chapter.

Chapter 5

LO system prototype design

5.1 Introduction

The design of the complete FLLOSS was presented in the previous chapter. However, because of cost reasons and limited time resources, the prototype of the complete system was not built. Nevertheless, a simplified prototype of the LO system operating at frequencies lower than those suggested in the previous chapter has been constructed and is described in this chapter. The design of the final LO system can be based on the design of the prototype and similar performance can be expected from the final LO system.

The LO system configuration has been selected in Chapter 3. This chapter describes the design and implementation of an LO prototype system. The chapter begins with the design of the system and explanation of its critical parts. Implementation and testing are discussed in the second half of the chapter.

5.2 Background

5.2.1 Link budget and signal to noise ratio

Any signal emitted from an antenna experiences power attenuation in the transmission medium. For a free space radio link the attenuation is described as follows:

$$L_{FS} = \left(\frac{\lambda}{4\pi d}\right)^2, \tag{5.1}$$

where λ is the wavelength of the signal and d is the distance from the transmitting antenna to the receiving antenna [31].

Noise acquired in the transmission medium is white Gaussian thermal noise. The

power generated by the noise is

$$N = kTB, \tag{5.2}$$

where k is Boltzmann's constant, B is the bandwidth of the system and T is the noise temperature in kelvins. Noise temperature is the temperature of a fictitious thermal noise source that generates the same amount of added noise power at the output as the thermal noise [45]. Components in an electronic system also produce additional internal noise. The measure of the noise power is the system noise temperature T_e.

Another measure of the noise power produced by the electronic components is the noise figure (NF). The noise figure is the ratio between the noise power at the output of a system and the noise power at the input. The noise figure and the system noise temperature are related as follows

$$T_e = T_0(NF - 1), \tag{5.3}$$

where NF is the noise figure and $T_0 = 290$ K is the standard reference temperature. Another important relationship is of the noise figure of a matched transmission line with attenuation, L:

$$NF = 1 + \frac{T_L}{T_0}(L - 1), \tag{5.4}$$

where T_L is the physical temperature.

The noise figure of cascaded components is calculated according to the following equation

$$NF = NF_1 + \frac{NF_2 - 1}{Gain_1} + \frac{NF_3 - 1}{Gain_1 Gain_2} + \dots, \tag{5.5}$$

where NF_1, NF_2, NF_3, etc. are the noise figures of the consecutive stages in the system and $Gain_1$, $Gain_2$, etc. are the power gains of the stages [24].

Assuming there is no interference, the SNR is calculated from

$$SNR_{dB} = (G_{AT})_{dB} + (P_{TX})_{dBW} + (G_{AR})_{dB} - (L_{FS})_{dB} - (kTB)_{dB}, \tag{5.6}$$

where $(P_{TX})_{dBW}$ is the transmitted power relative to 1 W, G_{AT} and G_{AR} are the gains of the transmitting and receiving antennas, L_{FS} is the free-space loss, and T is the noise temperature of the system whose bandwidth is B. Equation 5.6 is also called the link budget.

5.2.2 Effect of impedance mismatches on signal phases

One of the main problems in the LO system is impedance mismatches in the cables and in the connectors. Figure 5.1 shows how a reflected signal added to the signal of interest affects the phase of that signal. The standing wave ratio (SWR) of

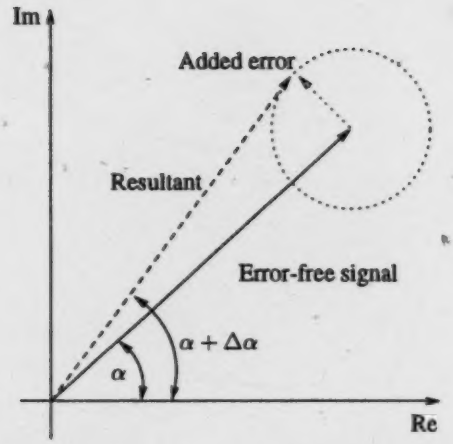

Figure 5.1: Generation of phase errors due to impedance mismatches.

amplifiers used in implementation of the LO prototype was SWR = 2, thus the reflection coefficient is $\Gamma = \frac{1}{3}$, giving a phase error which could be as large as 18.4°. This simple example shows how phase errors due to impedance mismatches are introduced into any system.

5.3 LO prototype design

Design of a prototype of the Cascaded PLL LO system is discussed in this section. The LO system is a feedback control system operating in free space over a radio link.

5.3.1 Selection of frequencies for use in LO prototype

The frequency spectrum of the LO system to be used in the SKA was discussed in Chapter 4. The signals discussed below are for the prototype only and will not be used in the final LO system.

The prototype frequencies have to be high enough so that they can be transmitted with relatively small antennas since at least one of the antennas has to be movable to simulate the motion of the airborne platform. However, there is a limit on how high the prototype frequencies can be, though. To reduce the cost of the prototype and reduce component delivery times, it was decided to use off-the-shelf components available from Mini-Circuits. However, most Mini-Circuits components have an upper frequency limit around 3 GHz.

Even though the prototype will have three very narrowband signals transmitted between two antennas pointed directly at each other, some of the signal will not be received, producing interference to other users of the frequency bands. Therefore, the frequencies must be selected so that they do not lie in protected frequency bands.

To simplify antenna design, it would be beneficial if the ratio between the highest and the lowest frequency was as small as possible to minimize the relative bandwidth. By carefully analyzing Figure 3.5, one can notice that the minimum ratio in the Cascaded PLL system approaches $2:1$. In this limiting case, however, two of the three signals have almost identical frequencies.

The three frequencies selected for the prototype are summarized in Table 5.1.

Prototype frequency	Radio bands as published by ITU (1982) [28]
$F_0 = 3.15$ GHz	Radiolocation: 3.10 GHz – 3.30 GHz
$F_{ref} = 1.35$ GHz	Aeronautical Radionavigation (radiolocation): 1.3 GHz – 1.35 GHz Radiolocation: 1.35 GHz – 1.40 GHz
$F_a = F_0 - F_{ref} = 1.80$ GHz	Fixed mobile: 1.71 GHz – 1.93 GHz

Table 5.1: Frequencies selected for the LO prototype.

5.3.2 Preliminary prototype configuration discussion

A diagram of the Cascaded PLL LO prototype system is shown in Figure 5.2. The system consists of the ground unit and the remote unit communicating with each other by means of a radio link. The main electronic components of the system to be designed are the USG, LSG and the phase-halving PLL.

The USG has two inputs, 1.35 GHz and 1.8 GHz, and it outputs their sum, 3.15 GHz. The same frequencies are present in the LSG but the 1.8 GHz signal is the output. A mixer at the input of the LSG and the USG produces the required output. The output of the mixer must be filtered to remove unwanted harmonics. There are two alternatives when it comes to filtering. One alternative is to use a narrowband PLL that would lock onto the correct signal and effectively filter out everything else. The other alternative is to use a passive bandpass filter. The bandpass filter method will not be useful if unwanted signals are very close to the passband simply because it is very difficult to construct very narrow bandpass filters. The narrowband filter would have a large number of poles at the edges of the band to increase the attenuation in the rejection region. However, the poles produce strong phase variations at the edges. A PLL on the other hand can have a very narrow bandwidth. PLLs also produce high power output, thus removing the need for an amplifier stage after the mixer.

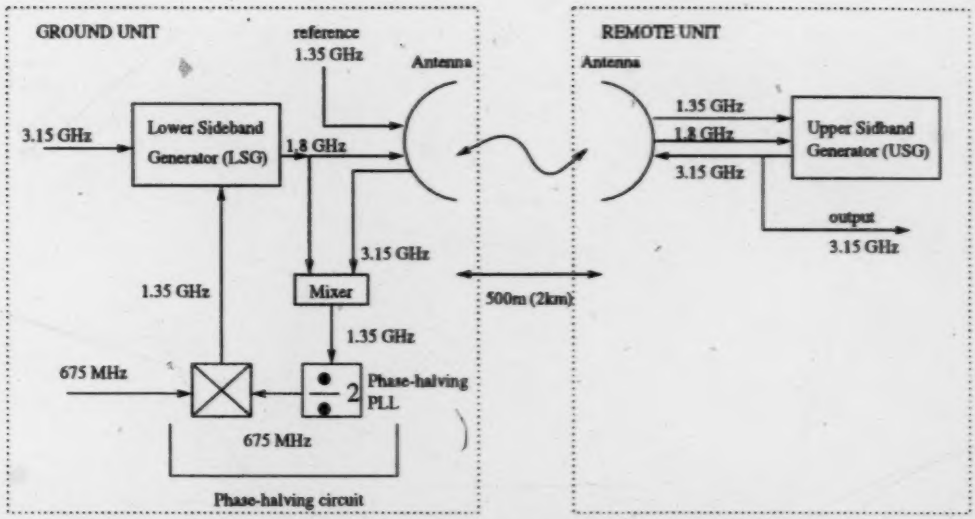

Figure 5.2: Cascaded PLL LO prototype diagram. Initially the LO prototype has been designed for 2 km focal distance. The specification, however, was later reduced to 500 m.

Even though PLL filters appear to be superior to simple bandpass filters, it was decided to use bandpass filters in the prototype. It is possible to use bandpass filters since the signals are widely separated and very narrow passband filters are not necessary. Cost and time considerations were the main factors behind this decision.

As discussed in Section 3.4.1.2, when the USG and the LSG are not based on PLLs, the transfer function of the LSG and the USG become equal to one and drop out from the transfer function of the LO system. The design of the phase-halving PLL is therefore the most important part of the prototype design.

5.3.3 Noise Considerations for the LO system

There are three separate parts of the system that are susceptible to noise. The phase-halving PLL will have noise introduced by the VCO and by the loop filter. The noise in the transmission medium is also a source of errors. Another disturbance is of course the effect on the system of distance changes between the ground and the remote units. Each possible source of errors will be considered separately below.

5.3.3.1 Noise introduced in phase-halving PLL

The phase-halving circuit is the only active component of the LO prototype system. The noise response of this circuit will greatly affect the noise response of the entire

system. The noise, $D(s)$, is modelled in Figure 5.3.

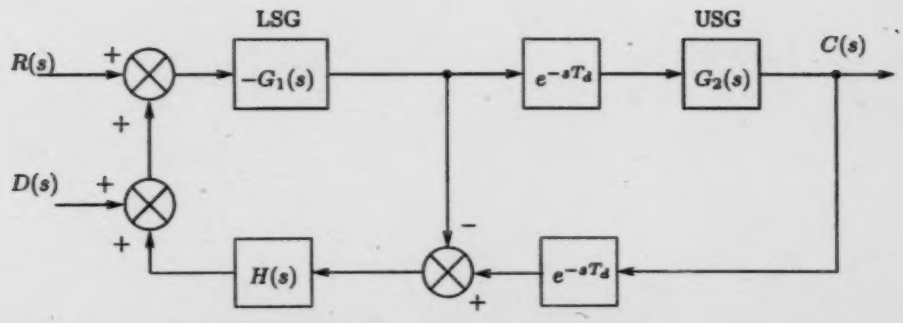

Figure 5.3: Noise introduced in phase-halving PLL. $H(s)$ denotes the transfer function of the phase-halving PLL.

By setting $R(s) = 0$, one obtains the transfer function relating the output of the system and the disturbance. It is clear that the transfer function is identical to the transfer function of the LO system shown in Equation 3.36 and illustrated in Figure 3.9 since the disturbance $D(s)$ is directly added to the input $R(s)$. Therefore, any disturbance produced in the PLL will appear at the output of the LO system. This clearly shows that extra attention must be paid when building the phase-halving PLL.

5.3.3.2 Noise acquired in the uplink

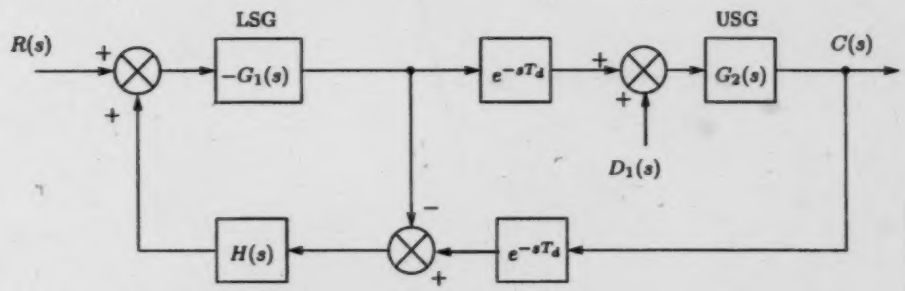

Figure 5.4: Noise acquired in the uplink transmission medium.

Noise acquired in the uplink path can be analyzed by introducing disturbance $D_1(s)$ as shown in Figure 5.4. By setting $R(s) = 0$, one obtains the transfer function relating the output of the system and the disturbance:

$$\frac{C(s)}{D_1(s)} = \frac{G_2}{1 + e^{-2sT_d}\frac{G_1G_2H}{1-G_1H}}. \tag{5.7}$$

Again assuming that $G_2 = 1$ and $G_1 = 1$, the noise frequency response is described by

$$\frac{C(s)}{D_1(s)} = \frac{1}{1 + e^{-2sT_d}\frac{H(s)}{1-H(s)}}. \tag{5.8}$$

The performance of the LO system is clearly dependent on the phase-halving PLL.

Equation 5.8 suggests that at low noise frequencies where $H(s) = \frac{1}{2}$ and $e^{-2sT_d} \approx 1$ the transfer function $\frac{C(s)}{D_1(s)} \approx \frac{1}{2}$ thus attenuating the uplink noise by 6 dB. As the frequency increases the denominator in Equation 5.8 becomes equal to one and the uplink noise is not attenuated any more.

5.3.3.3 Noise acquired in the downlink

The noise introduced in the downlink is modelled with disturbance $D_2(s)$ in Figure 5.5.

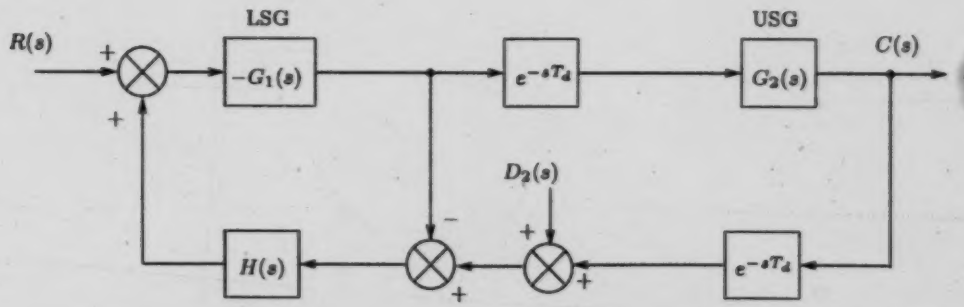

Figure 5.5: Noise acquired in the downlink transmission medium.

The response to noise $D_2(s)$ is then described by the following transfer function:

$$\frac{C(s)}{D_2(s)} = \frac{-\frac{G_1G_2He^{-sT_d}}{1-G_1H}}{1 + \frac{G_1G_2He^{-2sT_d}}{1-G_1H}}. \tag{5.9}$$

Since $G_1 = G_2 = 1$, the transfer function can be simplified to

$$\frac{C(s)}{D_2(s)} = \frac{-H(s)e^{-sT_d}}{1 + H(s)(e^{-2sT_d} - 1)}. \tag{5.10}$$

When the noise frequency is low, $\frac{C(s)}{D_2(s)} \approx -\frac{1}{2}$ and the noise is attenuated by 6 dB. However as the frequency increases beyond the bandwidth of the phase-halving PLL, the noise is greatly attenuated.

5.3.3.4 Noise due to the motion of airborne platform

The noise response of the LO system due to distance changes is modelled in Figure 5.6. The transfer function relating the output to the disturbance $L(s)$ is shown in

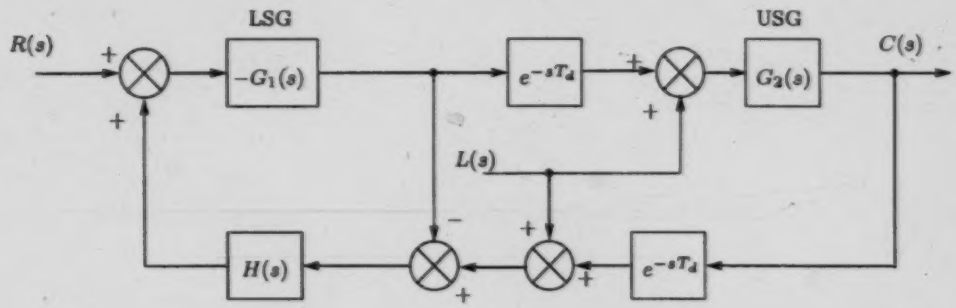

Figure 5.6: Disturbance due to the distance change.

Equations 3.37, 5.11 and 5.12.

$$\frac{C(s)}{L(s)} = \left(1 - \frac{G_1(s)H(s)}{1 - G_1(s)H(s)}e^{-sT_d}\right) \frac{G_2(s)}{1 + \frac{G_1(s)H(s)}{1-G_1(s)H(s)}G_2(s)e^{-2sT_d}}, \tag{5.11}$$

or

$$\frac{C(s)}{L(s)} = \frac{\left(1 - G_1(s)H(s) - G_1(s)H(s)e^{-sT_d}\right)G_2(s)}{1 + G_1(s)H(s)\left(G_2(s)e^{-2sT_d} - 1\right)}. \tag{5.12}$$

When the distance does not change, i.e. $s = 0$, $G_1(s) = G_2(s) = 1$, $H(s) = \frac{1}{2}$ and $e^{-2sT_d} \simeq 1$. In this case according to Equation 5.12, $\frac{C(s)}{L(s)} = 0$. That is in fact what is desired from the system.

In the case when sideband generators are based on passband filters, $G_1 = G_2 = 1$, and $\frac{C(s)}{L(s)} = \frac{1-H-He^{-sT_d}}{1+H\left(e^{-2sT_d}-1\right)}$. Thus when the variations in the distance happen at high

frequency such that $H(s) \ll \frac{1}{2}$, the LO system will not be able to perform properly since the distance variations will show at the output. This however is corrected by setting the bandwidths of G_1 and G_2 appropriately narrow so that the transfer function in Equation 5.12 approaches zero as the frequency of distance variations increases. Note that to control the bandwidths of G_1 and G_2, the LSG and the USG must be PLL based.

5.3.4 LO prototype simulations

The time delay present in the LO system creates some difficulty when it comes to designing the LO system. The main problem is that the time delay, T_d, is represented by a non-linear transfer function e^{-sT_d}. To analyze the LO behaviour in the presence of the time delay, MATLAB/SIMULINK software by the MathWorks was used. The LO system was simulated in the phase domain. The phase-halving PLL was simulated by its transfer function and the USG and the LSG were simulated by an adder and a subtracter respectively.

First of all, it is necessary to know how the bandwidth and damping of the phase-halving PLL affect the stability and dynamic response of the LO system. The effects of noise picked up in the transmission medium are also important to investigate, as well as the sensitivity of the LO system to changes in time delay.

There are two variables that are optimized in the simulation, namely, the damping ratio, ζ, of the PLL, and the natural frequency, ω_n, of the PLL. In the optimum case, the step response will not have ringing or very large overshoots while settling to the desired value. The noise rejection must be optimized also.

Initially the nominal focal length was 2 km; therefore the time delay used in the simulations was $T_d = 7.5\ \mu s$ which corresponds to 2 km of distance plus some additional delay to simulate delays in electronic components. Even though the damping ratio is a variable in the simulations, it was kept bounded to $0.5 \leq \zeta \leq 1$ since it is the optimum region for damping ratio in PLLs [20].

The LO simulations show that $\zeta = 0.707$ and $\omega_n = 2\pi \times 2 \times 10^3$ rad/s is close to an optimum combination for this system. Figures 5.7, 5.8, 5.9 and 5.10 show simulated performance of the LO system as the damping ratio and natural frequency of the phase-halving PLL change. Figure 5.10 is very important as it should be used to determine whether the LO system is able to remove the effects of airborne platform motion on LO output phase. To determine if the motion will not affect the phase of the LO system output, the power spectral density of the airborne platform velocities should be multiplied by an appropriate plot shown in Figure 5.10.

Usually, however, when the optimum is found the loop parameters do not have to be adjusted to exactly the optimum values. The extremum is normally quite broad to an extent that moderate deviations from the optimum values have very

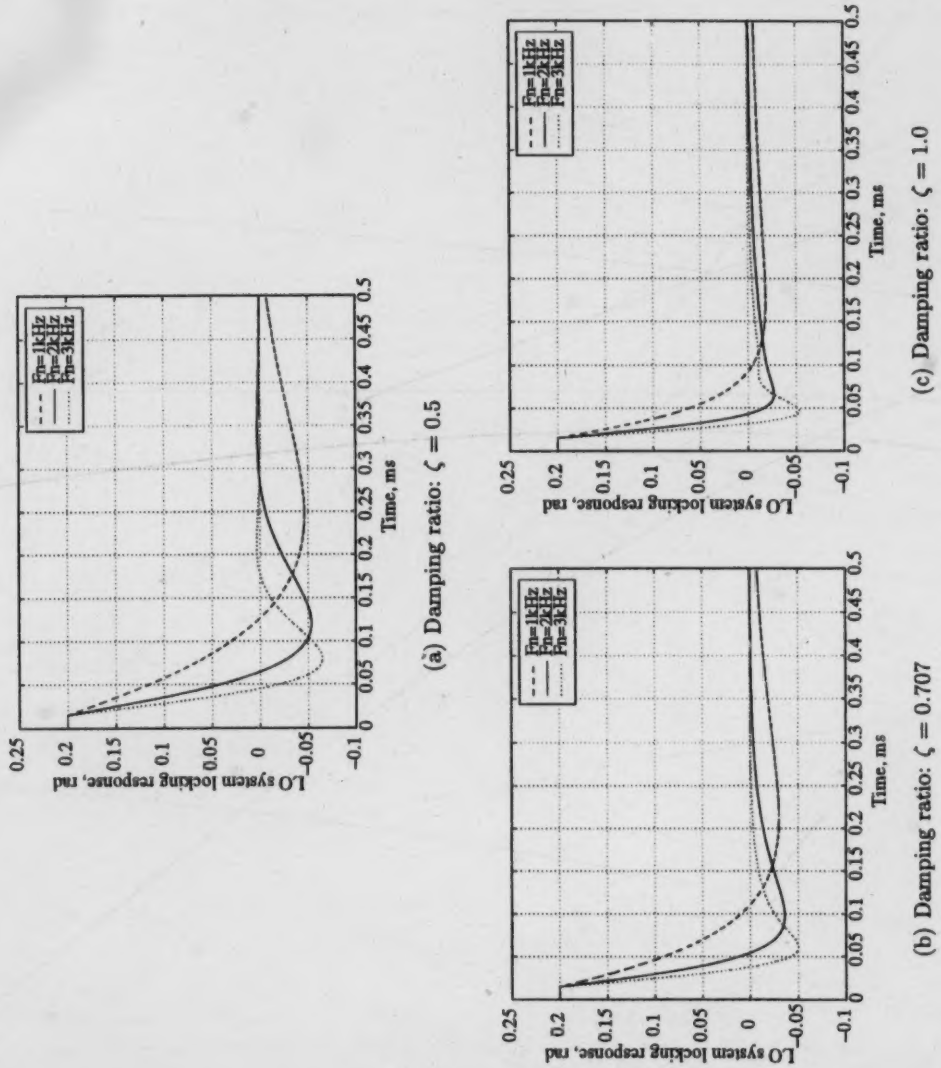

Figure 5.7: Behaviour of error signal $R(j\omega) - C(j\omega)$ of the LO system as it acquires lock. The initial state of $C(j\omega)$ differed by 0.2 rad from the phase $R(j\omega)$. Transfer functions of the USG and the LSG were assumed to be 1. $R(j\omega)$ and $C(j\omega)$ are shown in Figure 5.3. F_n is the natural frequency expressed in hertz.

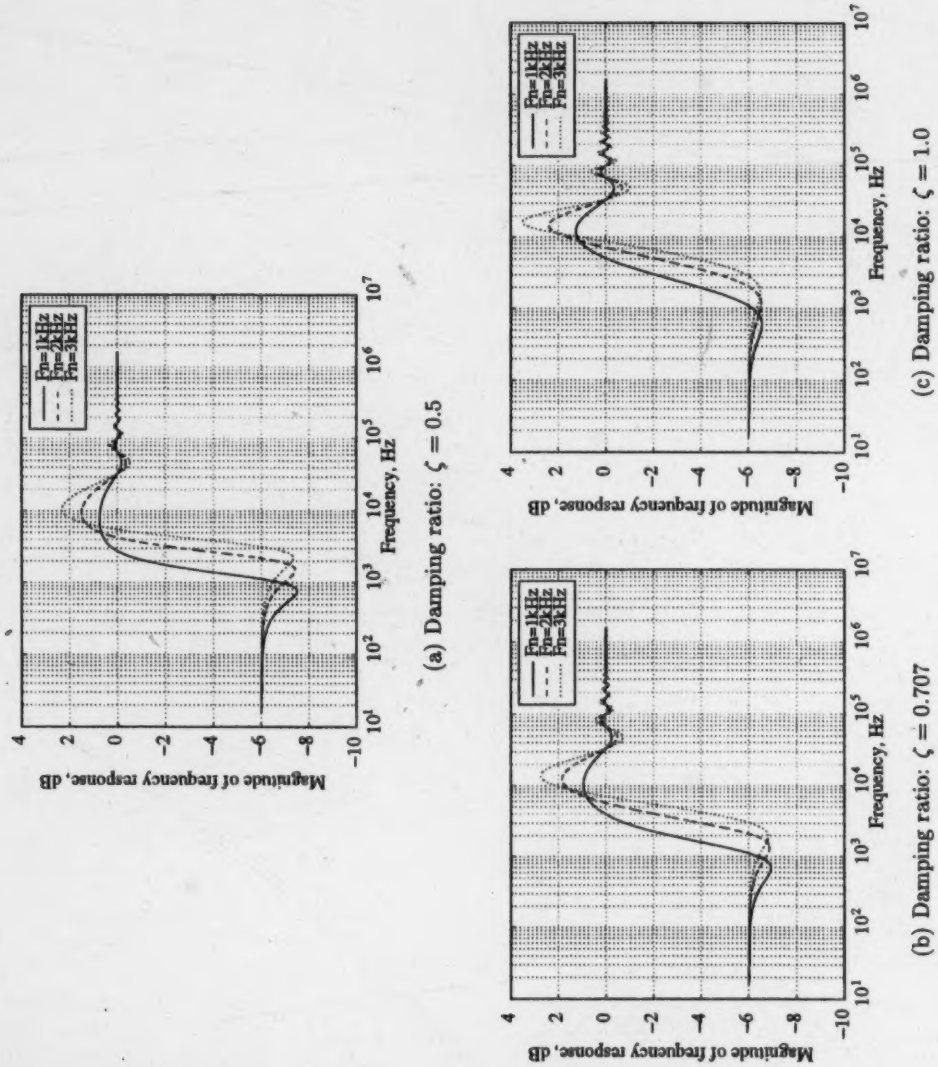

Figure 5.8: Frequency response from noise input $D_1(j\omega)$ to phase output $C(j\omega)$ of the closed loop LO system shown in Figure 5.4. Transfer functions of the USG and the LSG were assumed to be 1. F_n is the natural frequency expressed in hertz.

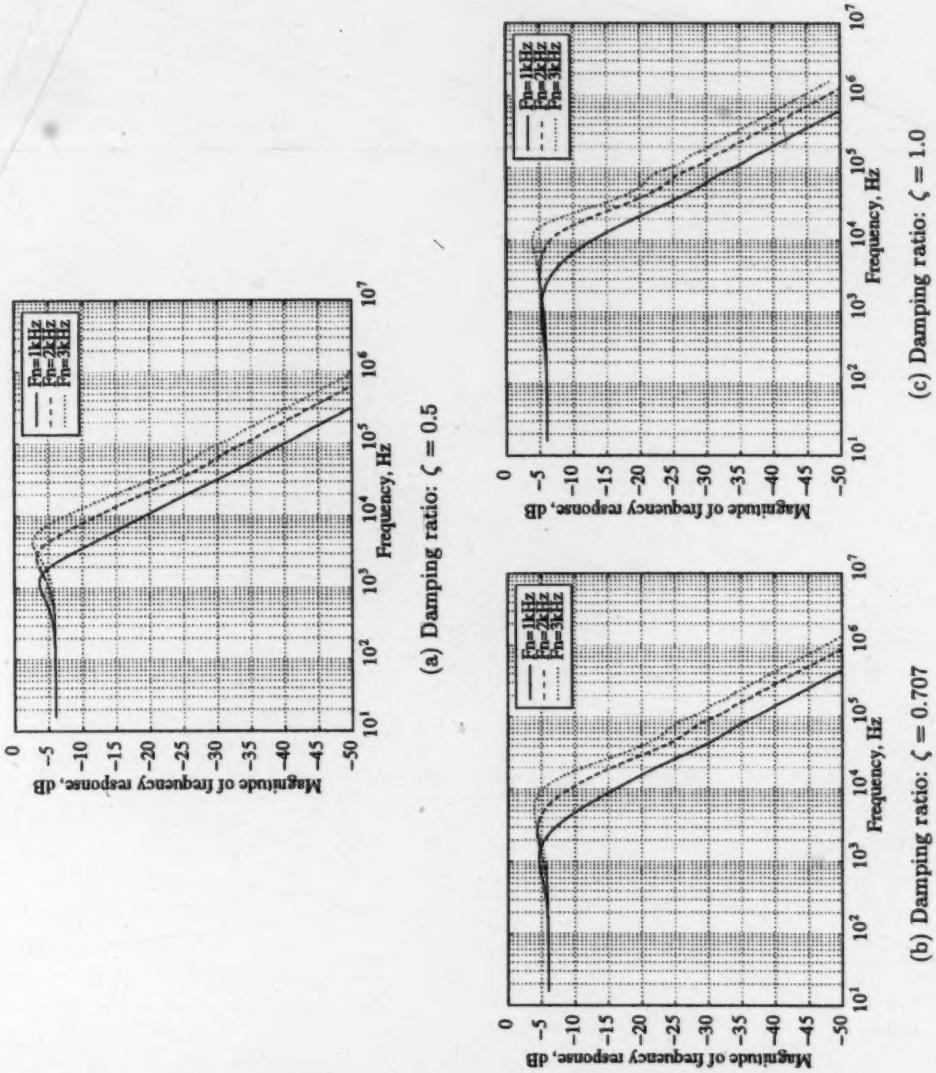

Figure 5.9: Frequency response from noise input $D_2(j\omega)$ to phase output $C(j\omega)$ of the closed loop LO system shown in Figure 5.5. Transfer functions of the USG and the LSG were assumed to be 1. F_n is the natural frequency expressed in hertz.

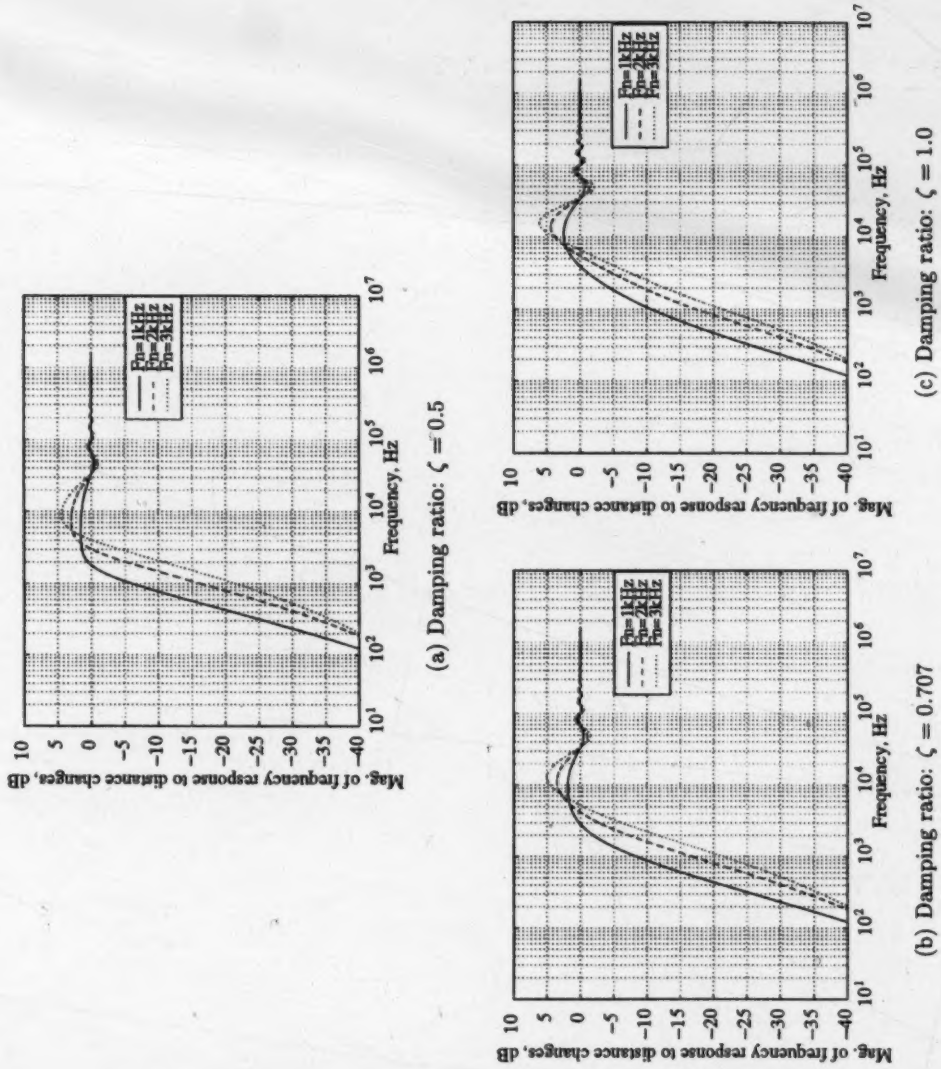

Figure 5.10: Frequency response from input $L(j\omega)$ to phase output $C(j\omega)$ of the closed loop LO system shown in Figure 5.6. Transfer functions of the USG and the LSG were assumed to be 1. F_n is the natural frequency expressed in hertz. The time delay in this simulation was 7.5 μs.

little effect on the system performance [20].

Landecker and Vaneldik (1982) state that if $T_d < \frac{1}{2\omega_{3dB}}$, where ω_{3dB} is the bandwidth of the phase-halving PLL, then the effect of the time delay is very little [32]. The bandwidth, ω_{3dB}, of the PLL is found from

$$|2 \times H(j\omega_{3dB})|^2 = 0.5 \tag{5.13}$$

as

$$\omega_{3dB} = \omega_n \left[8\zeta^2 + 2 + \sqrt{(8\zeta^2+2)^2+4}\right]^{1/2} = 2\pi \times 7.0 \times 10^3 \text{ rad/s}. \tag{5.14}$$

This satisfies the condition suggested by Landecker and Vaneldik since $(2 \times 2\pi \times 7.0 \times 10^3)^{-1} > 7.5\ \mu$s.

The time delay was varied and the variations in the phase at the output of the LO system as it was acquiring lock was plotted in Figure 5.11. In the simulation

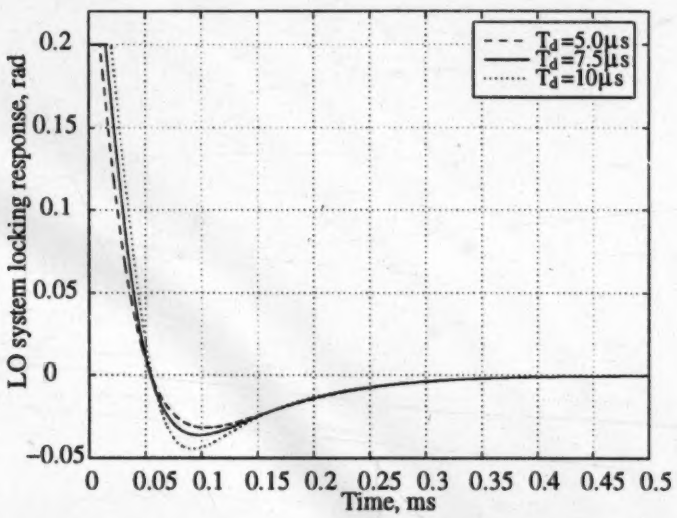

Figure 5.11: Behaviour of error signal $R(j\omega) - C(j\omega)$ of the LO system as it acquires the lock for three different values of the time delay. The initial state of $C(j\omega)$ differed by 0.2 rad from the phase of the $R(j\omega)$ which was kept constant. Transfer functions of the USG and the LSG were assumed to be 1. $R(j\omega)$ and $C(j\omega)$ are shown in Figure 5.3.

the time delay was drastically changed by 2.5 μs which is equivalent to a distance change of 750 m. It is clear that the time delay change has no significant impact on

the system performance.

5.3.5 Phase-halving PLL design

The phase-halving PLL is the most important part of the LO system. It defines the steady-state errors and the dynamic performance of the LO system as discussed in Section 3.4.1.2. The transfer function of the phase-halving PLL is:

$$\frac{C(s)}{R(s)} = \frac{2\zeta\omega_n s + \omega_n^2}{s^2 + 4\zeta\omega_n s + 2\omega_n^2}. \tag{5.15}$$

Figure 5.12 shows the block diagram of the phase-halving PLL.

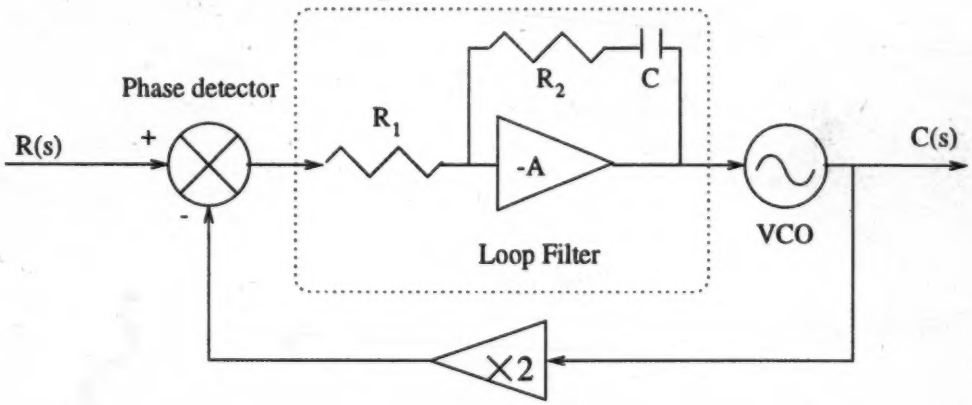

Figure 5.12: Phase-domain diagram of the phase-halving PLL system diagram.

Design of PLLs is well understood and was briefly described in Section 3.2.1.4. The most suitable phase-halving PLL will keep the LO system stable while providing the best achievable steady-state errors and the best achievable dynamic response to expected disturbances.

5.3.5.1 Component selection

Phase detector: A mixer is a phase detector; however, better performance can be achieved by using digital phase-frequency detectors. In fact, the lock limits are extended by 2π when mixers are replaced by phase-frequency detectors [20]. There are some phase-frequency detectors that also provide frequency sweep to assist with frequency lock. The natural locking process of a PLL can take a very long time [20].

A digital ultrahigh speed phase/frequency discriminator (PFD), AD9901, was selected as the phase detector for the PLL. The advantage of using a PFD is that it produces a sweep in the error voltage proportional to the frequency difference. When the frequencies of the input signals become very close, however, the output is proportional to the phase difference of the input signals.

The AD9901 PFD is a digital circuit designed to avoid the "dead-zone" very common in digital PFDs. The "dead-zone" occurs at the lock point where the gain of the PFD goes to zero, increasing the phase noise in the output. The gain of this PFD is $K_d = 0.285$ V/rad and it operates at frequencies as high as 200 MHz.

An ultrafast comparator, AD96687, is selected to precede the PFD. Both devices operate at the same logic levels and are compatible with each other.

VCO: Crystal oscillators have very low gain and their tuning range is limited. The maximum frequency of crystal oscillators does not exceed 200 MHz at the present time. Therefore, a crystal oscillator was not selected as a VCO, even though crystal oscillators are very stable. A transistor microwave oscillator using a high-Q cavity was selected instead and is shown in Figure 5.13. This

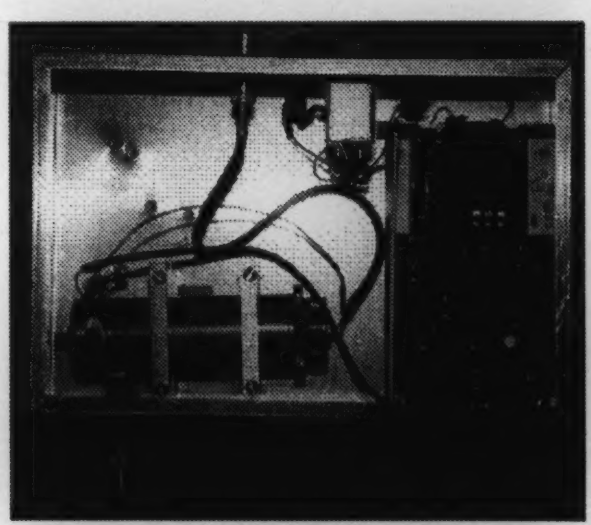

Figure 5.13: Photograph of the VCO used in the LO prototype.

VCO has an output power of +25 dBm, a tuning range of more than 10 MHz, and a loaded quality factor $Q \approx 70 \times 10^3$. The gain of the VCO was measured as $K_0 = 4.71 \times 10^6$ rad/(sV).

Loop filter: A very common operational amplifier, OP177GP, was selected for the loop filter. A typical open loop gain for this operational amplifier is $A = 12 \times 10^6$. A low noise operational amplifier may be required to reduce the noise in the PLL when the final FLLOSS is designed. Thus, OP177GP may be replaced by another operational amplifier with a better noise figure.

5.3.5.2 PLL loop filter design

The LO system simulations performed in Section 5.3.4 suggested design values of $\zeta = 0.707$ and $\omega_n = 2\pi \times 2 \times 10^3$ rad/s. These of course were designed for the time delay of 7.5μs. The distance of 2 km was not available for easy access, therefore it was decided to test the prototype over a distance of 800 m . Later the focal length of the LAR telescope decreased from 2 km. The natural frequency of the PLL is inversely proportional to the time delay; thus, for the test purposes a natural frequency $\omega_n = 2\pi \times 2 \times 10^3 \frac{2000}{800} = 2\pi \times 5 \times 10^3$ rad/s and bandwidth $\omega_{3dB} = 2\pi \times 17.5 \times 10^3$ rad/s were selected, using the relation given in Equation 5.14.

The values for the loop filter time constants can now be found as discussed in Section 3.2.1.4: $\tau_1 = \frac{2K_0K_d}{\omega_n^2} = 2.7$ ms and $\tau_2 = \frac{2\zeta}{\omega_n} = 45\ \mu$s.

The following values were selected for the loop filter components: $C = 1800$ pF, $R_1 = 1.5$ MΩ and $R_2 = 27$ kΩ (see Figure 5.12).

5.4 LO prototype implementation

5.4.1 PLL implementation

The PFD is limited to 200 MHz maximum frequency of operation. However, the input to the phase-halving PLL is 1.35 GHz. Therefore the inputs to the PFD must be shifted to lower frequencies in the PFD operation band. A free running VCO was used for that purpose. The VCO was not locked to any external frequency source. However, since the output of the VCO was used to frequency shift both input signals, the resultant signals kept their intrinsic phase relationship. The circuit diagram of the phase-halving PLL is shown in Appendix B. The amplifier labelled "Amplifier A" in Figure B.2 was inserted to provide a means for adjusting the gain of the loop filter in case the gain of the PFD was not exactly according to specifications. Figure 5.14 shows a photograph of the assembled phase-halving PLL.

5.4.1.1 Phase-halving PLL phase stability measurement

The PLL was then tested to see how well it could stay locked over long periods of time. The measurement was taken over twelve hours. The system was not being used for a while before the measurement; thus, all components experienced a warm

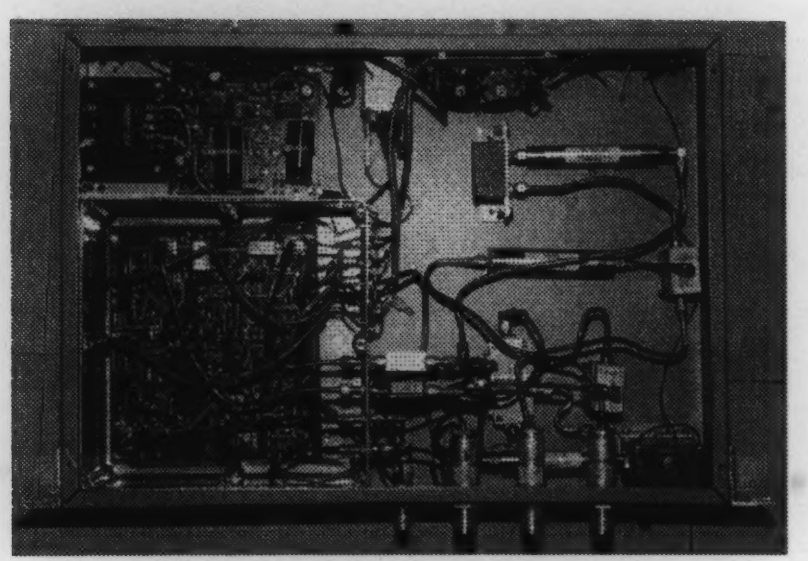

Figure 5.14: Assembled phase-halving PLL.

up period during the measurement. Figure 5.15 shows that the PLL stayed locked and the phase difference between the input to the PLL and the output did not vary by more than 0.36°.

5.4.2 Antenna design and implementation

A paraboloidal antenna concentrates the received electromagnetic signal at its focus and the signal is transformed from a travelling electromagnetic wave into a voltage signal by another antenna located at the focus. That antenna is called the "feed". The performance of a paraboloidal antenna depends strongly on the feed.

The paraboloidal antennas required for the LO prototype are pointed at each other. One of the antennas simulates the ground antenna. The other simulates the antenna located at the airborne platform and therefore is movable.

The polarization of a paraboloidal antenna is determined by the polarization of its feed. Circular polarization was chosen to avoid signal loss due to misalignment.

5.4.2.1 Feed design

A simple circularly polarized antenna that can be used as a feed is a helical antenna. A helical antenna is a broadband antenna. It is capable of covering the frequency range between 1.35 GHz and 1.8 GHz; however, it is not possible to operate the same

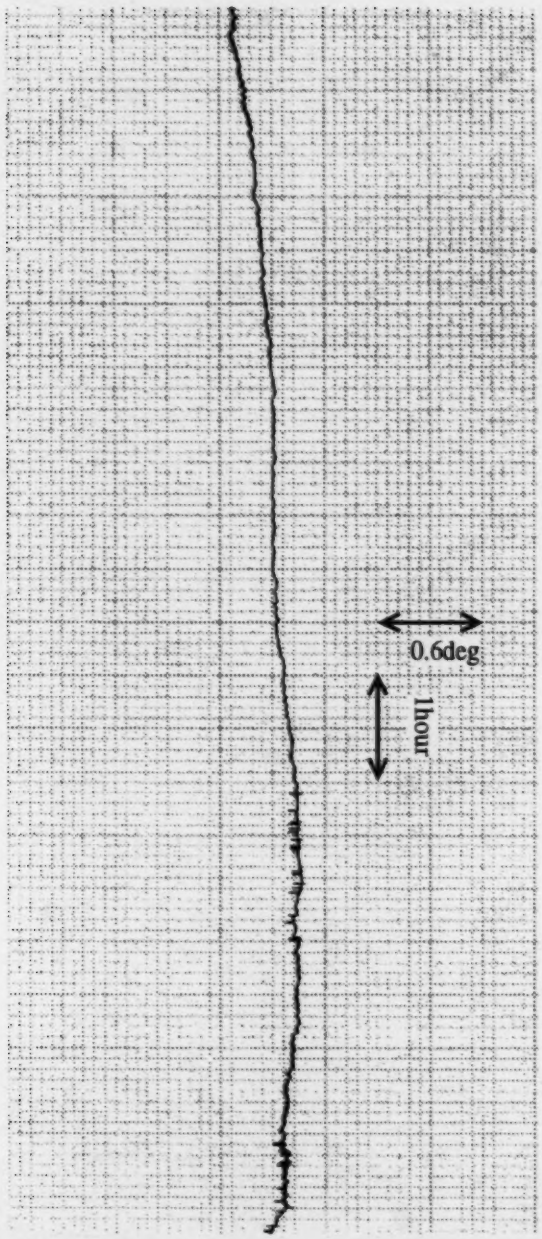

Figure 5.15: Phase stability measurement. This figure records the difference between the VCO phase and the phase of the input reference signal.

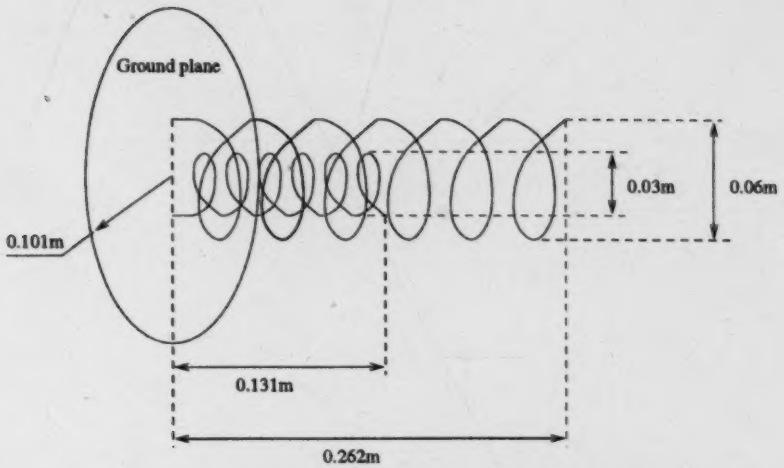

Figure 5.16: Coaxially-mounted dual helical feed.

helix at 3.15 GHz because the helix is not broadband enough [31]. There is, however, a way suggested by Holland (1981) of constructing two helical antennas coaxially, one inside the other, as shown in Figure 5.16 [26]. By doing so one can produce a feed covering a large band of frequencies. This idea was seen as the most suitable and the easiest to implement in this design. Holland (1981) also recommended placing the peripheral feed points of the two helices on opposite sides of the axis to reduce mutual coupling of the helices [26].

The performance of a helical antenna is well understood and generally design of such an antenna does not involve anything more than constructing a helix that satisfies the Kraus coil conditions [31]. The conditions specify the main dimensions of a helical antenna in terms of the centre wavelength. For example the conditions state that the circumference of the helix normalized by the wavelength, C_λ, should be $0.8 \leq C_\lambda \leq 1.2$ and the pitch angle, α, should be $12° \leq \alpha \leq 14°$. These two conditions and the knowledge of the desired gain or number of turns are enough for designing a helical antenna. The gain of the helical antenna is $D = 12C_\lambda^2 n S_\lambda$, where S_λ is the spacing between turns normalized by the wavelength and n is the number of turns.

The lower frequency helical antenna has to be centered at the frequency $\frac{1}{2}(1.35 + 1.8)$ GHz $= 1.575$ GHz. The circumference of the lower frequency helix was set to $C_\lambda = 1$ at this frequency. One should note that the helical antenna is still within the Kraus coil range at frequencies of 1.35 GHz and 1.8 GHz. The pitch angle was set to be 13°. Similarly, for the smaller helix operating at 3.15 GHz the circumference was set to 1 and the pitch angle was set to be 13°.

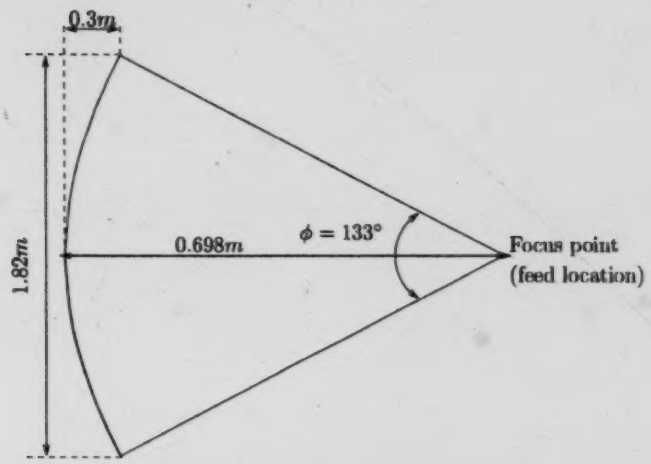

Figure 5.17: Reflector dimensions.

Another important parameter to consider when designing a feed for a paraboloidal antenna is the illumination of the reflector by the feed. It is obvious that some feeds may have very narrow beamwidth that will illuminate only the centre part of the paraboloid and give zero illumination of the edges, whereas another feed might have almost constant illumination of the whole paraboloid. There is a trade-off between beam efficiency and aperture efficiency as a function of feed pattern tapers. In practice, a taper of 10 dB to 20 dB at the edge is commonly used. The gain is usually maximum with a 10 dB edge illumination [26]. The dimensions of the paraboloidal reflector are shown in Figure 5.17. The number of turns required to achieve such illumination with the opening angle $\phi = 133°$ is [31]

$$n \approx \frac{8400}{C_\lambda^2 \phi^2 S_\lambda} = \frac{8400}{133^2 \times 0.23} = 2. \tag{5.16}$$

It was found, that for values of $n < 6$ the feed beam patterns were very irregular with very high sidelobes relative to the mainlobe. Therefore, both helices were constructed having six turns. It is unclear why the number of turns had to be larger than five.

The measure of the polarization performance is the axial ratio. For a perfectly circularly polarized antenna the axial ratio is one, whereas a linearly polarized antenna would have axial ratio of infinity. The axial ratio of a helical antenna having

n turns can be found from a simple relationship [31]

$$AR = \frac{2n+1}{2n}. \tag{5.17}$$

Therefore the larger the number of turns the more nearly circularly polarized the helix is. For $n = 6$, the axial ratio $AR \approx 1.08$. The dimensions of the feed are shown in Figure 5.16.

Each helix can have either right hand circular polarization (RHCP) or left hand circular polarization (LHCP). It was interesting to see if different polarization reduced the mutual coupling between the inner and outer helices. Table 5.2 summarizes the results of the measurement.

Frequency, GHz	Coupling of similarly polarized helices, dB	Coupling of oppositely polarized helices, dB
1.35	−15.0	−12.0
1.80	−9.6	−17.0
3.15	−9.6	−14.5

Table 5.2: Coupling between two helices. Helices were made of 10 AWG wire.

It appears that in the case of oppositely polarized helices the coupling was somewhat smaller; therefore, oppositely polarized helices were used in the feed.

Normally the thickness of the wire that the antenna is made of does not affect the antenna performance [31]. At first the helices were constructed with 10 AWG wire. They were tested in an anechoic chamber to investigate the beam patterns of the feed at the three frequencies of operation. It was found, however, that mutual coupling between the small helix and the large helix worsened the beam pattern at 1.8 GHz. Figure 5.18 shows the beam pattern of the feed at 1.8 GHz. It is clear that the sidelobe level would be very high at the edge of the reflector and there is a null in the feed beam illuminating the reflector.

The helices were then remade out of 16 AWG wire (thin wire). This improved the beam patterns. It was found that both helices had to be made from the thin wire for the better beam patterns. Figures 5.19, 5.20 and 5.21 show vertical and horizontal polarization beam patterns at the three frequencies. The thin wire also decreased coupling, as shown in Table 5.3.

When a helix is peripherally fed the terminal impedance of the helix is within 10% of $R = \frac{150}{\sqrt{C_\lambda}}$ [31]. One of the methods of matching this helix to a 50 Ω cable is to increase the conductor size close to the feed point [31]. This can be achieved by attaching a conductive strip extended for one half of the wavelength [30]. Kraus

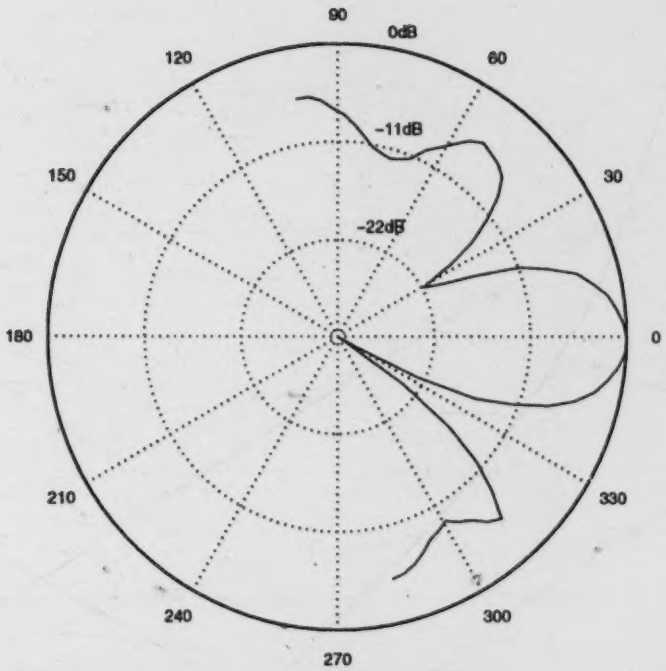

Figure 5.18: Beam pattern of the dual helix feed at 1.8 GHz when both helices are made of 10 AWG wire.

Frequency, GHz	Coupling, dB
1.35	−26.0
1.80	−29.0
3.15	−25.5

Table 5.3: Coupling between the two helices made from the thin wire.

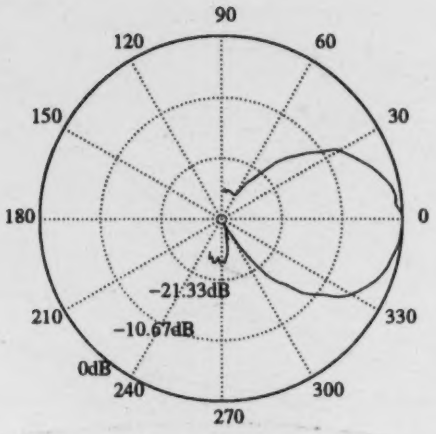

(a) $E(0°)$-field

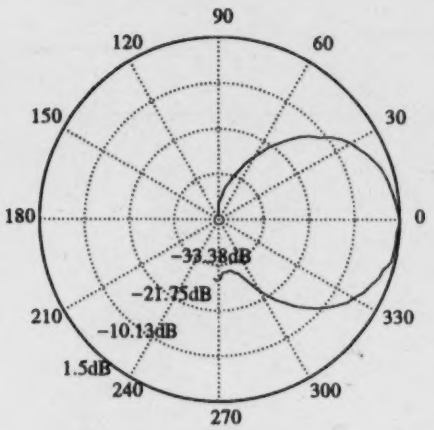

(b) $E(90°)$-field

Figure 5.19: Feed antenna patterns at 1.35 GHz normalized by $E(0°)$.

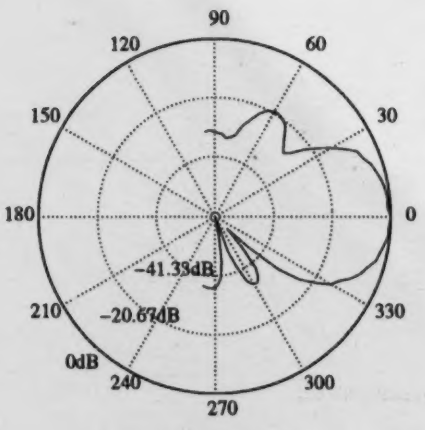

(a) $E(0°)$-field

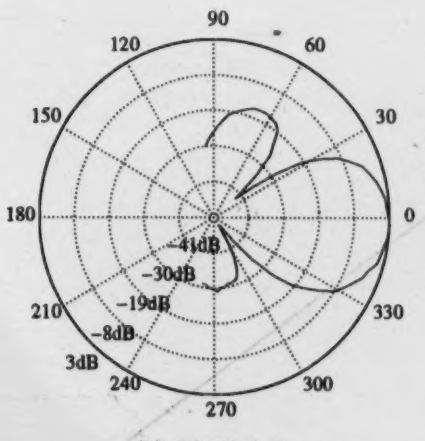

(b) $E(90°)$-field

Figure 5.20: Feed antenna patterns at 1.8 GHz normalized by $E(0°)$.

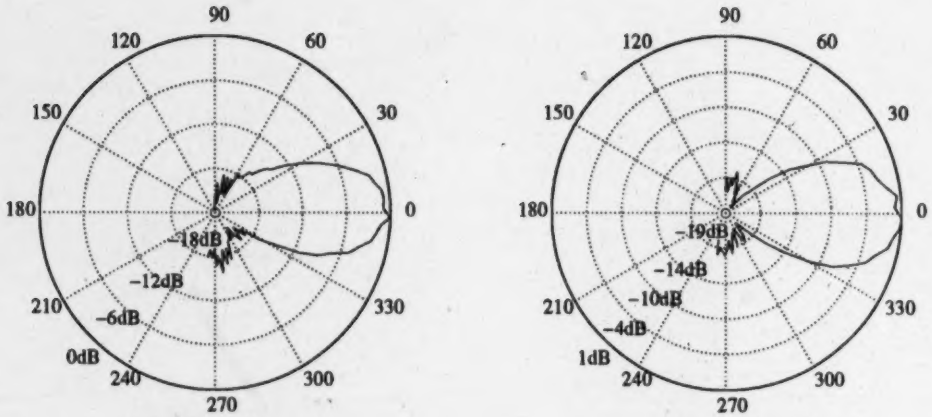

(a) $E(0°)$-field (b) $E(90°)$-field

Figure 5.21: Feed antenna patterns at 3.15 GHz normalized by $E(0°)$.

(1977) also suggested that if the conductor is positioned very close to the ground plane then the matching may not be needed at all [30]. That proved to be the case when the helices were constructed. The standing wave ratio (SWR) appeared to be less than 1.5 for the three frequencies. Figure 5.22 shows a plot of the feed SWR versus frequency. The network analyzer used to plot the SWR did not operate at frequencies higher than 3.0 GHz; therefore, it was not possible to measure the SWR at 3.15 GHz but by inspecting the behaviour of the SWR at frequencies close to 3.15 GHz, it was concluded that the SWR will not be greater than 1.5 at 3.15 GHz.

5.4.2.2 Paraboloidal antenna performance measurement

Once the feed was built and placed at the approximate location of the focus point of the paraboloid, the actual focal length was determined by using the Sun as a signal source and sliding the feed up and down along the focal axis until maximum power was received at the three frequencies. It appeared that, although the focal length of the paraboloid of 0.679 m was given in the antenna specifications, it was not accurate. The actual focal length is 0.698 m and the angle subtended by the rim at the focal point is 133° as shown in Figure 5.17. This focal length was used in Section 5.4.2.1. Figure 5.23 shows the paraboloidal antenna and its feed.

The Sun was also used as a source for the measurement of antenna patterns. The paraboloidal antenna was pointed to the declination of the Sun. As the Sun drifted by, the received power was plotted on a chart recorder. Figure 5.24 shows

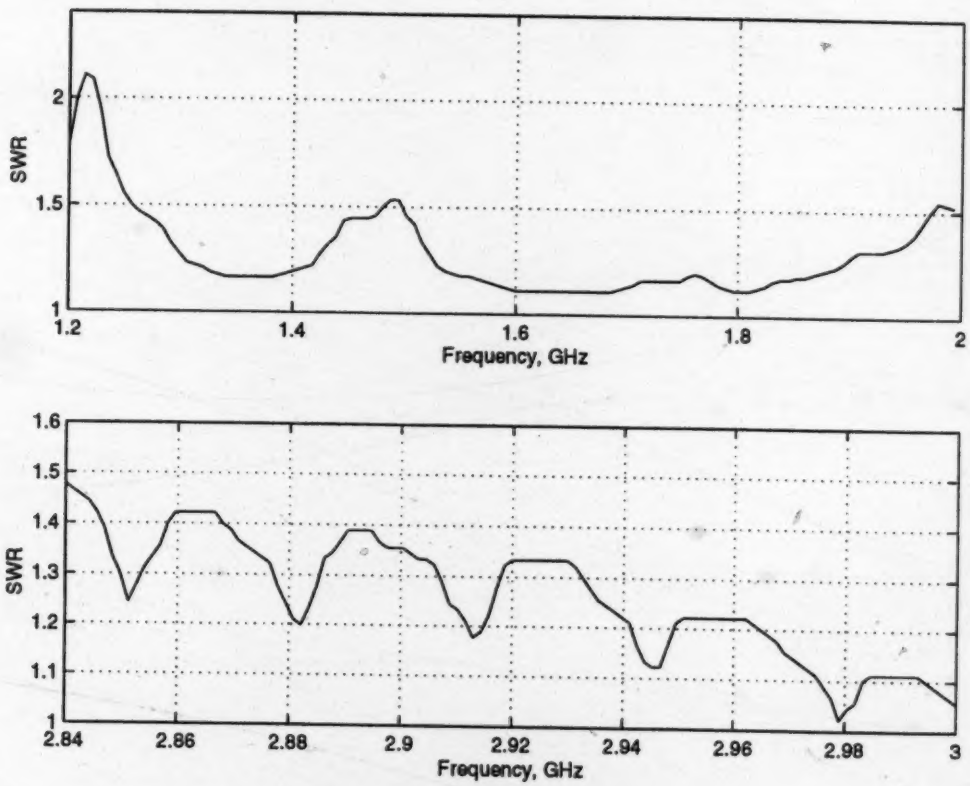

Figure 5.22: Measured feed SWR.

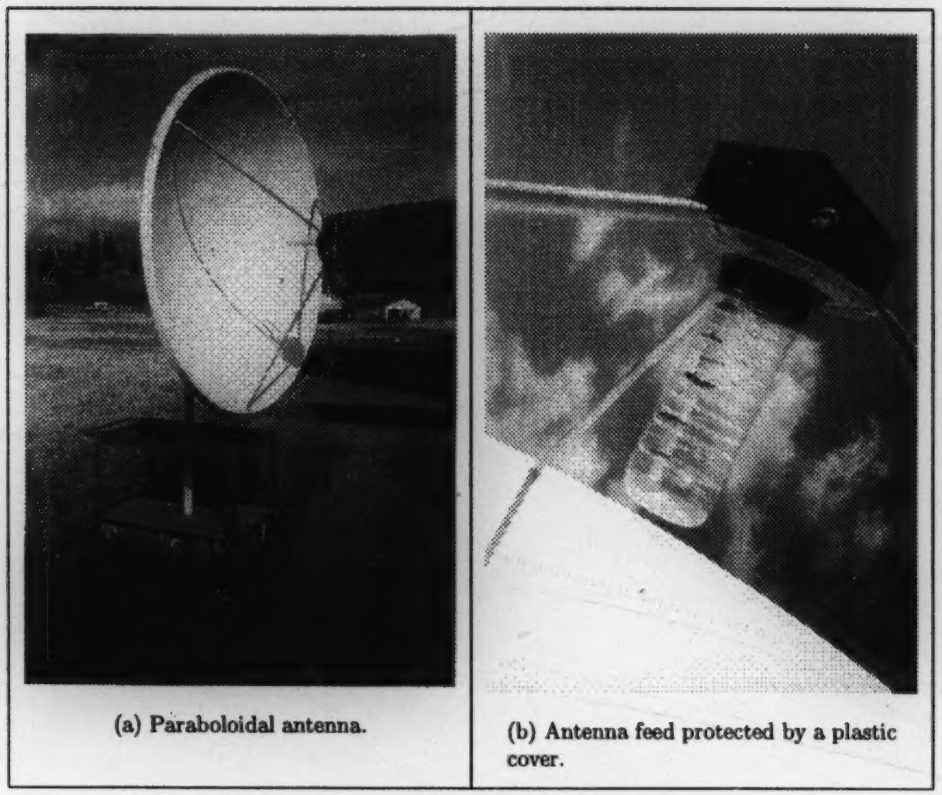

(a) Paraboloidal antenna.

(b) Antenna feed protected by a plastic cover.

Figure 5.23: Paraboloidal antenna and its feed.

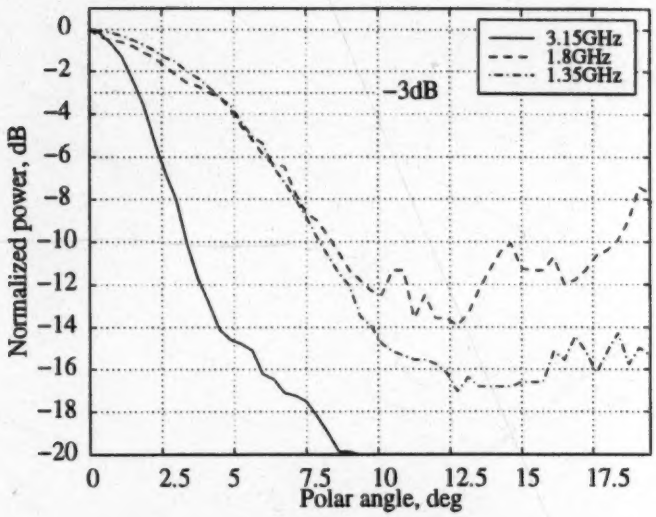

Figure 5.24: Paraboloidal antenna beam patterns recorded by solar drift scans.

the paraboloidal antenna beam patterns recorded. Although this method is very convenient for plotting antenna patterns it was found that reflections from nearby buildings affected the sidelobes considerably. There was also some interference from satellites. The shadow of the feed was used to determine the pointing. It is expected that the pointing might not have been precise. Therefore the solar drift measurements were only used to get an idea about what the main beam looks like. The HPBWs of the antenna at the three frequencies are summarized in Table 5.4.

Frequency	Theoretical HPBW (no taper)	Measured HPBW
1.35 GHz	7.08°	8.7°
1.80 GHz	5.31°	7.8°
3.15 GHz	3.04°	3.3°

Table 5.4: HPBWs of the paraboloidal antenna at the three frequencies.

The aperture efficiency of the antenna at the three operating frequencies was measured by injecting a noise signal of 373 K immediately before the first amplifier stage and using the flux density of the Sun. The antenna temperature due to the Sun, T_s, can be calibrated by measuring the output power, P_s, of the antenna pointed at the Sun and the output power, P_n, due to the noise injection as $T_s = T_n \frac{P_s}{P_n}$. Knowing the solar flux density one can find the effective area of the paraboloid as follows:

$$A_{eff} = \frac{2kT_s}{S \times 10^{-22}}, \tag{5.18}$$

where k is Boltzmann's constant, T_s is the apparent Sun temperature and S is the solar flux density in solar flux units, sfu[1]. The multiplier 2 appears in the equation simply because the antenna can only receive half of the total power from the Sun due to the random polarization properties of the signals. Figure 5.25 shows the solar flux at the day of the measurements. The data were taken from NOAA Solar-Geophysical Data [41]. Using linear interpolation, the solar flux density values for

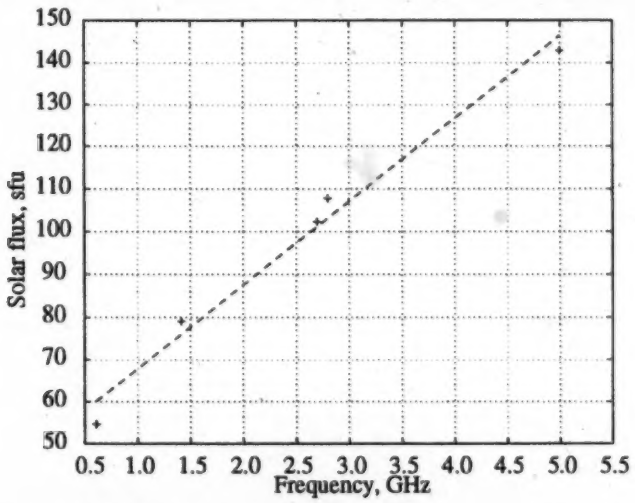

Figure 5.25: Solar flux density values (sfu), September 28, 1998 [41].

1.35 GHz, 1.8 GHz and 3.15 GHz were obtained.

Table 5.5 summarizes the results of antenna calibration, the effective area of the paraboloidal antenna and its aperture efficiency.

Since the antennas are not a very critical part of this project it was decided not to improve the feeds any longer. The feeds constructed perform well enough to be used in this study.

5.4.3 LO prototype testing

The implementation of the LO prototype had to allow for easy testing. The main concern for the test was the presence of the time delay, which was essential for a

[1] 1 sfu = 10^{-22} $Wm^{-2}Hz^{-1}$

Frequency, GHz	Solar flux density, sfu	Output power		Antenna temperature due to the Sun, K	Antenna effective area, m^2	Antenna aperture efficiency, %	Antenna gain, dBi
		P_s dBm	P_n dBm				
1.35	74.7	−6.5	−6.4	365	1.35	51.4	25
1.80	83.5	−10.4	−9.2	283	0.94	35.8	26
3.15	110.1	−8.3	−8.6	400	1.00	38.2	31

Table 5.5: Paraboloidal antenna efficiencies and effective areas.

proper test. It was also essential to compare phases of the reference signal at the input to the LO system and the signal delivered at the output.

The prototype LO system was implemented directly according to Figure 5.2. The circuit diagrams of the ground unit and the remote unit are shown in Appendix A. Figures 5.26 and 5.27 show assembled units. Figures 5.28 and 5.29 show two test

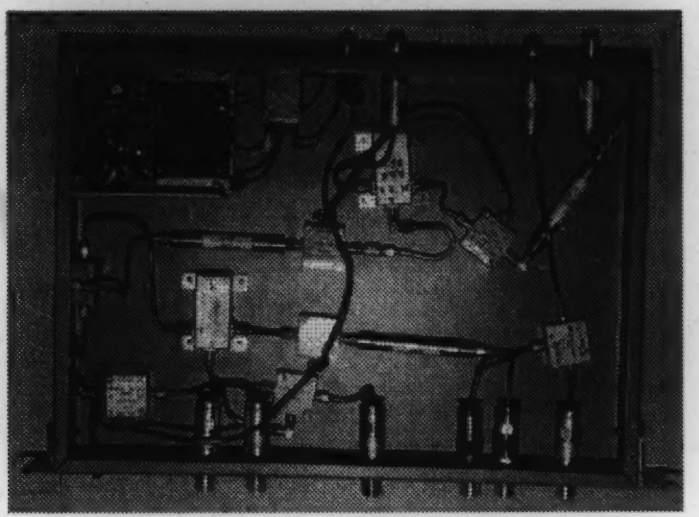

Figure 5.26: Assembled ground unit.

arrangements that were used.

5.4.3.1 Link budget for 800 metre test

Figure 5.28 displays the test configuration and shows the noise figures of the system components involved. The distance between the two antennas in the test was 300 m as shown in Figure 5.28. According to Equation 5.1 the free space attenuation of 3.15 GHz, 1.8 GHz and 1.35 GHz is 92 dB, 87 dB and 86 dB respectively. The 3.15 GHz signal and the 1.35 GHz and 1.8 GHz signals must share the same buried cable since the transmission medium for the signals must be the same; otherwise the LO cannot successfully remove the effects of distance variations. Two problems arose when the signals were combined on the same cable. First, only one combiner was available operating in the right frequency range; a directional coupler with 10 dB attenuation at the coupled port was used instead of the second combiner. Second, the leakage between signals in the directional coupler and the combiner introduced additional problems due to this configuration.

The cable connecting the antennas to the control building is long and at frequencies as high as 1 GHz – 3 GHz is very lossy. The measured attenuation of the buried

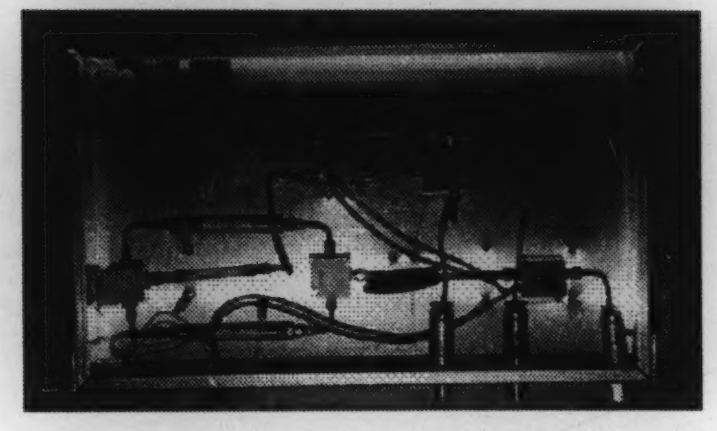

Figure 5.27: Assembled remote unit.

cable connecting the remote unit and the remote antenna is 110 dB at 3.15 GHz, 65 dB at 1.8 GHz, and 60 dB at 1.35 GHz. Therefore, it was necessary to build additional amplifier stages to restore the signal power and improve the noise figure. The remote antenna had a 30 dB amplifier at the receiving low frequency band helix. A 45 dB amplifier was added at the input to the remote antenna increasing the gain of the 1.35 GHz and 1.8 GHz signals to 75 dB and a 45 dB amplifier was inserted for the 3.15 GHz signal arriving from the control building through the buried cable. The feed of the ground antenna had a 12 dB amplifier at the receiving high frequency band helix. Two 30 dB amplifiers were inserted on both sides of the 50 m cable connecting the ground unit antenna and the ground unit and carrying the 3.15 GHz signal.

The link budget is calculated according to Equation 5.6. The noise figures for lossy components equal their attenuation. According to Equations 5.3 and 5.5 the system noise figure of the remote unit assuming a physical antenna temperature of 300 K and the noise temperature due to the 50 m cable of $\frac{290(10^1-1)}{10^{3.6}} = 0.66$ is calculated to be $NF_{ru} = 166$ (see Table 5.6).

Thus,

$$T_{ru} = (NF_{ru} - 1)290 = 47850 \text{ K}. \tag{5.19}$$

According to Equation 5.6, the SNR of the input to the remote unit with the bandwidth of 95 MHz is calculated in Table 5.7 as $SNR_{ru} = 35.6$ dB. 95 MHz is the bandwidth of the narrowest filter in the remote unit.

For the 3.15 GHz signal received by the ground antenna the link budget is calculated in the same fashion. First of all the noise figure of the signal that arrives at the remote antenna through the buried cable is found in Table 5.8 to be $NF_{ra} = 794 \times 10^9$.

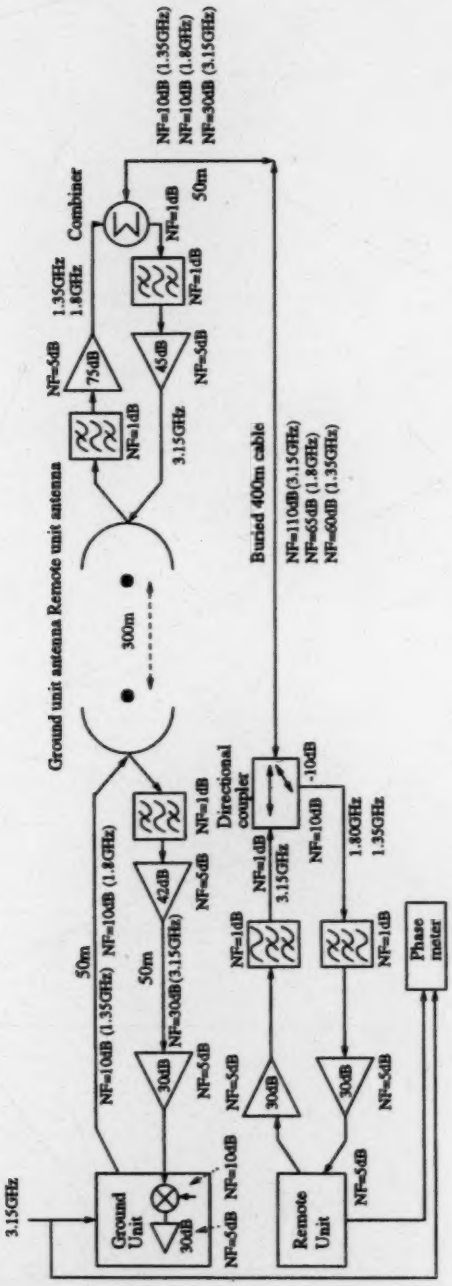

Figure 5.28: LO prototype (800 m test).

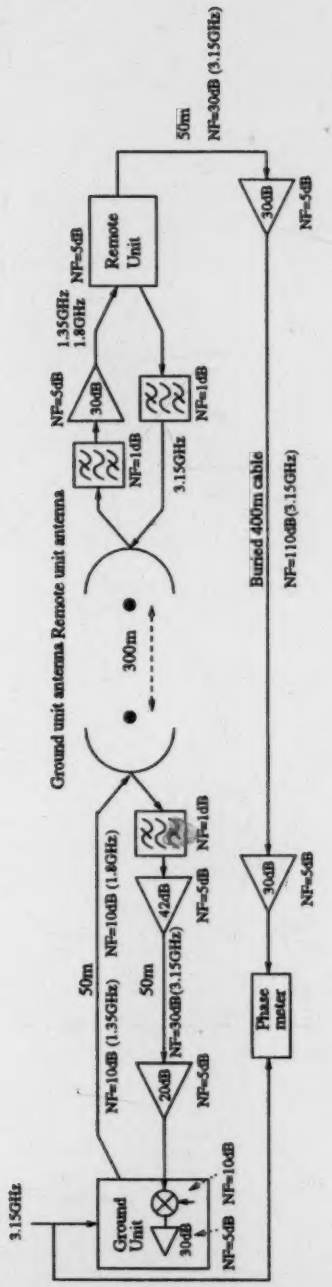

Figure 5.29: LO prototype (350 m test).

$NF_{ru} =$	$\frac{300+0.66}{290} + 1$	Remote antenna NF
	$+10^{0.1}$	Bandpass filter NF
	$+10^{0.5} \times 10^{0.1}$ ..	75 dB amplifier NF
	$+\frac{10^{0.1}-1}{10^{7.5}}10^{0.6}$ ...	Combiner NF
	$+\frac{10^{7.5}-1}{10^{7.5}}10^{0.6}$ ...	50 m cable and 400 m cable NF
	$+\frac{10^{1}-1}{10^{7.5}}10^{8.1}$	Directional coupler NF
	$+\frac{10^{0.1}-1}{10^{7.5}}10^{9.1}$ ...	Lowpass filter NF
	$+\frac{10^{0.5}-1}{10^{7.5}}10^{9.2}$ ...	30 dB amplifier NF
	$+\frac{10^{0.5}-1}{10^{10.5}}10^{9.2}$ ...	Remote unit NF
	+.....	Other (negligible)
	= 166	Total NF

Table 5.6: The system noise figure of the remote unit (800 m test).

SNR_{ru}(dB)	= 25	Ground antenna gain at 1.35 GHz
	−30	Transmitted power relative to 1 W
	+25	Remote antenna gain at 1.35 GHz
	−86	Free-space loss at 1.8 GHz
	+228.6	Boltzmann's constant (dB)
	−80	Bandwidth (dB)
	−47	Noise temperature (T_{ru}(dB))
	= 35.6	Total(dB)

Table 5.7: SNR of the input to the remote unit (800 m test).

Thus, the noise temperature received by the ground antenna is

NF_{ra}	$= 166$	NF_{ru}
	$+10^{0.5}$	30 dB amplifier NF
	$+\frac{10^{0.1}-1}{10^3}$	Highpass filter NF
	$+\frac{10^{0.1}-1}{10^3}10^{0.1}$ ...	Directional coupler, NF
	$+\frac{10^{14}-1}{10^3}10^{0.2}$ ...	400 m cable and 50 m cable NF
	$+\frac{10^{0.1}-1}{10^3}10^{14.2}$ ..	Combiner NF
	$+\frac{10^{0.1}-1}{10^3}10^{14.3}$ ..	Bandpass filter NF
	$+\frac{10^{0.5}-1}{10^3}10^{14.4}$ ..	45 dB amplifier NF
	$+$	Other (negligible)
	$= 794 \times 10^9$	Total

Table 5.8: Noise figure of the signal emerging from buried cable (800 m test).

$$T_{ga} = 300 + \frac{794 \times 10^9}{10^{(9.2-3.1-3.1)}} = 794 \times 10^6 \text{ K}, \tag{5.20}$$

where the loss in the transmission medium is 92 dB and the gain of the antennas at 3.15 GHz is 31 dB. The system noise figure of the ground unit is $NF_{gu} = 2.7 \times 10^6$ as calculated in Table 5.9.

The noise temperature at the ground unit is then

$$T_{gu} = (NF_{gu} - 1)290 = 794 \times 10^6 \text{ K}. \tag{5.21}$$

The SNR of the input to the ground unit with the phase-halving PLL noise bandwidth of 10.25 kHz is calculated in Table 5.10 as -45.4 dB. This causes a problem since the minimum SNR required by the PLL to lock was measured to be -15 dB. Thus this test was not possible.

5.4.3.2 Link budget for 350 metre test

The link budget is calculated from Equation 5.6. According to Equations 5.3 and 5.5, the system noise figure of the remote unit assuming a physical antenna temperature

$NF_{gu} =$	$\frac{794\times10^6}{290}+1$	Ground antenna NF,
	$+10^{0.1}$	Bandpass filter NF
	$+10^{0.5}\times10^{0.1}$ ..	42 dB amplifier NF
	$+\frac{10^3-1}{10^{4.2}}10^{0.6}$	50 m cable NF
	$+\frac{10^{0.5}-1}{10^{4.2}}10^{3.6}$ ...	30 dB amplifier NF
	$+\frac{10^1-1}{10^{7.2}}10^{3.6}$	Ground unit input mixer NF
	$+\frac{10^{0.5}-1}{10^{7.2}}10^{4.6}$ ...	30 dB amplifier NF
	+.....	Other (negligible)
	$=2.7\times10^6$	Total

Table 5.9: The system noise figure of the ground unit (800 m test).

SNR_{gu}(dB)	= 31	Ground antenna gain at 3.15 GHz
	−115	Transmitted power relative to 1 W
	+31	Remote antenna gain at 1.35 GHz
	−92	Free-space loss at 1.8 GHz
	+228.6	Boltzmann's constant (dB)
	−40	Bandwidth (dB)
	−89	Noise temperature (T_{ru}(dB))
	= −45.4	Total(dB)

Table 5.10: SNR at the input to the ground unit (800 m test).

of 300 K and the noise temperature due to noise acquired in the 50 m cable of $\frac{290(10^{1}-1)}{10^{3.6}} = 0.66$ is calculated in Table 5.11 as $NF_{ru} = 7.3$.

$NF_{ru} =$	$\frac{300+0.66}{290} + 1$	Remote antenna NF
	$+10^{0.1}$	Bandpass filter NF
	$+10^{0.5} \times 10^{0.1}$ ..	30 dB amplifier NF
	$+\frac{10^{0.5}-1}{10^{3}}10^{0.6}$ ...	Combiner NF
	+.....	Other (negligible)
	= 7.3	Total NF

Table 5.11: The system noise figure of the remote unit (350 m test).

Thus,

$$T_{ru} = (NF_{ru} - 1)290 = 1827 \text{ K}. \tag{5.22}$$

According to Equation 5.6, the SNR of the input to the remote unit with the bandwidth of 95 MHz is shown in Table 5.12 and is $SNR_{ru} = 49.6$ dB. 95 MHz is the bandwidth of the narrowest filter in the remote unit.

SNR_{ru}(dB)	= 25	Ground antenna gain at 1.35 GHz
	−30	Transmitted power relative to 1 W
	+25	Remote antenna gain at 1.35 GHz
	−86	Free-space loss at 1.8 GHz
	+228.6	Boltzmann's constant (dB)
	−80	Bandwidth (dB)
	−33	Noise temperature (T_{ru}(dB))
	= 49.6	Total(dB)

Table 5.12: SNR of the input to the remote unit (350 m test).

For the 3.15 GHz signal received by the ground antenna the link budget is calculated in the same fashion. First of all the noise figure of the signal that arrives at the remote antenna is found in Table 5.13 to be $NF_{ra} = 8.6$.

Thus, the noise temperature received by the ground antenna is

$$T_{ga} = 300 + \frac{290(8.6-1)}{10^{(9.2-3.1-3.1)}} = 302 \text{ K}, \tag{5.23}$$

NF_{ra}	$= 7.3$	NF_{ru}
	$+10^{0.1}$	Bandpass filter
	$+$	Other (negligible)
	$= 8.6$	Total

Table 5.13: Noise figure of the signal arriving at the remote antenna cable (350 m test).

where the loss in the transmission medium is 92 dB and the gain of the antennas at 3.15 GHz is 31 dB. The system noise figure of the ground unit is shown in Table 5.14 as $NF_{gu} = 8.2$. The noise temperature at the ground unit is then

$NF_{gu} =$	$\frac{302}{290} + 1$	Ground antenna NF
	$+10^{0.1}$	Bandpass filter NF
	$+10^{0.5} \times 10^{0.1}$ ..	42 dB amplifier NF
	$+\frac{10^3-1}{10^{4.2}}10^{0.6}$	50 m cable NF
	$+\frac{10^{0.5}-1}{10^{4.2}}10^{3.6}$ ...	20 dB amplifier NF
	$+\frac{10^1-1}{10^{6.2}}10^{3.6}$	Ground unit input mixer NF
	$+\frac{10^{0.5}-1}{10^{6.2}}10^{4.6}$ ...	30 dB amplifier NF
	$+$	Other (negligible)
	$= 8.2$	Total

Table 5.14: The system noise figure of the ground unit (350 m test).

$$T_{gu} = (NF_{gu} - 1)290 = 2088 \text{ K}. \tag{5.24}$$

The SNR at the input to the ground unit with the phase-halving PLL noise bandwidth of 10.25 kHz is very large as calculated in Table 5.15. This SNR should be expected in the real LO system employed in the LAR telescope.

SNR_{gu}(dB)	= 31	Ground antenna gain at 3.15 GHz
	−17	Transmitted power relative to 1 W
	+31	Remote antenna gain at 1.35 GHz
	−92	Free-space loss at 1.8 GHz
	+228.6	Boltzmann's constant (dB)
	−40	Bandwidth (dB)
	−33	Noise temperature (T_{ru}(dB))
	= 108.6	Total(dB)

Table 5.15: SNR at the input to the ground unit (350 m test).

5.5 LO system performance

The LO system prototype was assembled according to the design described in Section 5.4. Figure 5.30 shows the assembled LO system.

Figure 5.30: Assembled LO system. (Two racks right of centre.)

5.5.1 LO prototype test without time delay

The system performance was examined to investigate if the design and simulations were valid and could be used for the design of the LO system for the LAR. The uplink and downlink signals were combined on a single cable whose length was slowly changed by using an adjustable airline driven by an electric motor. The length was

altered monotonically by 0.47 m at the speed of 3 mm/s. The phase of the 3.15 GHz signal delivered to the remote unit was compared with the phase of the 3.15 GHz reference signal by downconverting the signals with a 3 GHz reference signal and measuring their relative phases with an HP8405A vector-voltmeter. The output of the HP8405A was displayed on a chart recorder.

5.5.1.1 Improvement of the LO performance

The main difference, other than the time delay, between the prototype LO system and the final LO system was that the uplink and downlink used the same coaxial cable. This introduced coupling between the two channels and produced spurious signals that caused phase errors in the LO output.

At first the system as it was assembled produced output having $38^{\circ}_{\text{p-p}}$ phase error as shown in Figure 5.32(a). There are a number of reasons for the errors. The most common cause of the errors is mismatches between cables and components. An attenuator labelled "Attenuator A" in Figure A.2 was inserted to improve matching. The result was reduced phase variations as shown in Figure 5.32(b).

Another problem with the original design was the mixer labelled as "MIXER A" in Figure A.2. The mixer is a non-linear device that produces not only the expected 1.35 GHz but also two spurious 1.35 GHz signals due to squaring of both 675 MHz input signals. The spurious signals were only 10 dB below the desired signal. The spurious signals produce phase errors that are very significant, as demonstrated in Section 5.2.2. Therefore the mixer was replaced with the "mixer assembly" shown in Figure 5.31. The circuit diagram of the "mixer assembly" is shown in Figure

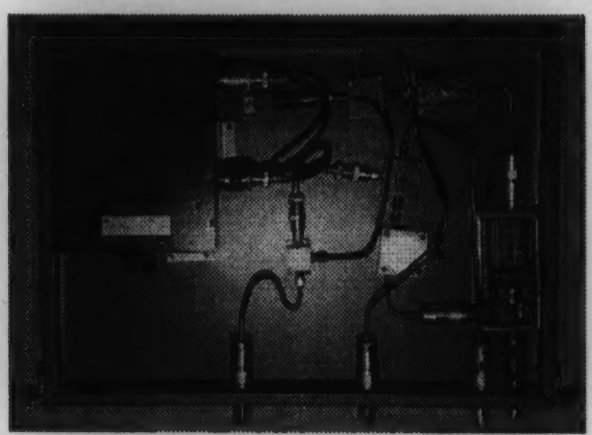

Figure 5.31: Photograph of the "mixer assembly" .

C.1. Initially, however, the "mixer assembly" did not have the two isolators. The

LO performance is shown in Figure 5.32(c). The matching was further improved by inserting isolators at the input and the output of the ground unit to achieve the phase tracking performance shown in Figure 5.32(d).

The "mixer assembly" consists of a local oscillator that is used to spread signals away from 1.35 GHz for easy filtering. Nevertheless, there was still enough signal leakage through the directional coupler to produce phase errors. That problem was corrected by inserting isolators on both outputs of the directional coupler. Figure 5.32(e) shows the change in the LO performance.

Finally, the local oscillator signal used in the "mixer assembly" was locked to a reference signal (see Figure C.1). This appeared to make a difference even though it should be possible to build this system with unlocked local oscillator and still have it perform satisfactorily. However, locking the oscillator appeared to be much easier than making the lengths of the lines identical. Figure 5.32(f) shows the performance of the LO system after all the improvements were put in place.

At this time, it has been decided not to improve the LO any further. The reason is that LO systems like this are being used at the present time at a number of telescopes. It is known that the performance of the prototype can be improved to match the performance of those systems. However, the hunt for obscure mismatches is very time consuming. If it could be shown that the system functioned satisfactorily when time delay was introduced, then it most certainly can be improved by improving the performance of the system without the time delay.

5.5.2 100 metre test

A 100 m cable was inserted between the ground unit and the remote unit. The cable introduced a time delay for the first time in the system.

There are several problems with combining the signals on one cable, especially when the cable is very lossy. The main problem arises from coupling between very strong signals entering the combining network and the weak signals emerging from the cable. The 100 m cable has 60 dB attenuation at 3.15 GHz. Therefore strong signals entering the cable can saturate amplifiers necessary to boost the emerging signals if there is some leakage between the signals. Very good filtering is required to ensure that the amplifiers are not saturated. A number of filters were constructed specifically to combat this problem.

Two main performance issues that were tested are the LO phase stability with cable length change and the dynamic response of the LO system.

Figure 5.33 shows the phase of the LO output signal as the length of the cable was varied monotonically by 0.47 m. The figure shows that phase variations were 7°_{p-p} which is comparable to the performance of the system without time delay.

To measure the step response of the system properly, the cable length must

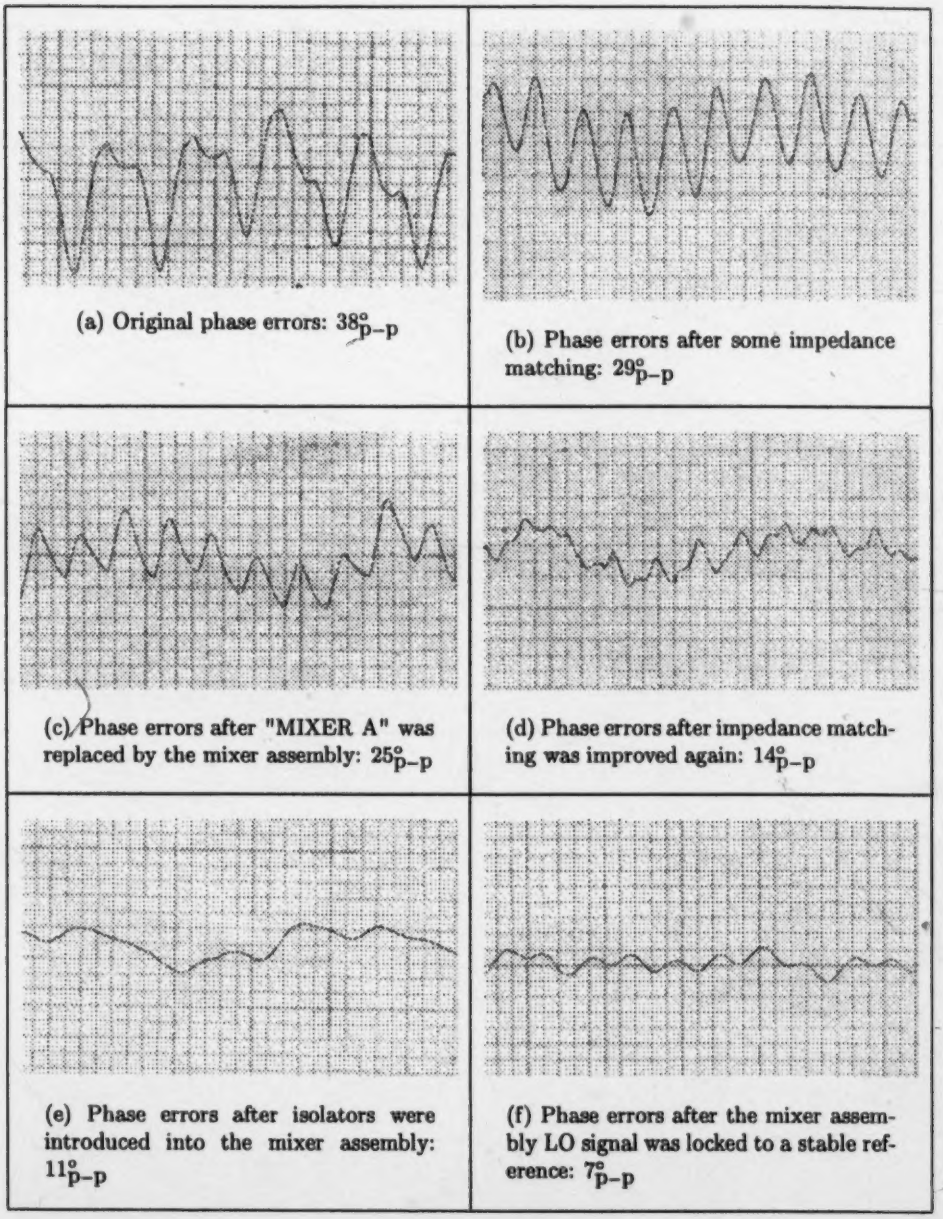

(a) Original phase errors: 38°_{p-p}

(b) Phase errors after some impedance matching: 29°_{p-p}

(c) Phase errors after "MIXER A" was replaced by the mixer assembly: 25°_{p-p}

(d) Phase errors after impedance matching was improved again: 14°_{p-p}

(e) Phase errors after isolators were introduced into the mixer assembly: 11°_{p-p}

(f) Phase errors after the mixer assembly LO signal was locked to a stable reference: 7°_{p-p}

Figure 5.32: Improvement of the LO performance. Horizontal scale from beginning of each curve to the end in each figure represents a change of 0.47 m in the path length between the ground and the remote units. The vertical scale of 3.6 deg/div represents the phase variations in the LO output.

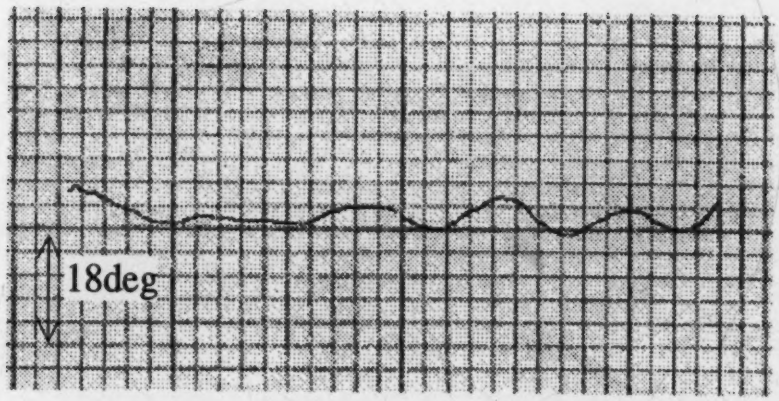

Figure 5.33: Phase of the LO output signal as the path length changes (100 m test). The figure represents phase variations in the output of the LO system as the path length between the ground and the remote units changes by 0.47 m.

be changed instantaneously and the phase variations at the LO output must be recorded. The step response can be measured by phase modulating the 3.15 GHz signal with a square wave and comparing the phase of the modulated signal delivered by the LO system with that of an independent 3.15 GHz source. In this case, however, the time delay does not change. Unfortunately, these two tests were not possible. The first test required some device to change the cable length abruptly and to record the change for comparison with the results of the phase measurements. The other test required a second 3.15 GHz signal generator which was not available.

Instead a lock acquisition test was performed. A locked system was disturbed by frequency-shifting the 675 MHz reference signal. The test did not measure the step response of the LO system, but it did provide an insight into system behaviour. The frequency-shifting of the 675 MHz reference signal was accomplished by frequency modulating the signal with a square wave. Since the 1.35 GHz reference signal was derived by doubling the 675 MHz signal, the 1.35 GHz was also frequency modulated by the same square wave. The output of the loop filter in the phase-halving PLL was measured. This output can be considered as an average measure of the phase error. Figure 5.34 displays the block diagram of the control system measured in the test. Simplifying the block diagram, the transfer function becomes:

$$\frac{C(s)}{R(s)} = \frac{K_m K_d \frac{F(s)}{s}\left(1 + e^{-2sT_d}\right)}{1 + 2K_o K_d \frac{F(s)}{s} e^{-2sT_d}}. \tag{5.25}$$

The "locking response" measured in this test is not identical to the step response

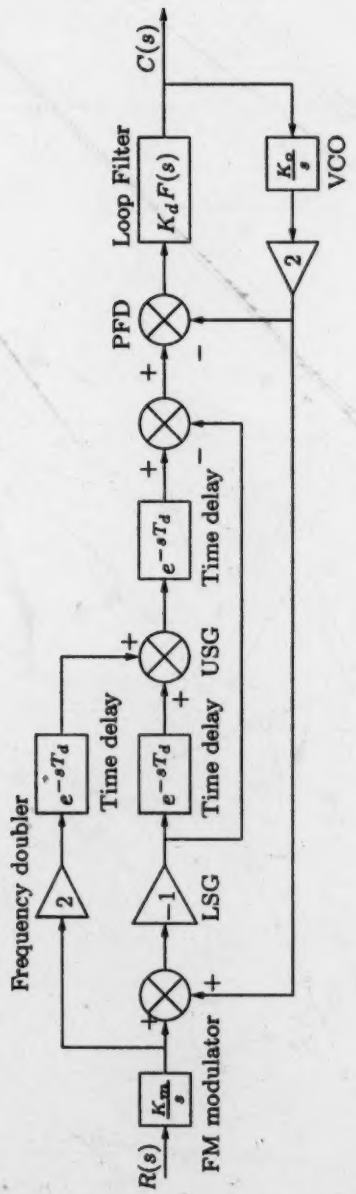

Figure 5.34: Block diagram of the lock acquisition test (100 m test).

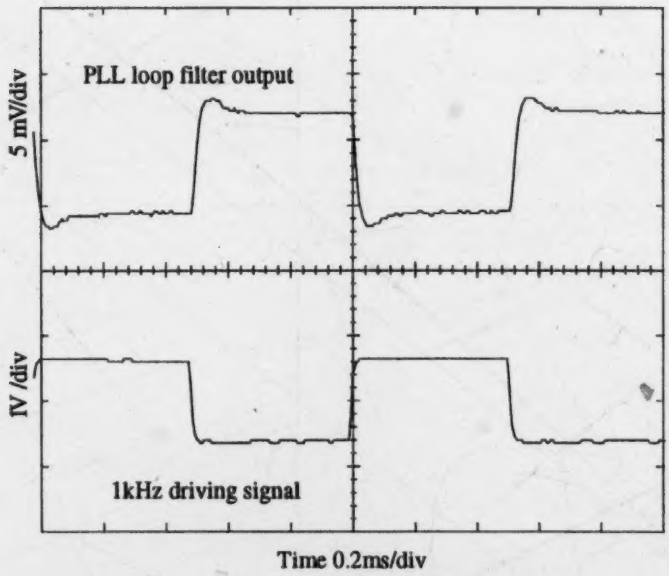

Figure 5.35: "Locking response" of the phase-halving PLL loop filter output to a square wave frequency-modulation of the 675 MHz reference signal (100 m test).

of the LO system. Figure 5.35 shows the measured "locking response".

5.5.3 350 metre test

The antennas were positioned 300 m apart. Two 50 m cables connected the ground unit antenna with the ground unit. One cable carried the 3.15 GHz signal, the other cable carried the 1.35 GHz signal and the 1.8 GHz signal. The overall distance was 350 m and the time delay was $\frac{350}{3\times10^8} = 1.17\,\mu s$ (see Figure 5.29).

This configuration is very similar to the proposed configuration of the LO system in the LAR. A number of critical measurements were made to analyze the performance of the LO prototype.

Phase stability: The phase delivered by the LO system was measured and plotted with a chart recorder. Figure 5.36 shows that the phase varied by 0.072°rms over 10 min. The cable carrying the LO output signal back to the ground

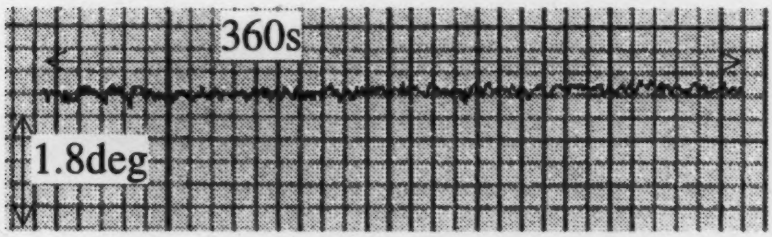

Figure 5.36: LO system phase stability test (350 m test). The phase of the LO output signal was compared with the phase of the 3.15 GHz reference signal.

unit, the remote unit, and the amplifiers shown in Figure 5.29 were not in a temperature controlled environment which caused the phase to drift slightly. The effects of temperature variations were also noticeable as amplifier gains changed with time.

The ground unit antenna was then moved cyclically forward and back to measure whether the LO system can cope with the distance variations. Figure 5.37 shows the performance of the LO system. The antenna was moved forward and back by 0.4 m with an average speed of 0.14 m/s. The phase varied by less than 3.6°_{p-p} which suggested that some of the problems that were present when a cable connected the ground unit and the remote unit had disappeared. A similar experiment was performed with the open loop LO system. The phase varied by 360°_{p-p} when the antenna was moved. This is shown in Figure 5.38.

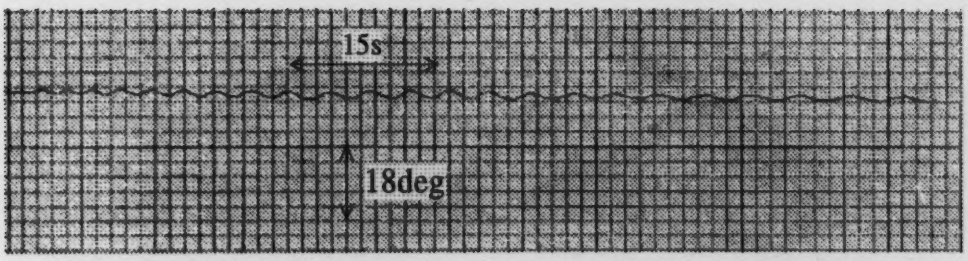

Figure 5.37: Phase stability of the LO system as the distance changed (350 m test). The ground antenna was moved periodically back and forth by 0.4 m with an average speed of 0.14 m/s. The phase of the LO output signal was compared with the phase of the 3.15 GHz reference signal.

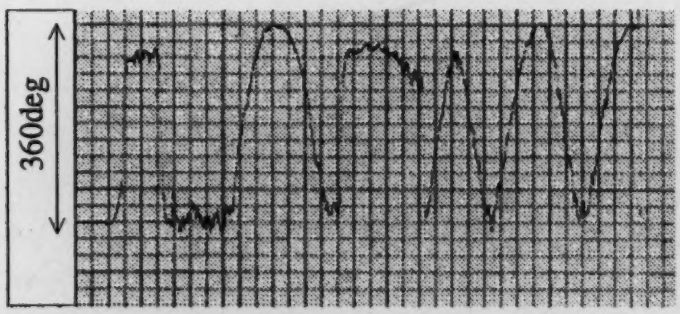

Figure 5.38: Open loop performance of the LO system (350 m test). The ground antenna was moved back and forth a few times.

Lock-in time: An electrically controlled switch was introduced at the output of the VCO. The switch was driven with a square wave signal. The switch broke and restored the phase-halving PLL loop so that the lock-in time could be measured. The phase-halving PLL loop filter output and the driving square wave are shown in Figure 5.39. From Figure 5.39 the lock-in time is measured as t_{lock} = 9.5 ms. MATLAB/SIMULINK simulations have shown that the

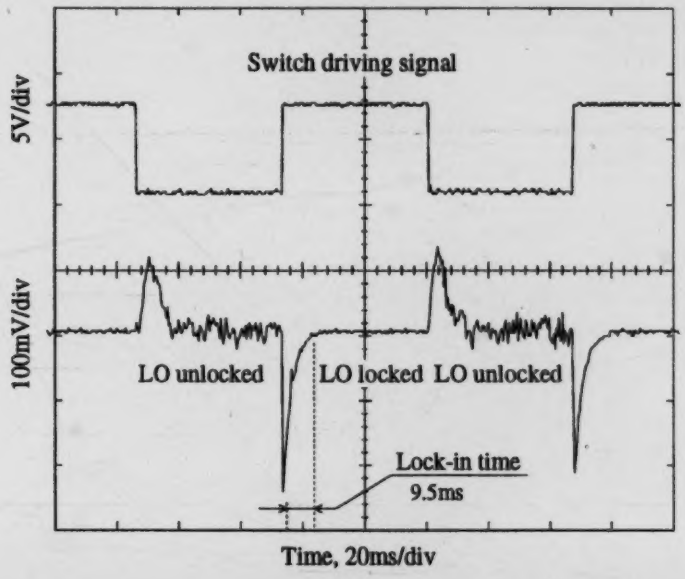

Figure 5.39: Lock-in time measurements. An electrically controlled switch, driven by a square wave signal and introduced at the output of the VCO, broke and restored the phase-halving PLL loop so that the lock-in time could be measured at the output of the phase-halving PLL loop filter. (350 m test)

lock-in time is highly dependent on the behaviour of the VCO. The further the VCO output drifts from the frequency of lock, the longer it might take for the loop to regain lock. This is especially true if the output of the VCO drifts past the pull-in range of the PLL.

Antenna pointing: Good pointing of the antennas is very important for the performance of the LO system. With the HPBW of 3° at 3.15 GHz the pointing of the antennas had to be very accurate to perform the pointing measurements. After the antennas were pointed directly at each other, the ground unit antenna was tilted down so that the power received by the antenna at 3.15 GHz

decreased by 3 dB. The antenna was then tilted up very slowly until the gain reached its peak and then decreased by 3 dB again. During this experiment, the signal power and the phase of the LO output were recorded. Figure 5.40 shows how the LO output phase varied as the elevation of the ground antenna changed.

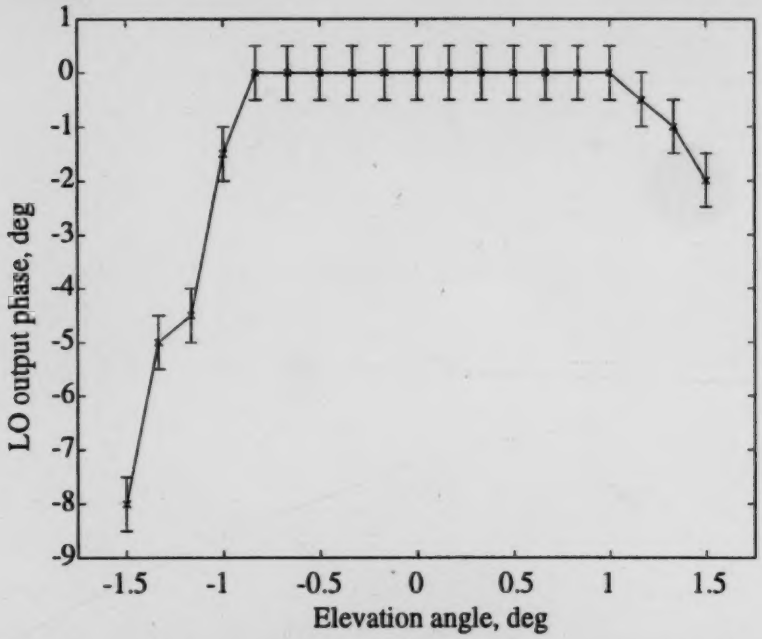

Figure 5.40: Phase variations at the LO output as a function of the antenna pointing. The angles were obtained from the power level measurements. The theoretical value for the HPBW was used. The phase is normalized.

The test showed that the output of the LO system is not affected by the pointing when the accuracy of pointing is within one third of the narrowest beamwidth. It was expected that the pointing must be within the HPBW of the narrowest beamwidth; however, the measurement showed that better pointing is required. Multipath might have affected the measurements slightly as the phase variations are less prominent when the elevation of the ground antenna is higher.

Locking response: The step response could not be measured adequately for the reasons already described. Therefore a similar test to the one discussed in Section 5.5.2 was performed. Figure 5.41 shows the result of the test.

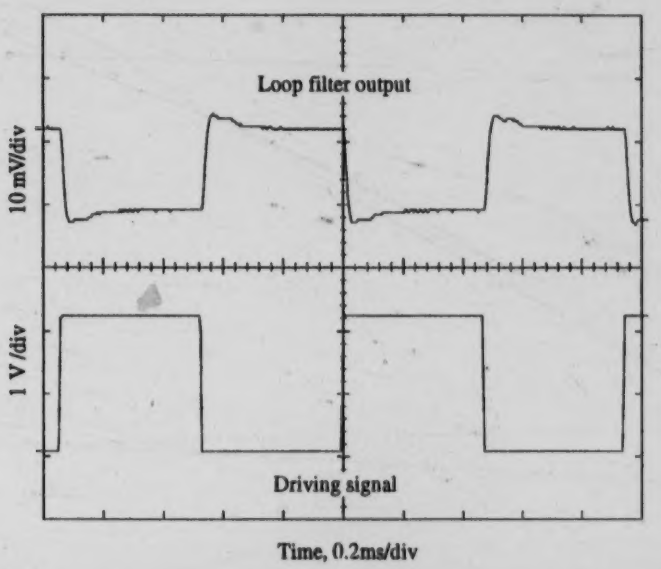

Figure 5.41: "Locking response" of the phase-halving PLL loop filter output to a square wave modulation of the 675 MHz reference signal (350 m test).

LO output spectrum: The spectrum of the LO output was recorded to compare with the spectrum of the 3.15 GHz reference signal. Figures 5.42 and 5.43 show both spectra. The spectra look almost identical suggesting that the LO system does deliver the reference signal to the remote unit.

Optimum design test: In this final test, the gain of the amplifier labelled "Amplifier A" in Figure B.2 was changed to determine if the response of the LO system worsens as the loop parameters deviate from the optimum. Figure 5.44 shows how the increase in the gain by 100 had changed the "locking response". It was also found that slight variations in the loop parameters did not affect the performance of the system.

5.5.4 800 metre test

The buried cable (see Figure 5.28) attenuates the 3.15 GHz signal by 110 dB which combined with 30 dB attenuation in the 50 m cable reduces signal to noise ratio considerably. The measured SNR at the input to the phase-halving PLL was -40 dB which is a little bit better than calculated (-45 dB see Section 5.4.3.1) but it still prevented the PLL from locking.

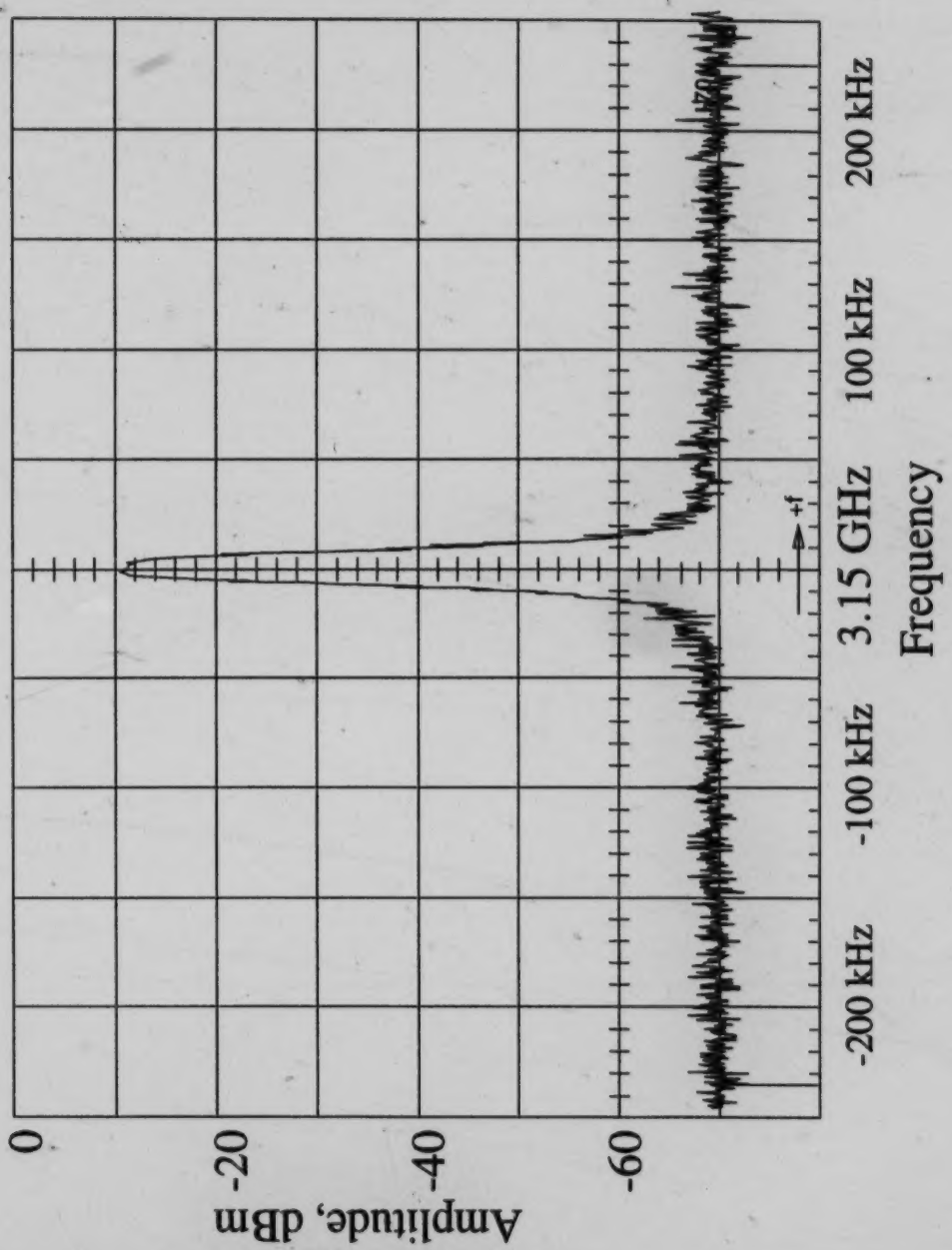

Figure 5.42: LO output signal spectrum (350 m test). The resolution bandwidth equals 10 kHz and the spectrum analyzer's internal oscillator is used.

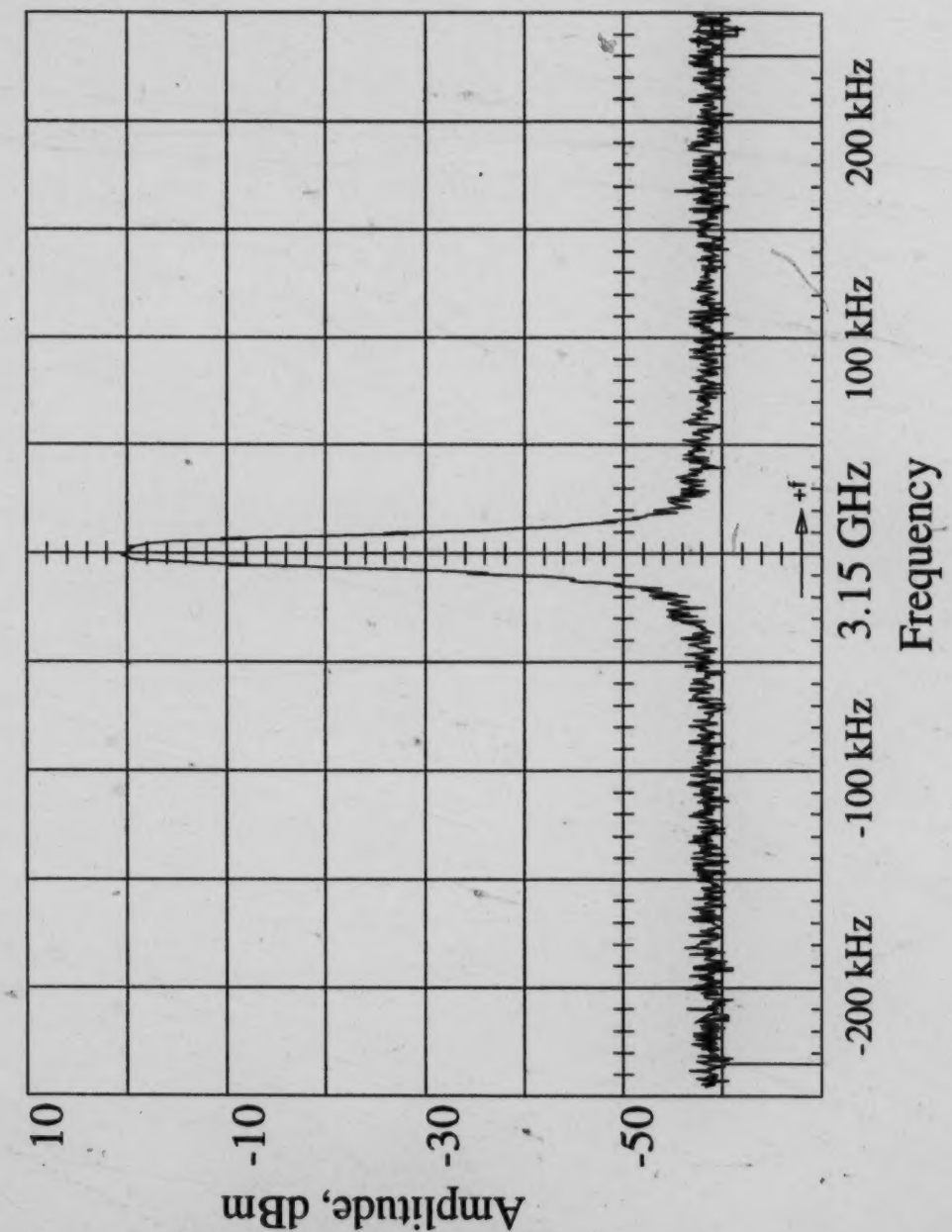

Figure 5.43: LO reference signal spectrum (350 m test). The resolution bandwidth equals 10 kHz and an external frequency reference is used.

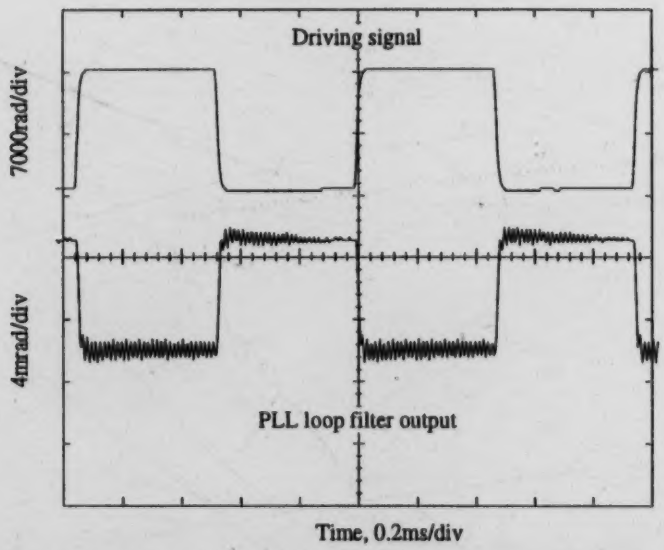

Figure 5.44: "Locking response" of the phase-halving PLL loop filter output to a square wave modulation of the 675 MHz reference signal as the gain of "Amplifier A" increased by 100 (350 m test).

5.6 Discussion

There were two main problems encountered while testing the LO prototype system. A proper test requires measuring the phase of the LO system output at the remote unit location. The test demands a phase-stable signal generator located by the remote unit so that its output can be compared with the output of the signal generator. However, such a generator was not available, making this test impossible. The other problem had to do with multipath. Even though the multipath should not be a problem in the LAR telescope, during the test the two antennas were located 300 m apart and 2 m above the ground creating the multipath problem. A person walking below the ground antenna feed caused noticeable phase variations in the LO system output.

A prolonged test of the LO system was not possible since some of the equipment and the cable used to return the LO output signal back to the ground unit were not located in a temperature-stable environment, causing phase drifts in the LO system output. It is, therefore, suggested that for proper testing, and for use in the LAR, a temperature-controlled environment would be beneficial.

Antenna pointing must also be addressed when testing the final LO system. It must be possible to control and record pointing of the antennas. It was almost impossible to measure how accurately the antennas must be pointed at each other to ensure proper performance of the LO system because there were no means of measuring antenna pointing. Although it is very likely that multipath was the reason why pointing of the antennas needed to be within one third of the main beam instead of the whole beamwidth, a more accurate test is still required to determine if it is really the case.

The tests showed that time delay did not affect the system performance. This suggests that initial testing of the LO system in a laboratory with zero time delay is adequate to predict the performance of the LO system with the time delay. The tests also showed that MATLAB/SIMULINK simulations were correct.

It is suggested that the USG and LSG based on PLLs be used in the final LO system. Simulations have shown that if the bandwidths of the PLLs are wider than $\frac{\pi}{2T_d}$[rad/s], where T_d is the time delay, the effects of the USG PLL and the LSG PLL on the behaviour of the LO system are negligible and the phase-halving system may have the bandwidth suggested during the prototype design. If, however, one of the bandwidths of one of the two PLLs is narrower than $\frac{\pi}{2T_d}$, the phase-halving system bandwidth must be reduced to maintain good behaviour of the entire system. The exact bandwidths of the PLLs cannot be recommended here because it is not known what kind of VCOs will be used in their design. When the final system is designed the VCO noise characteristics and the reference signal noise will govern the PLL bandwidths selection. The bandwidth will have to be adjusted so as to optimize the

rejection of the internal VCO noise and the external reference noise. It is, however, expected that the bandwidths can be quite wide, preferably exceeding 150 kHz to satisfy the condition mentioned above. If that is the case, problems can arise from high frequency poles that may worsen performance of the PLLs. A capacitor across the resistor R_1 (see Figure 5.12) may be necessary to introduce an extra zero in the transfer function and to improve behaviour of the PLLs [32]. It is also suggested to design the LSG PLL and the USG PLL so that they have slightly different lock-in time to avoid one of them locking onto the errors in the other one. Vaneldik and Landecker (1982) also suggest that the PLLs have to be nearly critically damped or overdamped to avoid noise multiplication by the major peaks in the system noise response [32].

Since the earth is in constant motion around its axis and around the Sun, the signals received by any telescope on the ground will appear frequency shifted due to the Doppler effect. It is suggested that the signals in the LO system should not be altered to facilitate the Doppler tracking since changing the phase of the signals will complicate the distance measurements performed by the FLM. The Doppler tracking can, however, be accomplished during data processing in the correlator.

One main unknown that was not taken into an account in the LO design presented in this chapter is the power spectral density distribution of the airborne platform velocities. It is essential to know the distribution for proper design of the LO system. Once the spectral density distribution is known, the critical parameters in the phase-halving PLL must be revisited to ensure that LO system responds properly to focal distance variations.

Chapter 6

Conclusion

This thesis described a Local Oscillator system and a Focal Length Measurement system suggested for the LAR telescope. The system consists of a ground unit and a ground antenna located in the centre of the LAR and a remote unit and a remote antenna located at the airborne platform. The separation between the antennas is 500 m.

The LO system delivers a phase- and frequency-stable signal to the airborne platform. A feedback control system is employed to readjust the phase of the delivered signal removing phase variations due to airborne platform motion. The dynamic response of the control system is controlled by a PLL. A prototype for the system has been designed, simulated, and tested. The tests revealed that the design and the simulations were correct and that the simulations can be used to design the final LO system. There were a few complications with testing that must be overcome when testing the final system. It was not possible to measure the phase of the LO output signal directly at the LO output because a signal generator was not available to serve as a reference signal. It was also impossible to measure antenna pointing very accurately to determine pointing requirements for the LO system. Nevertheless, the behaviour of the system matched expectations very well and it is believed that the system will be able to perform according to specifications.

Procedures for distance measurement and calibration based on the Chinese remainder theorem for use in the FLM system were recommended. The FLM system provides precise focal length measurement and has 3-D position determination capability. The Chinese remainder theorem provides a convenient way of resolving ambiguities. 3-D positioning becomes possible by measuring the pointing of the ground antenna tracking the airborne platform. Employing monopulse techniques and using the results of the focal length measurement using the PRN signal, the FLM is able to determine the 3-D positioning with an accuracy in the order of a few millimetres. The FLM system has not been tested.

Both systems, the FLM system and the LO system, are based on the same

concept of interferometry and are combined into one system.

A more detailed design of the FLM part of the FLLOSS is still required before the final FLLOSS is constructed. This design must include simulations of the FLM system so that the exact algorithm for ambiguity resolution using the CRT can be obtained.

Bibliography

[1] J.E. Allnutt. *Satellite-to-Ground Radio Propagation: Theory, Practice and System Impact at Frequency above 1 GHz.* Peter Peregrinus Ltd., London, 1989.

[2] G. Aloisio, A. Guerriero, C. Marzo, G. Milillo, and E. Morelli. An introduction on old and new SAR interferometric techniques. In *Symposium on Applications of Multifrequency/Multipolarization SAR in View Of X-EOS CGS*, pages 177–196, May 1990.

[3] M.A. Benkhelifa, M. Gindre, J-Y.L. Huerou, and W. Urbach. Echography using correlation techniques: Choice of coding signal. *IEEE Transactions on Ultrasonics, Ferroelectrics, and Frequency Control*, 41(5):579–587, September 1994.

[4] R.E. Best. *Phase-Locked Loops: Theory, Design, and Applications.* McGraw-Hill Book Company, New York, 1984.

[5] W.L. Brogan. *Modern Control Theory.* Prentice-Hall, Upper Saddle River, NJ, third edition, 1991.

[6] C. Carignan, P.E. Dewdney, E.R. Seaquist, A.R. Taylor, and C.D. Wilson. Canadian radio astronomy in the 21st century - the challenge. The Second Report of the NRC Planning Committee for a New National Facility for Radio Astronomy, Dominion Radio Astrophysical Observatory, National Research Council of Canada, December 1996.

[7] B.R. Carlson, P.E. Dewdney, T.A. Burgess, R.V. Casorso, W.T. Petrachenko, and W.H. Cannon. The S2 VLBI correlator: A correlator for Space VLBI and geodetic signal processing. *Proceedings of the Astronomical Society of the Pacific*, 111:1025–1047, August 1999.

[8] W.N. Christiansen and J.A. Högbom. *Radiotelescopes.* Cambridge University Press, Cambridge, 1969.

[9] J. Clarke. The Chinese remainder theorem and multi-PRF radars. Memorandum 3650, Royal Signals and Radar Establishment, London, February 1984.

[10] R.E. Collin. *Antenna and Radiowave Propagation.* McGraw-Hill Book Company, New York, 1985.

[11] D.C. Cox, H.W. Arnold, and R.P. Leck. Phase and amplitude dispersion for earth-satellite propagation in the 20-30 GHz frequency range. *IEEE Transactions on Antennas and Propagation*, AP-28:359–366, May 1980.

[12] W.D.T. Davies. Generation and properties of maximum-length sequences. *Control*, June-August 1966.

[13] D.A. De Wolf. Rayleigh-mie approximation for line-of-sight propagation through rain at 5-90 GHz. *IEEE Transactions on Antennas and Propagation*, 44(3):273–279, March 1996.

[14] P.E. Dewdney and B.G. Veidt. Specifications and guidelines for research in critical development areas. Technical report, Dominion Radio Astrophysical Observatory, National Research Council of Canada, February 1997.

[15] R.C. Dorf. *Modern Control Systems.* Addison-Wesley Publishing Company, New York, sixth edition, 1992.

[16] E.B. Fomalont. Astronomy and geodesy. In G.B. Taylor, C.L. Carilli, and R.A. Perley, editors, *Synthesis Imaging in Radio Astronomy II*, volume 180, pages 463–479. Astronomical Society of the Pacific Conference Series, 1999.

[17] G.F. Franklin, J.D. Powell, and A. Emami-Naeini. *Feedback Control of Dynamic Systems.* Addison-Wesly Publishing Company, New York, third edition, 1994.

[18] D.E. Fry. The use of cross-correlation and power spectral techniques for the identification of the Hunter Mk.12 dynamic response. Aeronautical Research Council, Her Majesty's Stationery Office, 1970.

[19] D.J. Gale and R.M. Braun. Path length analyzer for digital microwave radio. In *COMSIG 88: Proceedings of the Southern African Conference on Communications and Signal Processing*, pages 140–143, CSIR Conference Centre, Pretoria, South Africa, 1988.

[20] F.M. Gardner. *Phaselock Techniques.* John Wiley & Sons, New York, second edition, 1979.

[21] M.A. Goldman, R.E. Creager, D.H. Parker, and J.M. Payne. Rangefinder metrology for the Green Bank Telescope. GBT memo 162, March 10, 1997.

[22] M.P.M. Hall. *Effects of the Troposphere on Radio Communication.* Peter Peregrinus Ltd., London, 1979.

[23] M.P.M. Hall and L.W. Barclay. *Radiowave Propagation*, volume 30 of *IEEE Electromagnetic Waves Series.* Peter Peregrinus Ltd., London, 1989.

[24] A.F. Harvey. *Microwave Engineering.* Academic Press, London, 1963.

[25] B. Hofmann-Wellenhof, H. Lichtenegger, and J. Collins. *Global Positioning System: Theory and Practice.* Springer-Verlag, New York, second edition, 1993.

[26] J. Holland. Multiple feed antenna covers L, S and C-band segments. *Microwave Journal*, pages 82–85, October 1981.

[27] B.M. Horton. Noise-modulated distance measuring systems. *Proceedings of the IRE*, 47(5):821–828, 1959.

[28] ITU. *Radio Regulations.* International Telecommunication Union, Geneva, 1982.

[29] F.A. Jenkins and H.E. White. *Fundamentals of Optics.* McGraw-Hill, Inc., New York, fourth edition, 1976.

[30] J.D. Kraus. Antenna design note. *IEEE Transactions on Antennas and Propagation*, AP-25(6), November 1977.

[31] J.D. Kraus. *Antennas.* McGraw-Hill Boook Company, Singapore, second edition, 1988.

[32] T.L. Landecker and J.F. Vaneldik. A phase-stabilized local-oscillator system for a synthesis radio telescope. *IEEE Transactions on Instrumentation and Measurement*, IM-31:185–192, September 1982.

[33] F.H. Lange. *Correlation Techniques.* Iliffe Books Ltd., London, 1967.

[34] F.H. Lange. *Correlation Techniques: Foundations and Applications of Correlation Analysis in Modern Communications.* Measurement and Control. Trans. P.B.Johns. New Jersey: D. Van Nostard Company, Inc., Princeton, 1967.

[35] T.H. Legg. A proposed new design for a large radio telescope. *Astronomy and Astrophysics Supplement*, 130:369–379, June 1998.

[36] A. Leick. *GPS Satellite Surveying.* John Wiley & Sons, New York, second edition, 1995.

[37] N. Levanon. *Radar Principles.* John Wiley & Sons, New York, 1988.

[38] H.J. Liebe. Modeling attenuation and phase of radio waves in air at frequencies below 1000 GHz. *Radio Science*, 16:1183–1199, November-December 1981.

[39] M.A. Nahon. Dynamics and control of a novel radio telescope antenna. In *Proceedings of the AIAA Modeling and Simulation Technologies Conference*, pages 214–222, Portland, August 1999.

[40] I. Niven and H.S. Zuckerman. *An Introduction to the Theory of Numbers.* John Wiley & Sons, 1966.

[41] NOAA. *Solar-Geophysical Data: Prompt Reports, Part I.* Number 651. National Oceanic and Atmospheric Administration, November 1998.

[42] K. Ogata. *Modern Control Engineering.* Prentice-Hall, Toronto, 1970.

[43] J.M. Payne, D. Parker, and R.F. Bradley. Rangefinder with fast multiple range capability. *Review of Scientific Instruments*, 63:3311–3316, 1992.

[44] J. F. Ready. *Industrial Application of Lasers.* Academic press, San Diego, second edition, 1997.

[45] M.S. Roden. *Analog and Digital Communication Systems.* Prentice Hall, New Jersey, third edition, 1991.

[46] A.E.E. Rogers. Very long baseline interferometry with large effective bandwidth for phase-delay measurements. *Radio Science*, 5(10):1239–1248, October 1970.

[47] J.J. Saastamoinen. *Surveyor's Guide to Electromagnetic Distance Measurement.* University of Toronto Press, Toronto, 1967.

[48] D.V. Sarwate and M.B. Pursley. Crosscorrelation properties of pseudorandom and related sequences. *Proceedings of IEEE*, 68(5):593–619, May 1980.

[49] M.I. Skolnik. *Radar Handbook.* McGraw-Hill Book Company, New York, 1970.

[50] J.J. Spilker Jr. *Global Positioning System: Signal Structure and Performance Characteristics.* Stanford Telecommunications Inc., Sunnyvale, 1978.

[51] W.L. Stutzman, T. Pratt, D.M. Imrich, W.A. Scales, and C.W. Bostian. Dispersion in the 10-30 GHz frequency range: Atmospheric effects and their impact on digital communications. *IEEE Transactions on Communication*, COM-34(3):307–310, March 1986.

[52] A.R. Taylor and R. Braun. Science with the Square Kilometer Array: A next generation world radio observatory. Technical report, Department of Physics and Astronomy, University of Calgary, March 1999.

[53] A.R. Taylor, P.E. Dewdney, S.M. Dougherty, and N. Bartel. Science with the Canadian Large Adaptive Reflector. Technical report, Dominion Radio Astrophysical Observatory, National Research Council of Canada, April 1999.

[54] A.R. Thompson, J.M. Moran, and G.W. Swenson Jr. *Interferometry and Synthesis in Radio Astronomy.* John Wiley & Sons, New York, 1986.

[55] B.G. Veidt, T.L. Landecker, J.F. Vaneldik, P.E. Dewdney, and D. Routledge. A 408-MHz aperture synthesis radio telescope. *Radio Science*, 20(5):1118–1128, September-October 1985.

[56] R.S. Warwick, R.F. Davis, and R.E. Spencer. Phase stability, angular structure and position measurement with a radio-link interferometer. *Monthly Notice of the Radio Astronomical Society*, 177:335–347, 1976.

[57] L.R. Weill. Conquering multipath: The GPS accuracy battle. *GPS World*, 8(4):59–66, April 1997.

[58] Z. Yang, Z. Ting, R. Weiming, and L. Dacheng. Heterodyne interferometer with a dual-mode HeNe laser for absolute distance interferometry. *SPIE*, 2544:354–57, 1995.

[59] A.C. Young, M.G. McCulloch, S.T. Ables, M.J. Anderson, and T.M. Percival. The local oscillator system. *Journal of Electrical and Electronics Engineering*, 12(2):161–172, June 1992.

Appendix A

Remote unit and ground unit circuit diagrams

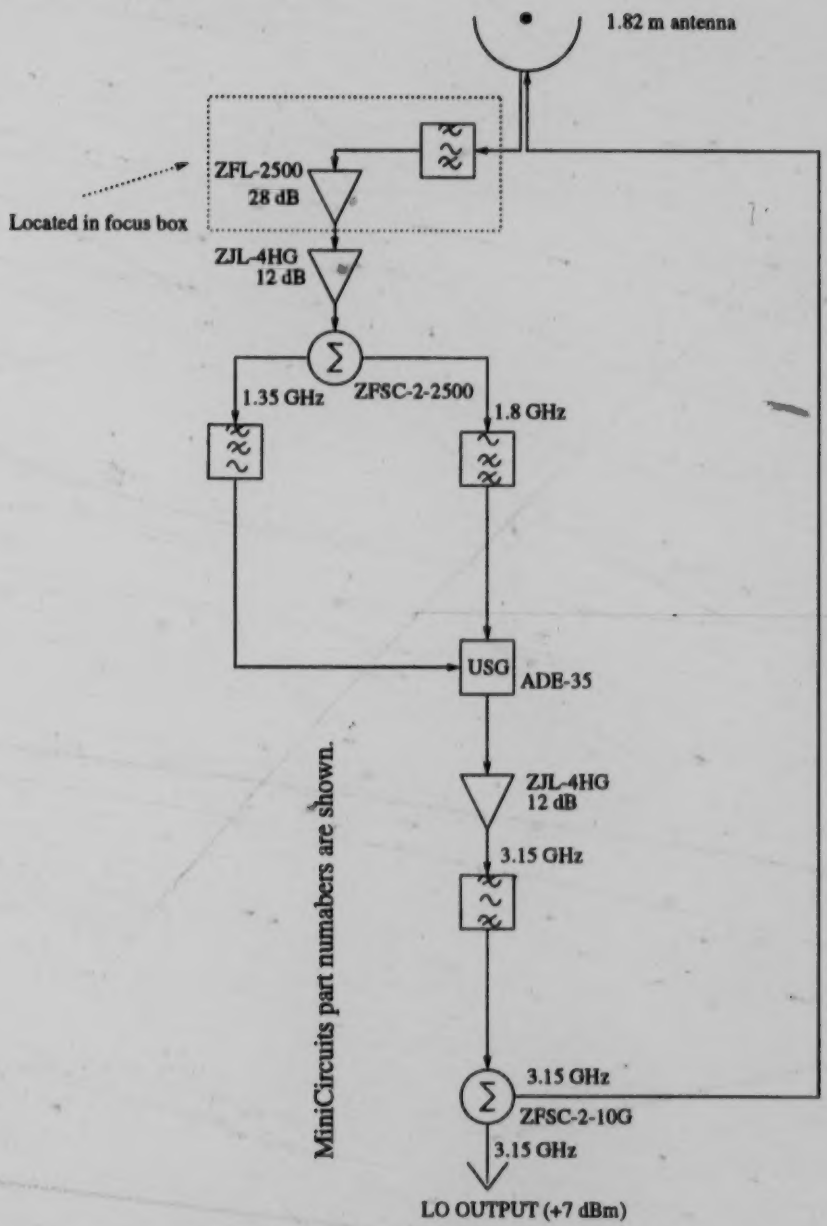

Figure A.1: Remote unit circuit diagram.

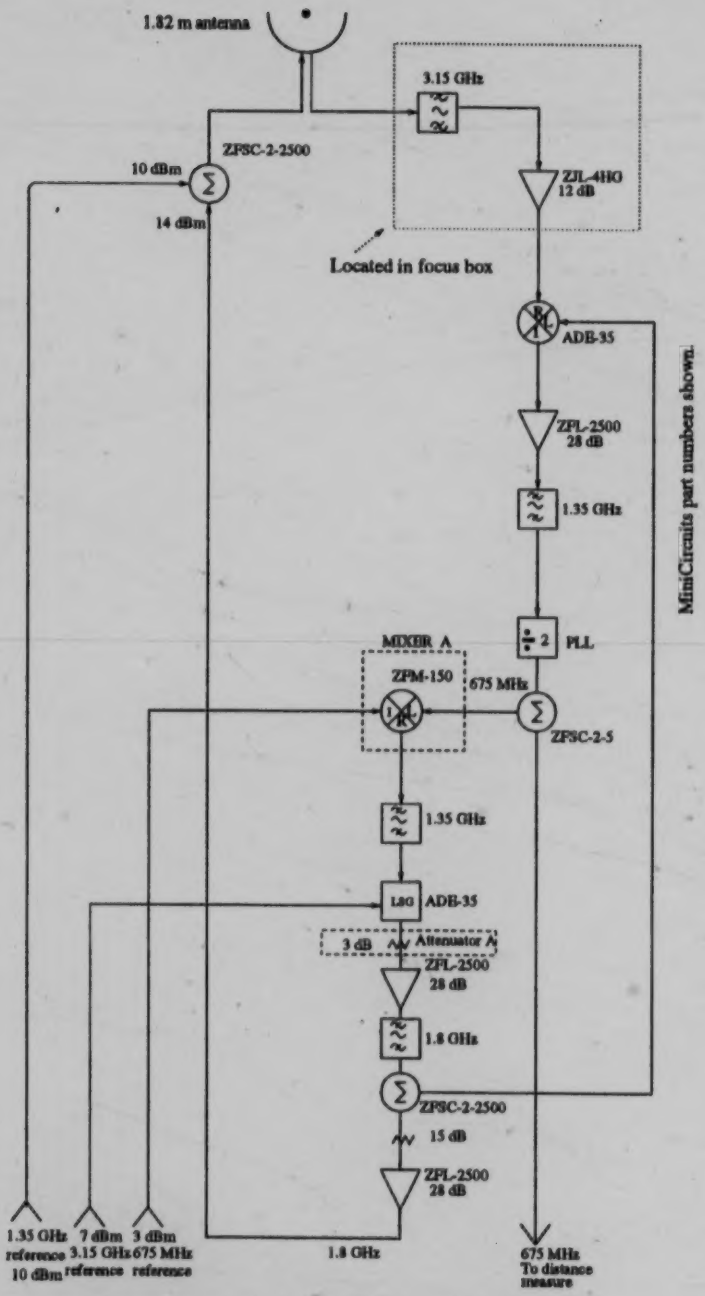

Figure A.2: Ground unit circuit diagram.

Appendix B

Phase-halving PLL: circuit diagram

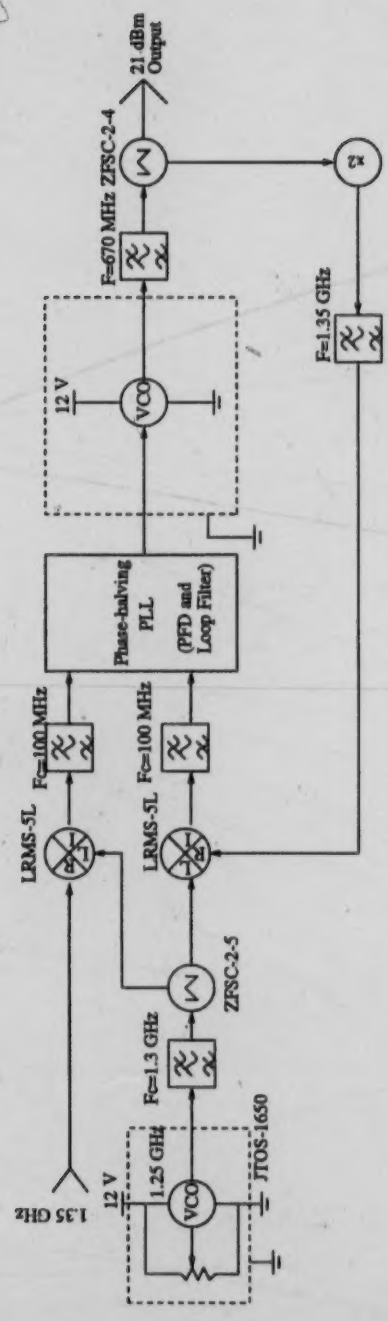

Figure B.1: Phase-halving system.

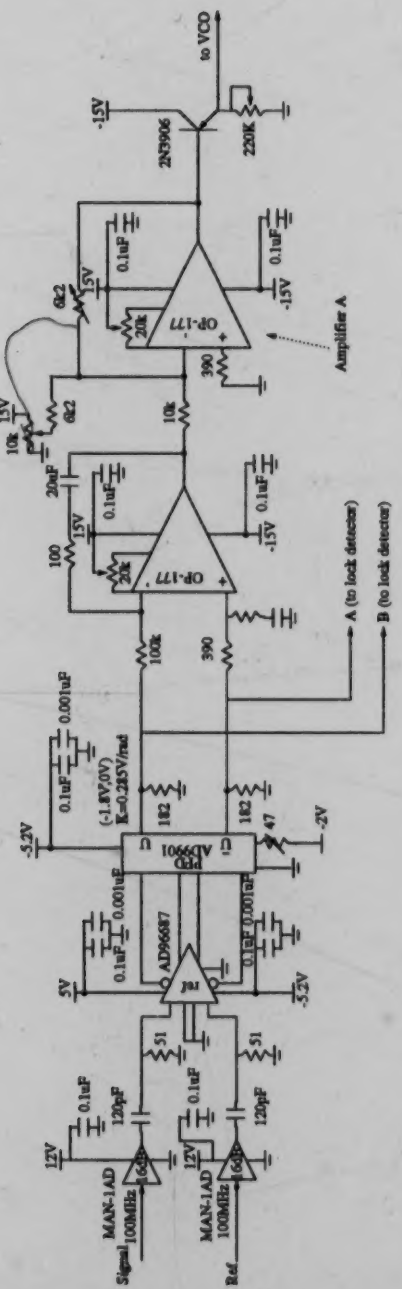

Figure B.2: Phase-halving PLL: phase detector and loop filter.

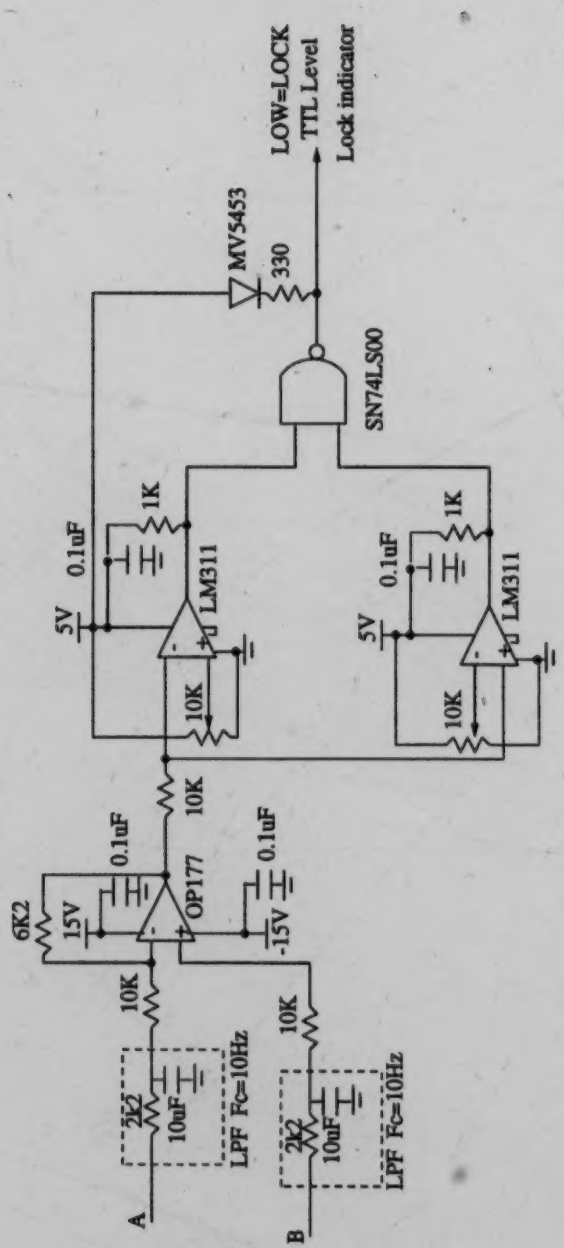

Figure B.3: Lock indicator.

Appendix C

Mixer assembly

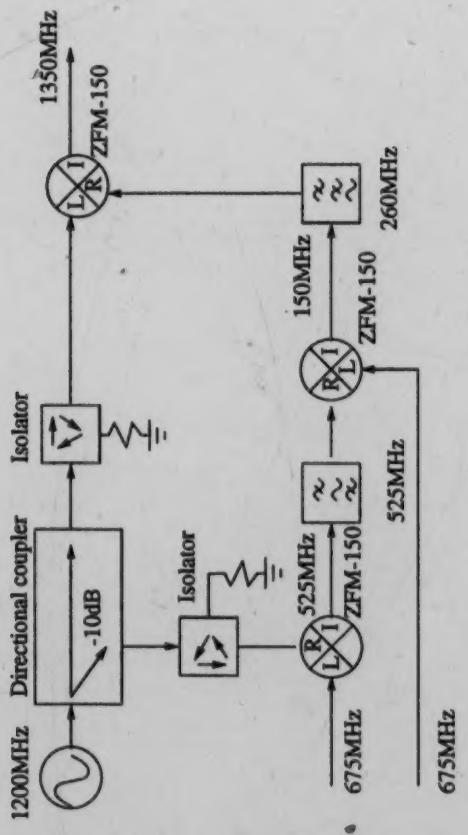

Figure C.1: Mixer assembly.